DIELECTRIC BREAKDOWN OF POLYCRYSTALLINE ALUMINA: A WEAKEST-LINK FAILURE ANALYSIS

by

Benjamin Block

A thesis submitted to the faculty of
The University of Utah
in partial fulfillment of the requirements for the degree of

Master of Science

Department of Materials Science and Engineering

The University of Utah

August 2013

Copyright © Benjamin Block 2013

All Rights Reserved

The University of Utah Graduate School

STATEMENT OF THESIS APPROVAL

The thesis of Benjamin Block
has been approved by the following supervisory committee members:

Dinesh K. Shetty	, Chair	6/6/13 Date Approved
Anil V. Virkar	, Member	6/17/13 Date Approved
Rebecca Brannon	, Member	6/7/13 Date Approved

and by Feng Liu , Chair of

the Department of Materials Science and Engineering

and by Donna M White, Interim Dean of The Graduate School.

ABSTRACT

The effects of varying electrode geometry (ball and ring) and size (radius), dielectric media (castor oil and Diala® oil), specimen thickness, and concentration of defects on the dielectric breakdown strength of commercial-grade alumina and high-purity fine-grained (HPFG) alumina were investigated. The breakdown strength was expressed in terms of the maximum electric field in the ceramic at the breakdown voltage calculated by finite element analysis (FEA). The breakdown strength decreased systematically with increasing electrode radius and specimen thickness. The breakdown strength increased with decreasing concentration of defects. The breakdown strength was higher in the Diala® oil (dielectric constant, $\varepsilon_r = 2.3 \pm 0.12$) as compared to the castor oil ($\varepsilon_r = 4.59 \pm 0.06$). The breakdown strength was higher for the HPFG alumina as compared to the commercial-grade alumina. These effects of the electrode geometry, specimen thickness, concentration of defects, and of the dielectric media were analyzed with a weakest-link failure model employing the Laplace and Weibull distributions for a population of defects in the material. The measured size or scaling effects of the electrodes, specimen thickness, concentration of defects, and of the liquid media on breakdown strength were in better agreement with the Laplace distribution for the population. The measured concentration of surface defects was in good agreement with the concentration of surface defects estimated from the surface area scaling of the breakdown field with the Laplace distribution.

TABLE OF CONTENTS

ACKNOWLEDGEMENTS

I would like to express my appreciation to my committee chair, Doctor Dinesh K. Shetty. His insights, teachings, guidance, and continual help are what made this thesis possible. I would like to thank my committee members, Doctor Anil V. Virkar and Doctor Rebecca Brannon, for their advice and insights throughout my M.S. research.

I would also like to thank Varian Medical Systems for funding this research. Discussions with and assistance from James Boye, Christopher Lewis, Grant Gerringer, and Michael Oates were invaluable in obtaining the results reported in this thesis.

Finally, I would like to thank my wife, Cierra, my sister, Lisa, and my parents, Jon and Margarete, for their support and inspiration during my studies.

CHAPTER 1

INTRODUCTION

1.1 Motivation for Research

Polycrystalline alumina is widely used as an insulator in high-voltage devices[1]. High voltage devices employ polycrystalline alumina for insulators due to its high dielectric breakdown field, dimensional stability, and low cost. Breakdown fields reported in the literature for alumina at room temperature range from less than 10 kV/mm to greater than 100 kV/mm for bulk specimens[2-5], and as high as 1100 kV/mm for thin films[4,6,7]. Part of the variation in breakdown field can be attributed to variation in intrinsic factors such as microstructure of the alumina, specifically, porosity, grain size, and composition. The variation in breakdown strength is also affected by extrinsic factors such as electrode size and shape, dielectric medium, specimen thickness, and surface finish. Extrinsic factors have a much greater effect on breakdown strength than intrinsic factors[8]. Extrinsic factors are a relatively unexplored area with little data reported in the open literature.

Currently, there is no method available to predict how well a given insulator will perform. The aim of this research was to develop a methodology to predict the dielectric breakdown strength of alumina for a given set of intrinsic and extrinsic factors. The design and optimization of alumina insulators could then be done using FEA instead of costly prototypes. To develop such a model, the root causes of dielectric breakdown must be

understood. A commercial-grade of alumina♦ was used in the majority of our research with HPFG alumina sintered from a commercial powder♠ used to assess the influence of alumina content and grain size on dielectric breakdown strength.

1.2 Dielectric Breakdown Mechanisms

Dielectric breakdown mechanisms can be broadly classified into two categories: (1) electrical breakdown mechanisms, and (2) thermal-breakdown mechanisms. Both of these mechanisms can be triggered at defects that concentrate the electric field locally.

1.2.1 Electrical Breakdown Mechanisms

In 1937, Fröhlich[9] proposed a formula for a critical electric field, F, in thin single crystal dielectrics. The critical field occurs when the rate of collision recombination is less than the rate of collision ionization:

$$F = 1.6(\log\gamma)^{\frac{1}{2}} * 10^5 \frac{\lambda}{Ma^4 (hv)^{\frac{1}{2}}} \left(1 + \frac{2}{e^{\left(\frac{hv}{kT}\right)} - 1}\right)^{\frac{1}{2}} \tag{1.1}$$

$$\gamma = \frac{(2E)^{\frac{1}{2}}}{2^{\frac{2}{3}} m^{\frac{1}{2}} va} \tag{1.2}$$

♦ Grade AD-94, CoorsTek Inc., 16000 Table Mountain Pkwy, Golden CO 80403.
♠ Taimei Chemicals Co., LTD., 3911 Minamiminowa-mura, Kaiina-gun, Nagno-ken, Japan.

$$\frac{1}{M} = \frac{1}{M^+} + \frac{1}{M^-} \tag{1.3}$$

where E is the kinetic energy of an electron, λ is the wavelength of the ultra-violet absorption, M^+ is the mass of the positive ion, M^- is the mass of the negative ion, a is the distance between two neighboring ions of opposite sign, h is Plank's constant, v is the Reststrahlen frequency, k is Boltzmann's constant, and T is the temperature. This mathematical equation agreed with experimental results only by an order of magnitude for single crystal alkali halide specimens. At 300°K, the theoretical breakdown strength and experimental breakdown strengths of NaCl are 107 and 150 kV/mm, respectively. At 300°K, the theoretical breakdown strength and experimental breakdown strengths of KCl are 66 and 80 kV/mm, respectively. The experimental results were reported in terms of normalized electrical field. Therefore, there is a degree of error present in the results.

In 1949, Seitz[10] proposed the avalanche theory, which stated that breakdown in solids was the result of electron avalanches similar to how breakdown occurs in gases. However, it was not clear how electrons would gain sufficient energy from the electric field for impact ionization with a comparatively small mean free path in solids. In 1969, O'Dwyer[11] resolved this issue by proposing that impact ionization and electron injection worked in concert, which resulted in a larger distortion of the field. The field near the cathode may be orders of magnitude higher than the average field, which would be sufficient to destroy the specimen integrity. In 1982, O'Dwyer[12] went on to state that electrical breakdown is the result of the onset of collision ionization. This mechanism for breakdown occurs at low temperatures when the limiting factor is electrical conductivity.

1.2.2 Thermal Breakdown Mechanism

In 1927, Fock[13] and in 1931, Moon[14] stated that breakdown strength was temperature dependent. They detected a rapid rise in the internal temperature of a specimen near the breakdown voltage. In 1969, O'Dwyer[12] defined thermal breakdown as a process that can be explained using reasonable extrapolations of the electrical and thermal conductivities from values obtained substantially below breakdown. In 2004, Kao[16] concluded that the electrical breakdown of any material is ultimately due to thermal instability, which causes the destruction of the material.

Thermal breakdown is caused by electrical field applied for a duration sufficient to cause local heating. The local heating leads to a temperature increase that increases the electrical conductivity, but decreases the thermal conductivity of the material. For the temperature to rise, a volume element must generate heat in excess of what is dissipated by conduction and convection. The general equation governing the balance of the heat generation rate and the heat dissipation rate is given by the following[12, 15, 16]:

$$\rho C_p \frac{\partial T}{\partial t} - \nabla(k \nabla T) = Q \tag{1.4}$$

In Equation (1.4), ρ is density, C_p is specific heat capacity at constant pressure, T is temperature, t is time, k is the thermal conductivity, and Q is the heat source. Both dielectric (electronic) heating[17] and joule (ohmic) heating[18] are potential heat sources for thermal breakdown.

Dielectric heating is due to a changing electric field resulting from an alternating current. Heat is generated as molecules continually rearrange to align with the electric field. The dielectric heating rate (J/m^3s) is defined by the following equation[19]:

$$Q_D = \omega E^2 \varepsilon_o \varepsilon_r \tan\delta \tag{1.5}$$

In Equation (1.5), ω is the angular frequency, E is the electric field strength, ε_o is the permittivity of free space, ε_r is the relative permittivity of the medium, and $\tan\delta$ is the dielectric loss factor.

Joule heating stems from an induced electric current in the medium. The joule heating rate is defined by the following equation[16]:

$$Q_{JH} = E^2 \sigma \tag{1.6}$$

In Equation (1.6), E is the electric field and σ is the electrical conductivity.

Equation (1.4) cannot be solved analytically for dielectric and/or joule heating as several of the material properties vary with temperature and applied field. C_p, k, and $\tan\delta$ are functions of temperature and σ is a function of both temperature and applied field. It is, however, possible to obtain numerical solutions by finite element analysis (FEA) as a function of applied voltage.

1.2.3 Weakest-Link Failure Theory

Weakest-link theory states that the breakdown strength of a dielectric is the breakdown strength of the weakest defect in a sample of n defects[20]. The dielectric breakdown of ceramics possesses weakest-link characteristics similar to mechanical fracture[21, 22, 23]. In both cases, breakdown/fracture initiates at defects[24]. This is analogous to how a chain will break when the tensile stress exceeds the tensile strength of the weakest link in the chain. Weakest link is not a mechanism, it is a methodology to explain the effects of extrinsic variables. Both electrical breakdown and thermal breakdown mechanisms are compatible with weakest-link failure theory.

The concept of weakest-link failure was first used by Pierce[25] to explain the variation in the strength of yarn with specimen length. Pierce observed that if a specimen of length l broke under normally distributed loads, then a specimen of length nl would break under loads whose distributions are negatively skewed the lager the value of n. Pierce explicitly mentioned the work of Tippett[26] who had conducted the first basic statistical research on the distribution of extreme values.

In 1939, Weibull[22] proposed his statistical theory of the strengths of materials, based on a two-parameter population distribution now known as the Weibull distribution. It is important to note that Weibull did not recognize that the basis of his theory was the theory of extreme values.

In 1948, Epstein[20, 23] observed that mechanical and dielectric breakdown strengths scaled with the stressed number of defects, n. He assumed defects of varying size randomly distributed with a certain density per unit volume. Therefore, the number of stressed defects scaled with the stressed area or stressed volume. Depending on the size and orientation, a

defect can weaken a material. The defect sizes and orientations responsible for the greatest weakening of the material are pertinent to the breakdown strength. The worst flaw among n flaws determines the strength of the specimen. Epstein, therefore, applied the theory of extreme values to the weakest-link failure problem. He also observed that for many class of phenomena, the typical distributions are not Gaussian distributions. The treatment of weakest-link failure used in this study is described in Chapter 4.

1.2.4 Site Percolation Theory

Site percolation models employ a $\mathbb{Z}^d$ lattice network with each dimension having an independent number of vertices. Each vertex site can either be occupied with a probability of p or empty with a probability of 1-p. Site percolation determines the probability that for a given p, a path exists spanning the top to bottom plane of the lattice. Pathways are defined typically in two ways. First, a bond is assumed to exist between each pair of nearest neighbor sites on the lattice. Secondly, each site exerts a predefined range of influence and a bond exists between the site and to each site within this range. There exists a critical value of p, p_c, below which the probability of a pathway existing is always 0 and above which the probability is always positive. Site percolation is not a mechanism, it is a methodology to explain the effects of intrinsic and extrinsic variables. Both electrical breakdown and thermal breakdown mechanisms are compatible with site percolation theory.

In 1959, Gerson and Marshall[27] defined a ceramic as having voids which are uniform in size, randomly distributed through the specimen, with a dielectric breakdown strength of zero. The solid ceramic has a characteristic well-defined breakdown strength.

Therefore, breakdown will occur along a path containing a maximum number of voids and a minimum of solid ceramic. The following formula gives the breakdown strength, E, predicted by their model:

$$E = E_0\left[n - \frac{x_m}{n}\right] \tag{1.7}$$

In Equation (1.7), E_0 the electric breakdown field for the solid ceramic, n is the number of sites along a linear path from the upper to lower specimen surfaces, x_m the highest number of voids occurring at least once per specimen. x_m is determined by solving the following formula:

$$NW_n(x_m) = 1 \tag{1.8}$$

In Equation (1.8), N is the number of columns in the stressed area and $W_n(x)$ is the probability of finding a column containing x voids given n cubes per column. N and $W_n(x)$ are defined in the following equations:

$$W_n(x) = \frac{n!}{x!(n-x)!}\left[1 - \frac{\rho}{\rho_o}\right]^x\left[\frac{\rho}{\rho_o}\right]^{n-x} \tag{1.9}$$

$$N = \left[\frac{D}{d}\right]^2 \tag{1.10}$$

In Equations (1.9) and (1.10), n is the number of cubes in each column, x is the number of voids in a column, ρ is the bulk density of porous ceramic, ρ_o is the theoretical density of void-free ceramic, D is the diameter of the uniformly-stressed area, and d is the diameter of the average void.

Gerson and Marshall created artificial pores of a known size and quantity to validate their model. They correctly predicted the scaling of breakdown strength with porosity. However, the Gerson and Marshall model only considered linear paths perpendicular to the surface of the specimen. Experimental finding showed that the breakdown path is nonlinear. Furthermore, their analysis incorrectly predicts that the breakdown field increases with increasing specimen thickness. Their experimental results showed that the breakdown field increased with decreasing thickness. This severely limits the usefulness of their percolation model.

In 1982, Duxbury et al.[28] proposed two percolations models for electrical breakdown: a fuse-wire network and a dielectric network. The dielectric network consists of a random mixture of conductors and insulators. The fraction of conductors (bonds present), is p. The vacant sites, $1 - p$, can withstand an electric field strength of 1 V. If the field strength exceeds 1 V, the site becomes conductive. As the applied voltage increases, vacant sites begin to breakdown and become conductive. Once enough vacant bonds breakdown, a conductive path emerges signifying dielectric breakdown. The fuse-wire model assumes each bond is a 1 Ω fuse which can withstand a current of 1 A, beyond which the bond transitions from a conductor to an insulator. Vacant sites are assumed to be insulators which can never breakdown and become conductors. As the applied voltage

increases, fuses are tripped and a conductive path through the specimen ceases to exist, resulting in breakdown. They observed the following behavior of breakdown strength:

$$\frac{V_b}{L} = \frac{a(p)}{1 - \frac{c(p)\log_e L}{\log_e p}} \tag{1.11}$$

In Equation (1.11), V_b is the breakdown voltage, L is the side length of the square matrix, and p is the bond fraction with a and c being constants determined by the model. Their model shows that any finite fraction of random defects reduces the electrical breakdown strength of solids in a macroscopic system.

1.3 Prior Experimental Research

The breakdown strength of alumina is influenced by the following factors: specimen microstructure (porosity, grain size, and impurities)[2,3,26-30], specimen thickness[3,6,31], surface finish[5,32-34], temperature[4,35], and electrode size and shape[36-40].

1.3.1 Effects of Microstructure (Porosity, Grain Size, and Impurity)

In 1970, Morse and Hill[2] measured dielectric breakdown strengths of sintered, hot-pressed, and single crystal alumina specimens. The dielectric strength increased with increasing density of the alumina. The authors stated that breakdown was initiated by discharges in gas filled pores. AC breakdown voltages were approximately 75% of DC breakdown voltages. All tests were conducted in either silicone or transformer oil. Also in 1970, Gitzen[3] suggested that AC breakdown voltages could be converted to DC values by

increasing the AC values by one third. The scaling of breakdown voltage with the frequency of the applied current is noteworthy. Electron injection and propagation only occurs when an alternating current is in the positive phase of its cycle. Therefore, the electron concentration in the specimen is dependent not only on the electric field concentration, but also the current frequency. The dielectric heating rate is also dependent on the current frequency. Since both breakdown mechanisms are influenced by the current frequency, it is possible that studying the breakdown field with respect to the frequency could shed insights into the breakdown mechanisms.

In 1997, Beaudet et al.[29] studied the effects of bulk doping on dielectric breakdown strength of alumina. Alpha alumina powder was bulk doped with chromium oxide at 1 wt%, manganese oxide at 1 wt%, and a combination of chromium oxide and manganese oxide at 1 wt% each. The pure alumina (no doping) performed the worst at 75 kV/cm, chromium oxide samples were slightly better at 90 kV/cm, manganese oxide samples were stronger at 110 kV/cm, and the samples with both dopants performed the best at 120 kV/cm.

In 1998 and 2001, Liebault et al.[30, 31] observed that breakdown strength increased with decreasing grain size for several grades of high-purity alumina. They also noted an increase in dielectric breakdown strength with increasing specimen density. The relative influence of the grain size on breakdown strength varied with alumina grades and the presence of impurities. Alumina doped with calcium oxide had a higher breakdown strength than an alumina doped with magnesium oxide, which is a common sintering aid for alumina. They also performed absorbed current measurements on the same materials. Materials capable of diffusing injected charge had a higher breakdown strength than those

that trapped the charge locally. This finding indicates an electrical breakdown mechanism as well as a potential approach to improving specimen breakdown field strength.

In 2006, Sangawar and Kumar[32] studied the effect of density on dielectric strength of alumina. They varied the density by varying the sintering temperature (1600, 1620, and 1650°C) and sintering time (10 and 90 minutes). The dielectric strength increased with increasing density ranging from 3.37 to 28.30 kV/mm for densities ranging from 2.77 to 3.8 g/cm^3. They also noted that alumina simultaneously doped with magnesium oxide and silicon dioxide had higher dielectric constant and dielectric strength than an alumina doped with only magnesium oxide.

In 2007 and 2010, Touzin et al.[1,33] studied the influence of grain size and grain boundaries on dielectric breakdown strength. At room temperature, they observed an increase in breakdown strength in materials with microstructures containing very fine grains or highly-crystallized secondary phase material. These materials were able to stabilize a high amount of charges, creating a very negative surface potential which prevented further charge injection. At higher temperatures, traps lose their activity and breakdown strength depends on the ability to diffuse the charge.

1.3.2 Thickness Effect

In 1950, Lomer[6] studied the dielectric strength of alumina thin films with varying thickness. Breakdown strength increased with decreasing specimen thickness. Breakdown strengths for specimen thickness of 1000 and 100 Angstroms were 600 and 1000 kV/mm, respectively. He suggested that a critical number of ionizing collisions is required to produce a breakdown event. As specimen thickness decreased, so did the required number

of collisions. Therefore, dielectric strength increased with decreasing specimen thickness. Additionally, the number of ionizing collisions increased with increasing the local electrical field.

In 1970, Gitzen[3] studied the dielectric strength of bulk alumina specimens with varying thickness. The measured breakdown strength increased with decreasing specimen thickness. The specimens tested varied in thickness from 1 mm to 6.35 mm. Breakdown strength increased from 9.1 kV/mm to 20.0 kV/mm as the thickness of the specimens decreased from 6.35 mm to 1 mm. In 1982, Owate[34] and Freer observed that the breakdown strength of planar alumina specimens increased with decreasing thickness. They concluded that the breakdown strength falls with increasing specimen thickness due to an increasing probability of the presence of a breakdown initiating flaw. In 2010, Talbi and Lalam[35] also observed similar scaling of breakdown strength with varying thickness. They stated that the formation and growth of defects due to electromechanical strain is best suited to describe the dielectric breakdown of alumina. In their view, dielectric breakdown occurs when the work done by the mechanical forces exceeds the crack propagation energy. Figure 1.1 shows a plot of breakdown strength versus specimen thickness for thin film and bulk alumina specimens.

1.3.3 Surface Finish Effect

In 1988, and 1992, Owate and Freer[5, 34, 36] showed that the dielectric breakdown strength of alumina was dependent on surface finish. The breakdown strength of ground

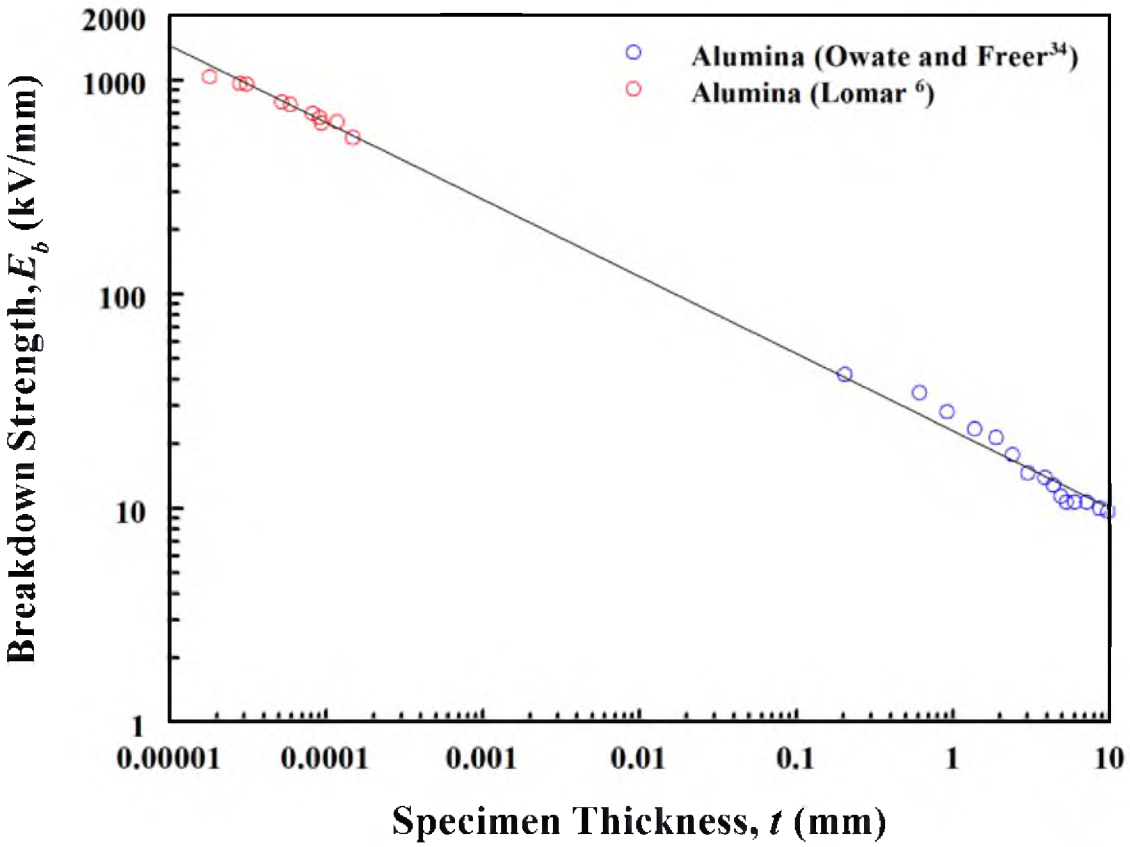

Figure 1.1 Breakdown strength of thin film and bulk alumina specimens versus specimen thickness.

and polished specimens was between 48 and 70% higher than the breakdown strength of as sintered specimens. This improvement in breakdown strength was attributed to the removal of surface flaws, decrease of surface texture, and improved contact between specimen and the electrodes. These factors contribute to a more uniform electric field. Their results are shown in Table 1.1. They proposed three stages to the electrical breakdown process of ceramic materials. (a) Electrons emitted by the electrodes bombard the surface of the material and produce more electrons through secondary emissions. They noted that, the ionization potential at defect sites is lower than that of defect free regions. (b) The breakdown channel propagates from the initiation site through the specimen thickness. (c) Molten material flows towards the electrode-material interface, creating the solidification crater. In 2002, Shiorir et al.[37] also observed that breakdown voltages for polished specimens were higher than the breakdown voltages of unpolished specimens. They stated that mechanical strain due to surface defects was responsible for dielectric breakdown.

Table 1.1 Effects of grinding and polishing on the dielectric breakdown strength of polycrystalline alumina. (adapted from Owate and Freer[5])

Specimen thickness (mm)	Breakdown Strengths (kV/mm)			
	Planar specimen		Plano-concave specimen	
	Unground	Ground and Polished	Unground	Ground and polished
0.5	24.48	36.95	-	-
1.0	18.29	31.14	-	-
2.0	14.24	21.10	22.28	25.79

1.3.4 Temperature Effect

In 1950, Miyazawa and Okada[38] measured the breakdown voltage of alumina thin films at various temperatures. The films had a thickness of 70 μm and were coated onto a 40 mm length tungsten wire. Temperature within the thin films was controlled by passing current through the tungsten wire. Electrodes were placed onto the ends of the alumina layer and measured the maximum AC breakdown voltage with respect to temperature. Below 20°C, they observed little to no scaling of the breakdown voltage with temperature. Above 1200°C, they observed that the breakdown voltage decreased with increasing temperature. They concluded that the below 20°C breakdown is due to electric breakdown while above 1200°C breakdown is due to joule heating. In 1981, Yoshimura and Bowen[4] also observed breakdown strength decreasing with increasing temperature. The measured breakdown strengths were 150 kV/mm, 26 kV/mm, and 2 kV/mm at 25°C, 900°C, and 1400°C, respectively.

1.3.5 Electrode Size and Shape Effect

In, 1995 Goshima et al.[39, 40] analyzed the breakdown of liquid nitrogen using weakest-link theory. They observed that dielectric strength decreased with increasing statistical stressed electrode area (SSEA) and statistical stressed liquid volume (SSLV). They used a two parameter Weibull distribution to analyze the scaling effects of the electrodes in terms of SSEA and SSLV. The Weibull shape parameters measured for the individual test configurations were close to the parameters obtained from the scaling with electrode area of liquid volume. In 1997, Hayakawa et al.[41] confirmed the findings of Goshima, adding that the volume effect due to thermal bubbles dominated the breakdown

strength and that the area effect was due to microscopic protrusions on the electrode surface.

In 2006, Tibbitts and Shetty[8] and in 2010, Kim and Shetty[42] studied the breakdown voltage and breakdown strength of alumina with varying electrode size. The breakdown testing was done using alumina disk specimens (radius = 38.1 mm, thickness = 4 mm) with a variable top ball electrode radius and a fixed bottom ball electrode radius. The breakdown voltage increased with increasing top electrode radius. The breakdown strength increased with decreasing top electrode radius. This scaling was attributed to a decrease in effective stressed area with decreasing electrode radius consistent with the weakest-link theory.

1.4 Outline of Current Research

The objectives of this study were as follows:

(a) Characterize the scaling of electric fields with electrode size and shape, specimen thickness, surface finish, and alumina grade.

(b) Analyze the scaling of the breakdown field using extreme-value theory.

(c) Identify and characterize the defects at which breakdown is initiated by (i) characterizing the surface and volume defect sizes and concentration on as-received and re-finished alumina specimens, and (ii) conducting breakdown testing on as-received and re-finished alumina specimens.

(d) Develop a methodology to predict breakdown fields of alumina insulators under specified conditions by using the theory of weakest-link failure to fit experimental breakdown field data using the Weibull distribution and the Laplace distribution.

CHAPTER 2

EXPERIMENTAL PROCEDURES AND FINITE ELEMENT ANALYSIS

2.1 Test Materials

2.1.1 Commercial-Grade Alumina

Sintered and ground disks of alumina, with a diameter of 76.2 mm and a thickness of 4 mm, were purchased from a material supplier♦. The composition of the alumina disks was reported as 93.3 w% Al_2O_3, 4.1 w% SiO_2, 0.8 w% BaO, 0.7 w% MgO, with the remainder consisting of ZrO_2, CaO, etc. Sintering was done at 1645°C over a 52-hour cycle. The specimens were then ground to their final thickness of 4 mm, and annealed at 1500°C for 30 minutes. The top and bottom surfaces were finished using diamond wheels and a proprietary protocol by the material supplier. The root-mean-square (RMS) roughness, R_{RMS}, of the final surface finish was 0.304 μm. Figure 2.1 shows the microstructure of the alumina. The average grain size was reported as 12 μm. Additional properties of this alumina reported by the material supplier are summarized in Table 2.1.

♦ Grade AD-94, CoorsTek Inc., 16000 Table Mountain Pkwy, Golden CO 80403.

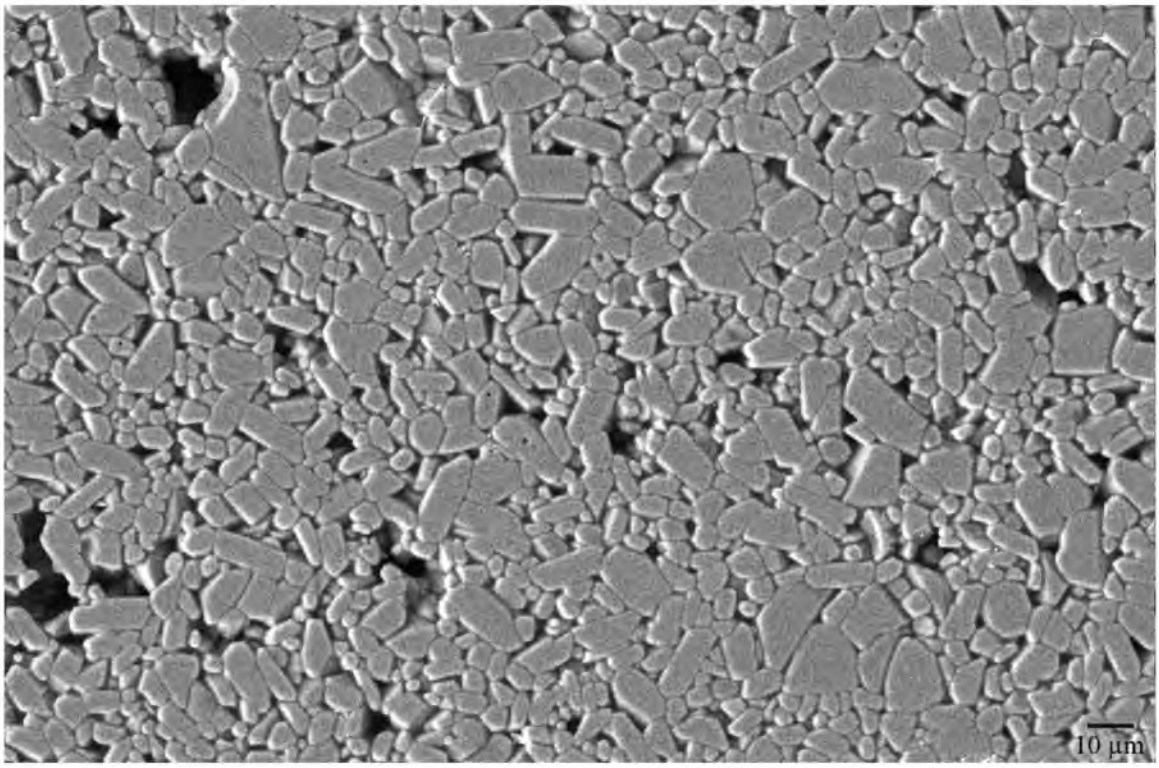

Figure 2.1 A SEM of the microstructure of commercial-grade alumina.

Table 2.1 Material properties of alumina used in this study[43,44].

Material Property	commercial-grade	HPFG
Grain Size (μm)	12	0.7
Density (gm/cc)	3.70	3.98
Resistivity @ 20°C (ohm-cm)	$1 * 10^{14}$	
Dielectric Strength (kV/mm)	8.3	
Dielectric Constant (ε_r)	9.1	
Specific Heat	880	
Thermal Conductivity @ 20°C (W/mK)	22.4	
Composition Al_2O_3 wt%	93.3	99.99

Additional 76.2 diameter disks were purchased with the following thicknesses: 2, 1, 0.5, and 0.25 mm. Also purchased were alumina disks with a diameter of 25.4 mm and a thickness of 1 mm. These disks were prepared in the same manner as the 4 mm disks.

2.1.2 High-Purity, Fine-Grained (HPFG) Alumina

Alumina disks with a diameter of 25.4 mm and a thickness of 4 mm were produced at the University of Utah by Tzu-Chien Wen[43]. The alumina powder was purchased from a material supplier♠. The composition of the powder was reported as 99.99 wt% Al_2O_3, ≤25 ppm Si, ≤15 ppm Fe, ≤10 ppm Na, ≤5 ppm K, ≤5 ppm Ca, ≤5 ppm Mg. A water-based alumina suspension was prepared with 78.0 w% solids content. The suspension was ball milled for 8 hours to breakdown agglomerates. The alumina suspension was then pressure-cast into a dense compact and dried in a humidity-controlled chamber for 2 days. The dried compact was prefired to remove organic additives then sintered at 1225°C in air over a 4-hour cycle. The specimens were sent to a ceramic finisher for surface finishing♥. The

♠ Taimei Chemicals Co., LTD., 3911 Minamiminowa-mura, Kaiina-gun, Nagno-ken, Japan.
♥ Quality Magnetics, 1220 West Walnut Street, Compton CA 90220.

specimens were ground to a final thickness of 1 mm. The top and bottom surfaces were finished using diamond wheels and a proprietary protocol by the ceramic finisher. The root-mean-square (RMS) roughness, R_{RMS}, of the final surface finish was 0.303 μm. Figure 2.2 shows the microstructure of the alumina. The average grain size was reported as 1 μm. Additional properties of this alumina reported by the material supplier and Wen are summarized in Table 2.1.

2.2 Measurements of Dielectric Breakdown Voltages

2.2.1 ASTM Standard for Dielectric Breakdown Strength Measurements

American Society for Testing and Materials (ASTM) Standard D149-97a[45] is commonly used to measure the dielectric breakdown strength of a solid insulator at commercial power frequencies. The ASTM standard specifies guidelines on the following: specimen preparation, electrodes, surrounding medium, and the voltage application method with failure criteria.

The Standard recommends test specimens with flat parallel surfaces. Neither the thickness nor the in-plane dimensions are specified; however, the in plane dimension should be relatively large when compared to the electrodes to prevent surface flashover.

Recommended electrodes are opposing cylinders, flat plates, hemispheres, and opposing circular flat plates. The electrodes are normally made from either brass or stainless steel and the surface should be polished and free from irregularities.

A surrounding medium is required to prevent surface flashover and minimize the effects of partial discharges prior to breakdown. It is recommended to use a liquid

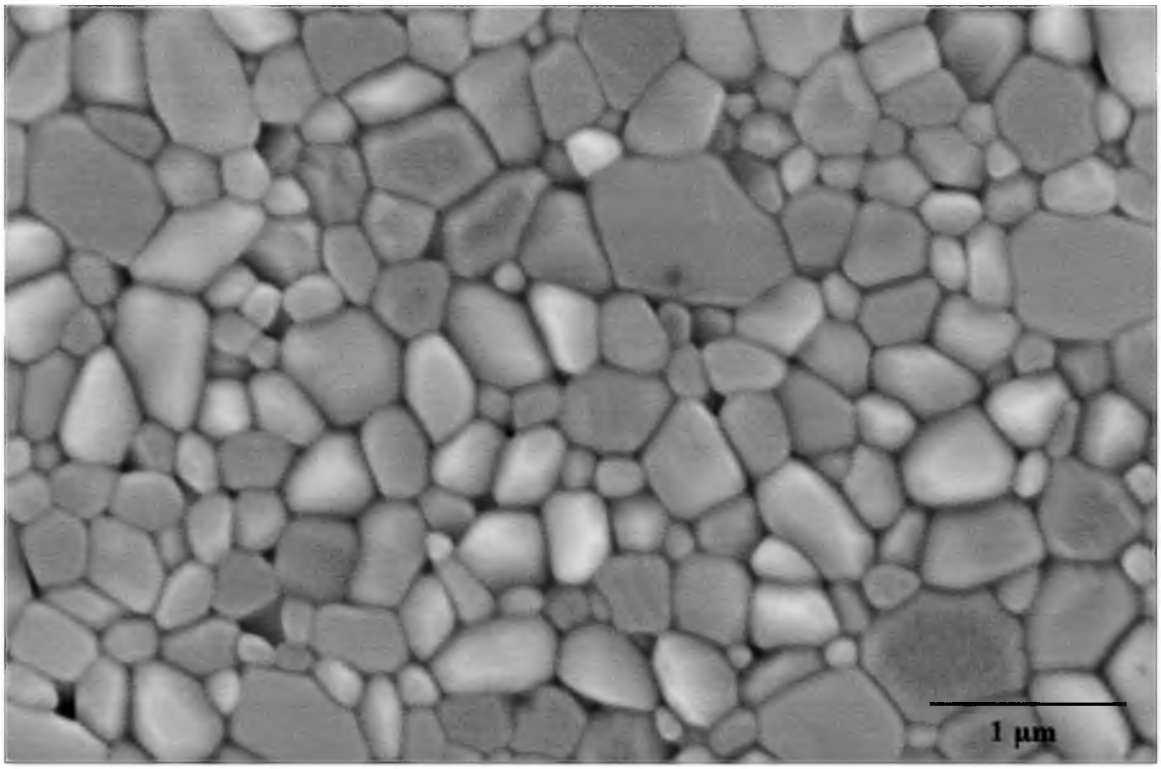

Figure 2.2 SEM image of the microstructure of HPFG alumina.

surrounding medium in a grounded metal container. The dielectric strength of the liquid must exceed that of the test specimen to prevent breakdown of the dielectric liquid. The dielectric liquids should be frequently replaced or filtered to minimize the variance in quality across tests.

An AC test voltage at 60 Hz is applied to the electrodes. The voltage is increased from zero using either a step function or a linear rate until a measured increase in current signifies dielectric breakdown. The current threshold must be set high enough that partial discharges do not trip the breaker, but should not be so high that excessive burning and electrode pitting occur on breakdown.

2.2.2 Drawbacks of the ASTM Dielectric Breakdown Test

The dielectric breakdown test electrodes and procedures outlined in ASTM Standard D149-97a have the following drawbacks: (i) Fixed electrodes, either flat-end cylinders or hemispheres, are not advisable. Breakdown tests produce damage on the electrode surface. This damage can affect electric fields in subsequent tests. (ii) Flat-ended electrodes should be avoided, in general, because electric fields are concentrated along the three-phase contact line, and the magnitude of the field concentration is affected by the edge radius and surface finish. (iii) The ASTM Standard calculates breakdown strengths as the breakdown voltages divided by the specimen thickness, irrespective of the electrode geometry or size. This masks important effects of electric field concentrations, including the scaling of the breakdown strength with electrically-stressed area or volume.

2.2.3 Modified Electrodes and Test Setup

In this study, disposable spherical electrodes with point contact or ring electrodes with line contact were employed to eliminate the drawbacks (i) and (ii) noted above. Ball electrodes were rotated after each test and disposed of after ten tests. Ring electrodes were inspected after each test and disposed of once pitting was evident. A pitted electrode has sharp edges which can scratch and damage the specimen surface. Such damage would affect the specimen surface finish and breakdown voltage. These modifications of the ASTM Standard ensured that the electrode surface near the specimen was pristine and uniform for all testing. These modifications also ensured that the electric field in and around the specimen was maintained the same for all the tests and the electrode surface finish did not affect the breakdown voltage.

Figures 2.3 and 2.4 show schematics of the test setup and the ball electrodes, respectively. Stainless steel ball electrodes were used to investigate the effects of electrode geometry and size on breakdown strength. The upper electrode had a radius, R_1, of 1.5875, 3.175, 4.7625, 6.35, 7.9375, 9.525, 11.1125, or 12.7 mm. The lower electrode radius, R_2, was fixed at 12.7 mm.

Figure 2.5 illustrates the test setup with the ring electrodes. Stainless steel ring electrodes were used to investigate the effects of spatially-distributed electric fields. The electrode contact radius, R_c, was 19.05 mm. The electrode radius of curvature, R_e, was 1.5875 or 12.7 mm for both upper and lower electrodes.

Drawback (iii) of the ASTM Standard was eliminated by defining the breakdown strengths in terms of the maximum electric fields. The definition of breakdown strengths used in this study will be discussed in Section 3.3.

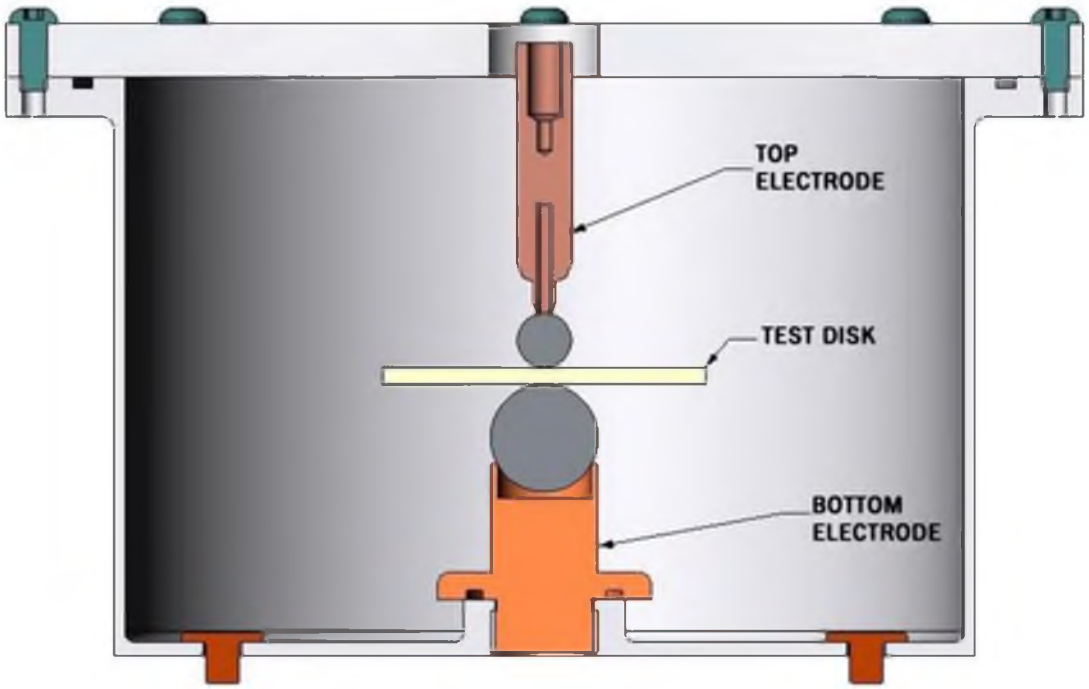

Figure 2.3 A schematic of the test specimen and disposable ball bearing electrodes for measuring breakdown voltage.

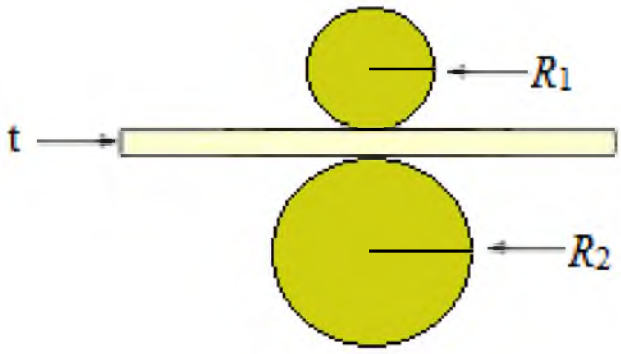

Figure 2.4 A schematic of the test specimen and disposable ball bearing electrodes for measuring breakdown voltage.

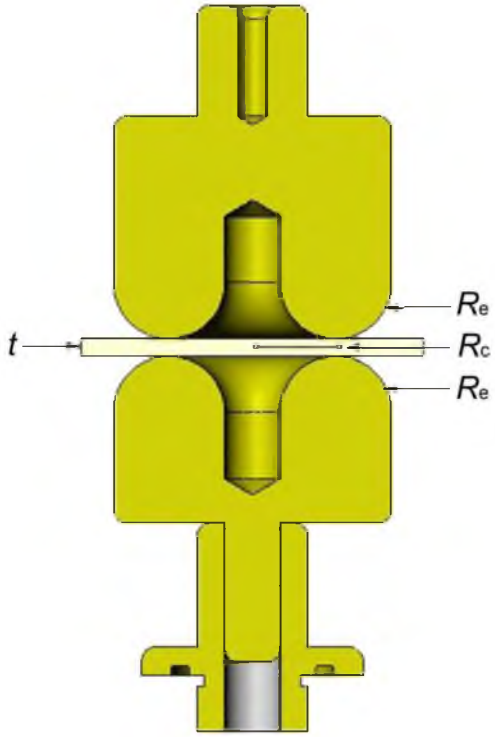

Figure 2.5 A schematic of the test specimen and ring electrodes for measuring breakdown voltage.

2.2.4 Test Procedure

The test specimen was placed between the upper and the lower electrodes. The center of the disk specimen was offset from the points of contact with the electrodes to allow for multiple (6) tests on one specimen. The electrodes and specimen were placed in a polyoxymethylene (POM) fixture to maintain their relative positions. This fixture was then lowered into a cylindrical aluminum tank, which had been filled to 95% capacity with a dielectric liquid. The dielectric liquid was either castor oil or Diala® oil. The liquids were degassed before use to prevent surface flashover.

An AC voltage of 60 Hz was applied to the upper electrode using a power supply (Model 950, Hipotronics, Brewster, NY) with a maximum output of 75 kV. The voltage was ramped at a rate of 2 kV/second starting from 0 kV. The lower electrode was attached to the aluminum tank by means of a wire with alligator clips. The aluminum tank itself was grounded using a grounding hook.

Specimen breakdown was detected by monitoring the current and recording the breakdown voltage, V_b, when the current exceeded 75 mA. The power supply was automatically shut down when the current exceeded the set threshold and the maximum voltage was recorded. The increase in current was typically nonlinear with applied voltage and was accompanied by an audible pop and a visible puncture through the thickness of the specimen. Figure 2.6 shows an image of a commercial-grade alumina specimen after six successful breakdown tests. Figure 2.7 show a typical puncture produced on the surface of the commercial-grade alumina specimen in a dielectric breakdown test. The surface around the puncture showed evidence of local heating and melting of the ceramic.

Figure 2.6 Image of a commercial-grade alumina specimen (radius 12.7 mm, thickness 1 mm) after 6 successful breakdown test.

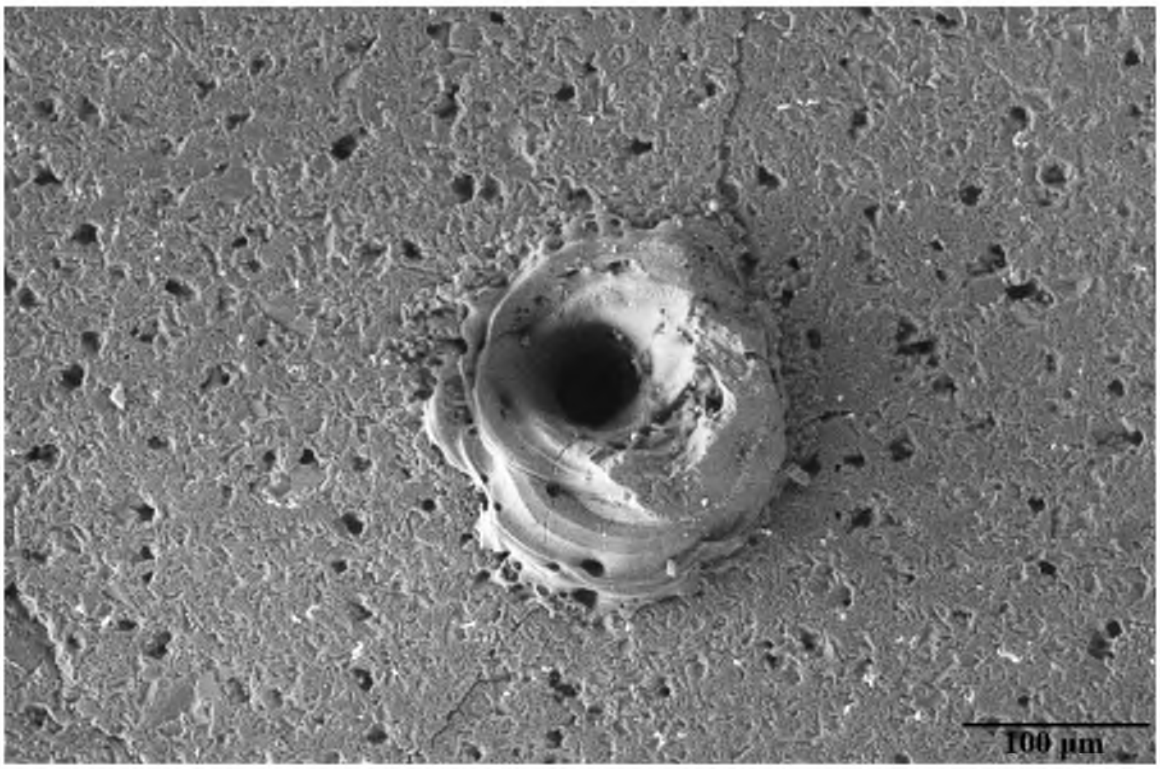

Figure 2.7 SEM image of a typical puncture on the surface of commercial-grade alumina.

After each test, the specimen surface was inspected to ensure that a puncture had occurred. The voltage leads and the dielectric liquid were also inspected for signs of breakdown and contamination. If a puncture was not visible or the test set up exhibited signs of damage or contamination, the data point was not recorded. Each test site was marked to ensure that subsequent tests were not performed at the same location. Twenty breakdown tests on 4 disks were conducted for each test condition defined by the electrodes, liquid medium, and specimen thickness.

The entire experimental setup was housed in a testing cage with an interlocking gate, which much be closed for the power supply to operate. The power supply and the operating controls were located outside of the testing cage.

2.3 Measurements of Dielectric Constants

Both the maximum electric field and the spatial variation of the electric field within the specimen are functions of the dielectric constant of the specimen and the dielectric liquid. Therefore, the dielectric constants of the dielectric liquids and the alumina specimens are needed to accurately compute the electric field using FEA. The dielectric constant, ε_r, is defined as follows:

$$\varepsilon_r = \frac{\varepsilon}{\varepsilon_0} \tag{2.1}$$

In Equation (2.1), ε is the permittivity of the material and ε_0 is the permittivity of free space. The permittivity of free space is 8.8542×10^{-12}F/m. The dielectric constant can be calculated from the capacitance of a disk specimen using the following equation:

$$\varepsilon_r = \frac{Ct}{A\varepsilon_0} \tag{2.2}$$

In Equation (2.2), C is the capacitance, t is the specimen thickness, and A is the area of the electrodes.

Figure 2.8 shows the test chamber, consisting of an aluminum box, specimen cell, and two brass electrodes, that was used to measure capacitance. The temperature within the test chamber was set to 21°C for this study. The capacitance was measured using a time domain spectrometer (TDS) (Model TDDS-1, Imass, Inc., Accord, MA) in the frequency range, 1 to 10,000 Hz. A precision LCR meter (Model 4284A, Hewlett-Packard Co., Palo Alto, CA) was used in the frequency range, 20 Hz to 1 MHz.

Figure 2.9 shows the liquid specimen holder, consisting of a brass lid, a brass cup, and a Teflon® ring which was used to measure the capacitance of castor oil and Diala® oil. The brass cup and lid serve as electrodes, while the Teflon® ring separates the electrodes and contained the liquid specimen. Each electrode has a surface area of 78.54 mm^2. The Teflon® ring affects the measured capacitance and must be accounted for. A correction for the capacitance of the liquid, C_l was made via the following formula:

$$C_l = C - C_o \tag{2.3}$$

In Equation (2.3), C is the total capacitance of the liquid sample and the Teflon® ring and C_o is the capacitance of the Teflon® ring without the oil. The dielectric constant was then calculated using Equation (2.2) with C_l replacing C.

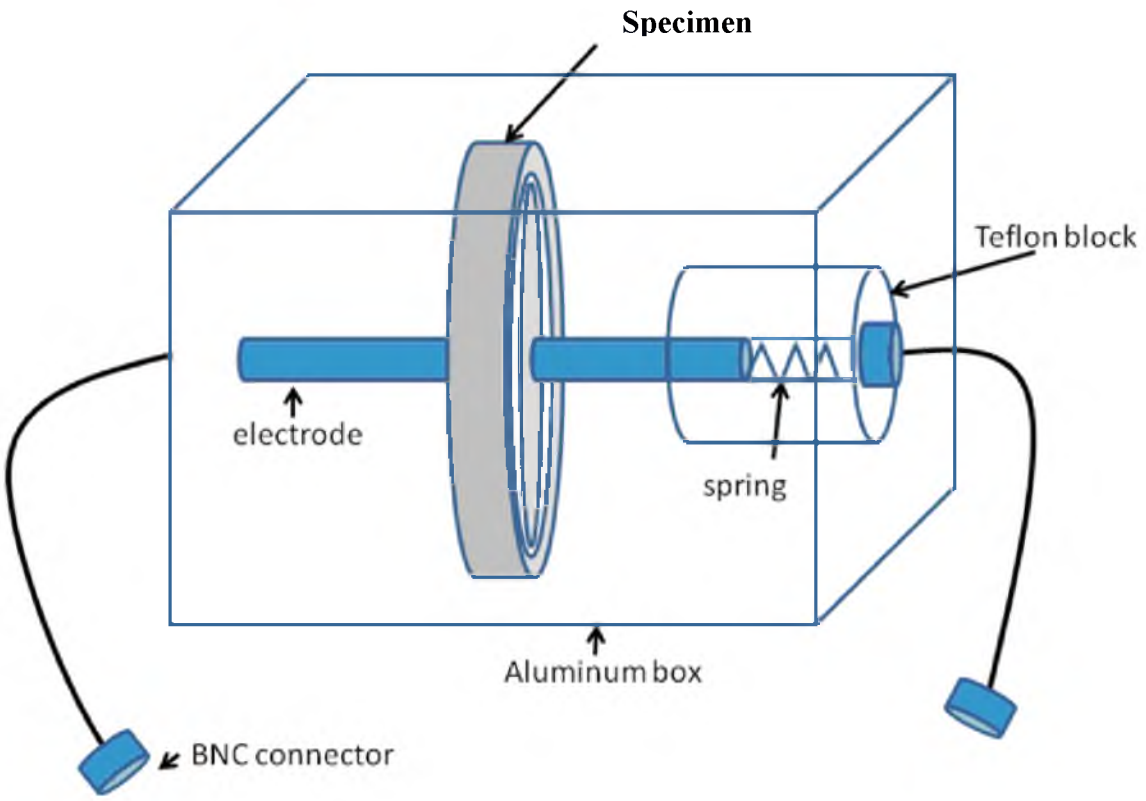

Figure 2.8 Test chamber, specimen cell, and electrodes used in measurements of capacitance.

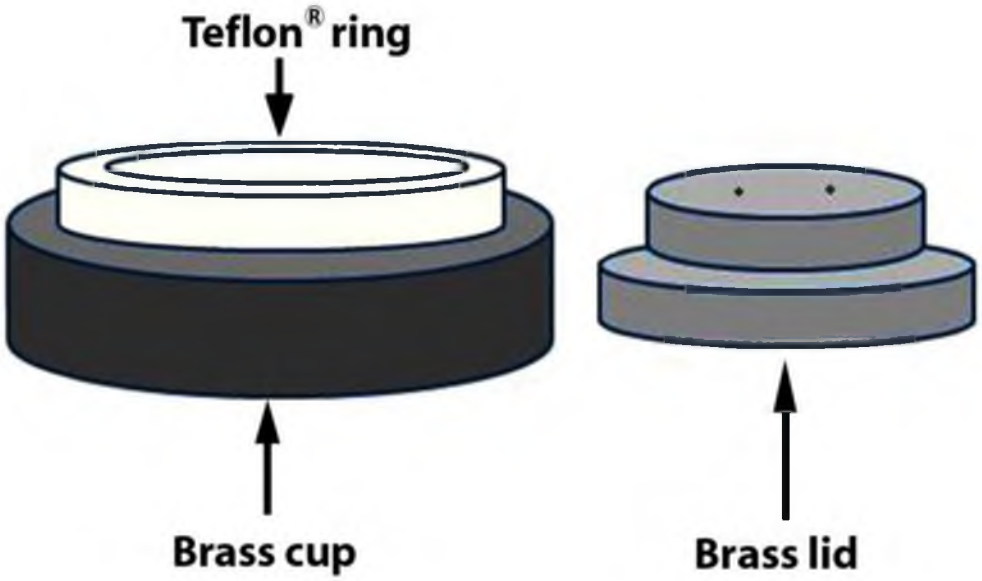

Figure 2.9 Specimen holder used to measure the capacitance of liquids.

To measure the dielectric constant of the alumina disk, both surfaces of the alumina were sputter coated with gold using a SPI-MODULE™ sputter coater. The gold coating served as the electrodes in lieu of a specimen holder. Each electrode has a surface area of 506.71 mm^2.

2.4 Finite Element Analyses of Electric Fields

An axi-symmetrical model was employed in FEA due to the axial symmetry in the experimental setup. Figure 2.10 shows the axi-symmetrical model used to test the convergence of the computed electric field in the specimen. The axi-symmetrical model is more efficient and requires less computational resources than a full 3-D model to obtain the same result.

Previous work by Kim[37] found that there was no difference between an electric currents analysis and an electrostatics analysis. Kim's findings were verified in this study. Therefore, Comsol® was used to solve a stationary electrostatics model. The governing equations in the Comsol® Electrostatics module are as follows:

$$E = -\nabla V \tag{2.4}$$

$$D = \varepsilon_0 \varepsilon_r E \tag{2.5}$$

$$-\nabla^2 V = \frac{\rho}{\varepsilon} \tag{2.6}$$

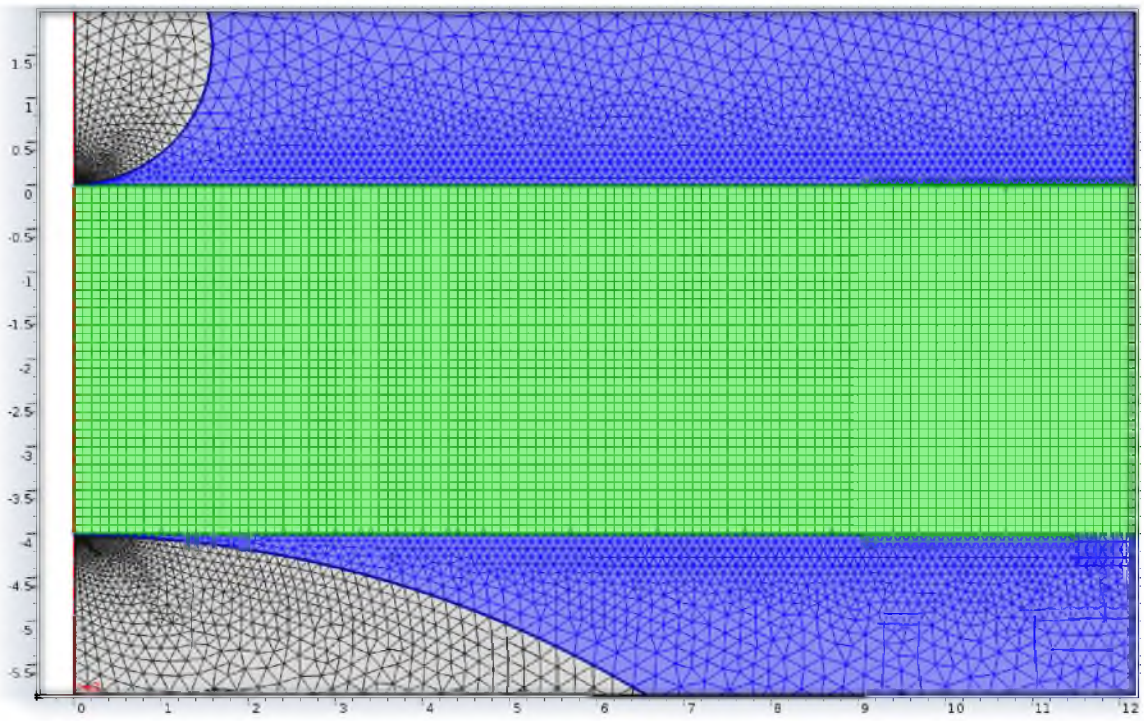

Figure 2.10 Example of the FEA mesh used in element size convergence testing.

where E is the electric field intensity, V is the voltage, D is the electric displacement, ε_0 is the permittivity of free space, ε_r is the relative permittivity, and ρ is the electric charge density. The MUMPS solver was employed in this study. The MUMPS solver uses a direct method to solve systems of linear equations.

Figure 2.11 shows the convergence of the maximum electric field in a specimen (commercial-grade, 38.1 mm radius, 4 mm thickness) with element size for an applied voltage of 75 kV. The convergence test was done with an upper electrode radius of 1.5875 mm in Diala® oil with a 0.0001 mm oil layer between the electrodes and the specimen. Cubic elements with an edge length of h were used to mesh the entire specimen. A free triangular mesh with a maximum element growth rate of 1.1 and a minimum element size of h was used to mesh the dielectric liquid and the electrodes. The maximum electric field increases with decreasing element size. The maximum electric field converges to two decimal places at h = 0.025 mm and to three decimal places at h = 0.015 mm. An element size smaller than h = 0.01 mm led to restrictively long computation times. Therefore, a fine mesh was only used near the contact point where the maximum electric field as well as the greatest change in electric field occur. A coarser mesh was used away from the contact point and did not impact the value of maximum electric field or the change in electric field along the radial directions or through the thickness but greatly reduced computation times.

Thin layers of dielectric liquid were placed between the electrodes and the specimen to prevent poor element geometry at the contact points and also mimic the real situation where both electrode and ceramic surfaces are wetted by the dielectric liquid. The convergence of electric field within the specimen with respect to the thickness of the dielectric liquid layer is shown in Figure 2.12. The convergence was tested with an upper

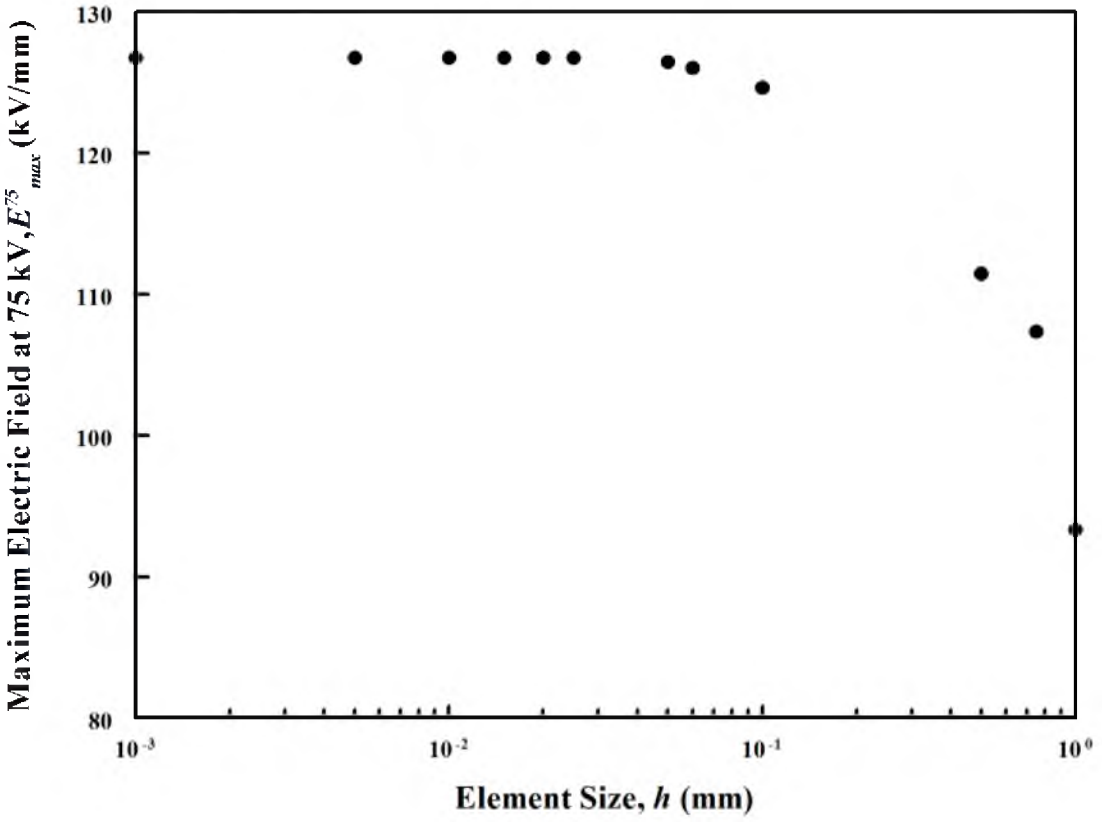

Figure 2.11 Convergence of maximum electric field with element size.

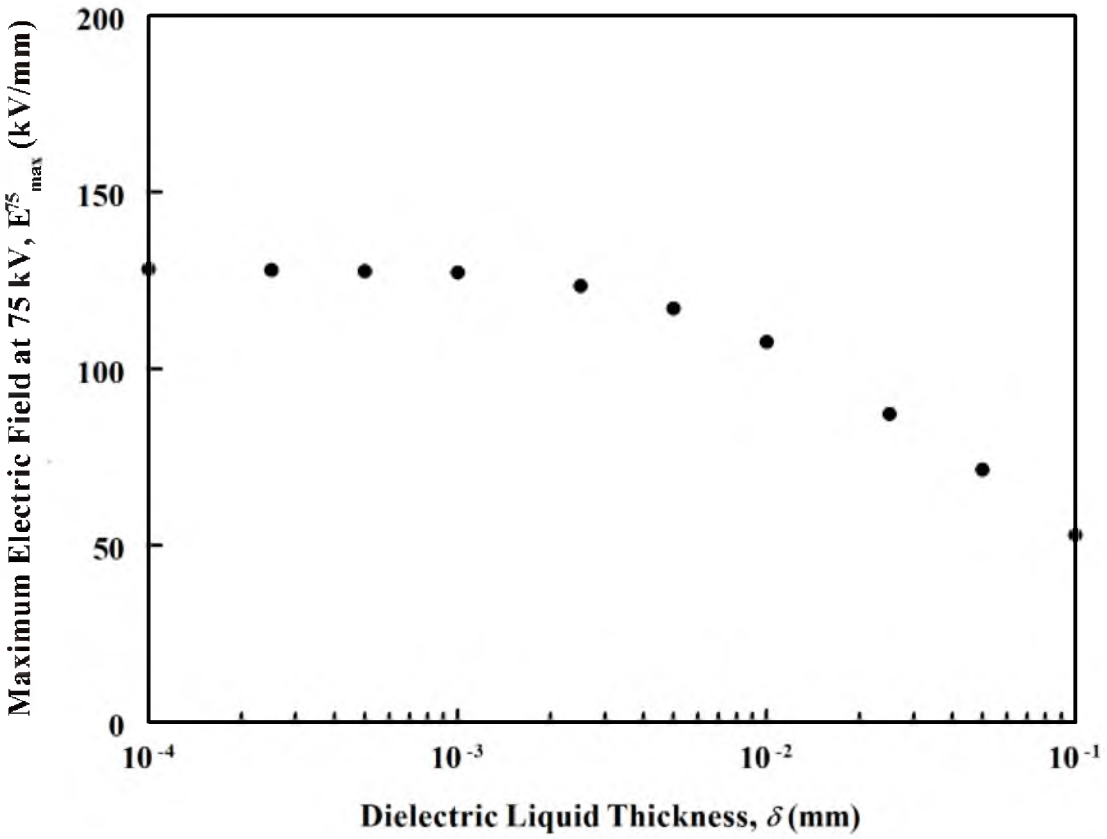

Figure 2.12 Convergence of maximum electric field with oil layer thickness.

electrode radius of 1.5875 mm in Diala® oil with an element size of 0.01 mm. The maximum electric field increases with decreasing dielectric liquid layer thickness. The maximum electric field converges to two decimal places at δ = 0.001 mm.

Figure 2.13 shows the mesh of the axi-symmetrical FEA model used in this study. The thickness of the dielectric liquid layer was δ = 0.0001 mm. The element sizes in the radial direction are 0.001 mm from r = 0.0 to 0.1 mm, 0.01 mm from r = 0.1 to 1.1 mm, 0.1 mm from r = 1.1 to 10.1 mm, and 1.0 mm from r = 10.1 to 38.1 mm. The element sizes through the thickness of the specimens were 0.001 mm from z = 0 to 0.1 mm, 0.005 mm from z = 0.1 to 3.9 mm, and 0.001 mm from z = 3.9 to 4 mm.

The validity of the FEA was established by calculating the maximum electric field in a dielectric plate placed between a sphere and a plane electrode and comparing the results with values reported in the literature. These results are presented in Section 3.2.1.

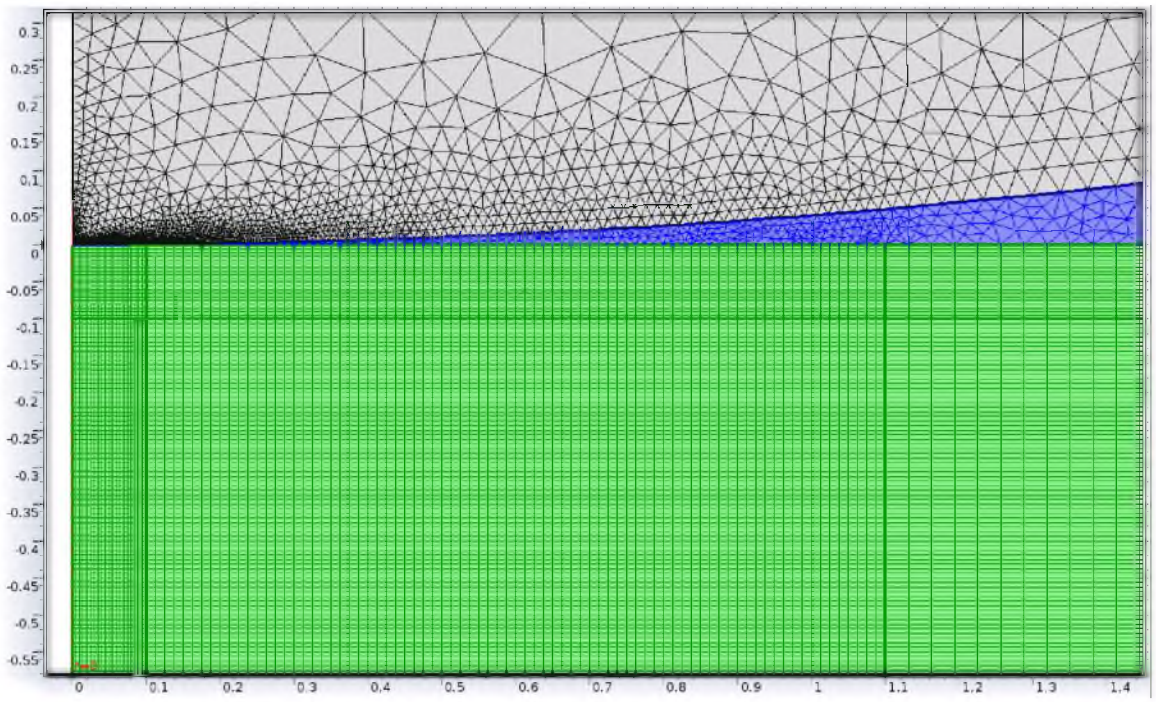

Figure 2.13 Close of up of the FEA mesh used in this study near the contact point between the upper electrode and the specimen surface.

CHAPTER 3

EXPERIMENTAL RESULTS

3.1 Dielectric Constants

3.1.1 Dielectric Liquids

Figures 3.1 and 3.2 show plots of the dielectric constant as a function of frequency for castor oil and Diala® oil, respectively. The average dielectric constants at 60 Hz and 21°C are 4.6 ± 0.13 and 2.3 ± 0.06 for castor oil and Diala® oil, respectively. The dielectric constant of both liquids were relatively insensitive to the applied frequency.

3.1.2 Dielectric Solids

Figures 3.3 and 3.4 show plots of the dielectric constant as a function of frequency for the commercial-grade alumina and the HPFG alumina, respectively. The average dielectric constants at 60 Hz and 21°C were 9.3 ± 0.12 and 9.7 ± 0.16 for the commercial-grade alumina and the HPFG alumina, respectively. Li et al.[46] have attributed the increase in dielectric constant with increasing alumina content to interfacial polarization. The measured dielectric constant of the commercial-grade alumina is slightly larger than the value of $\varepsilon_r = 9.1$ reported on the material supplier data sheet. The dielectric constants of both aluminas were relatively insensitive to the applied frequency. Table 3.1 summarizes

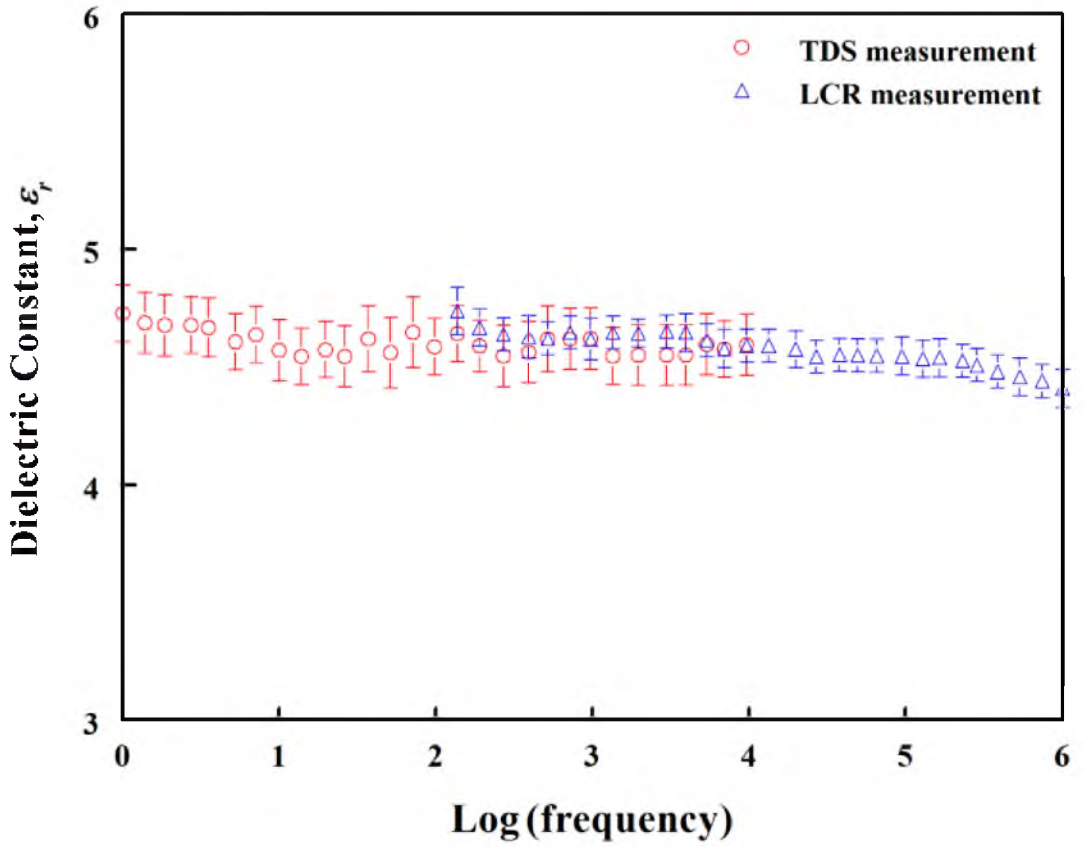

Figure 3.1 Dielectric constant of castor oil plotted as a function of frequency from 1 Hz to 1 MHz.

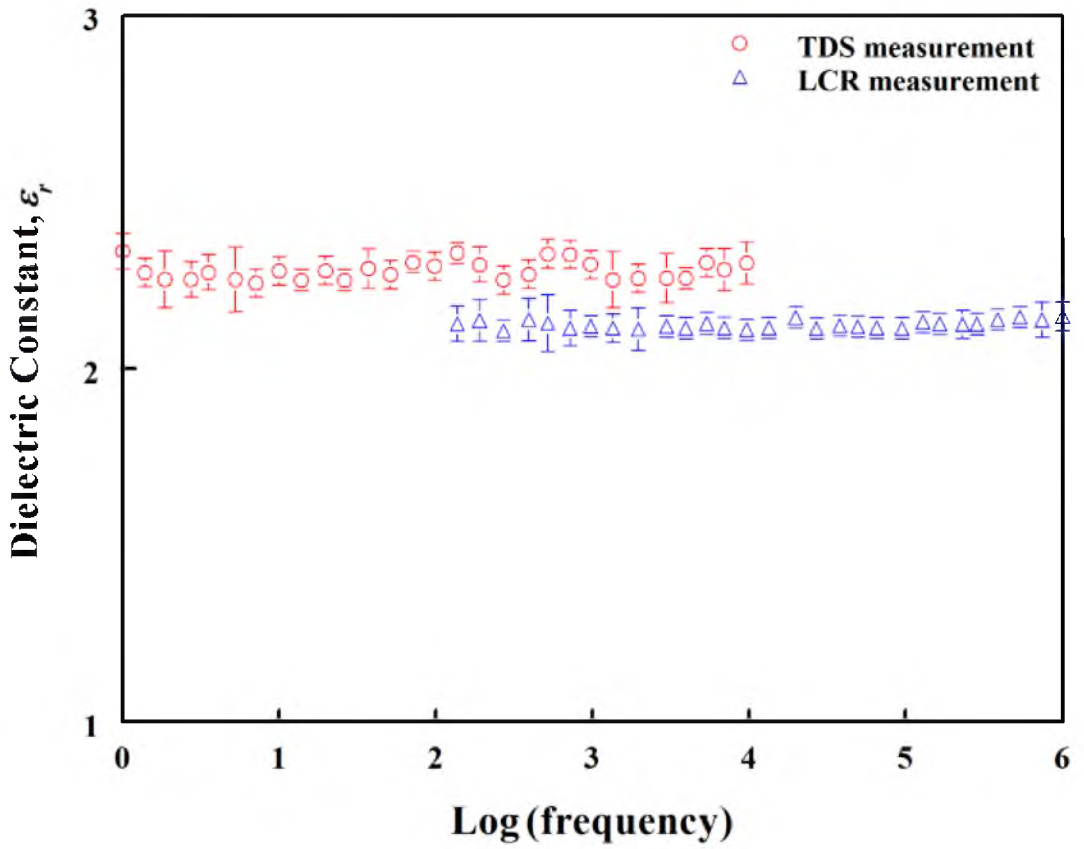

Figure 3.2 Dielectric constant of Diala® oil plotted as a function of frequency from 1 Hz to 1 MHz.

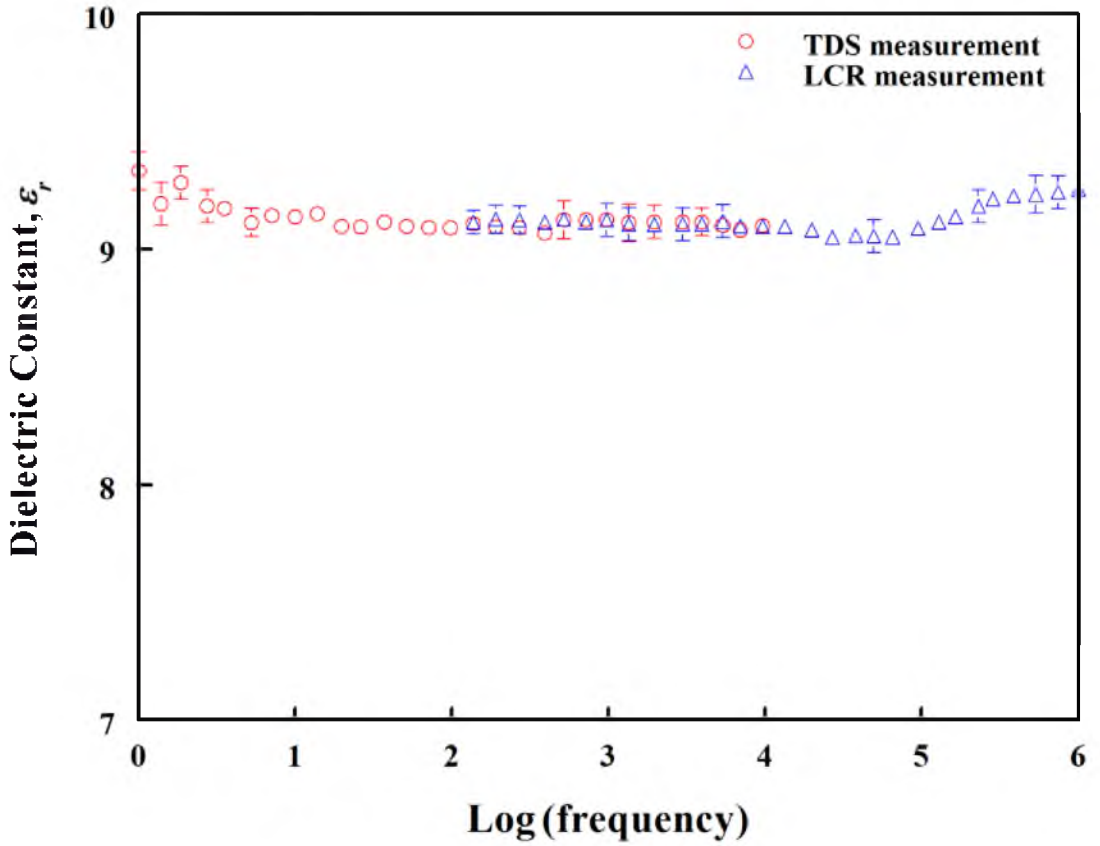

Figure 3.3 Dielectric constant of commercial-grade alumina plotted as a function of frequency from 1 Hz to 1 MHz.

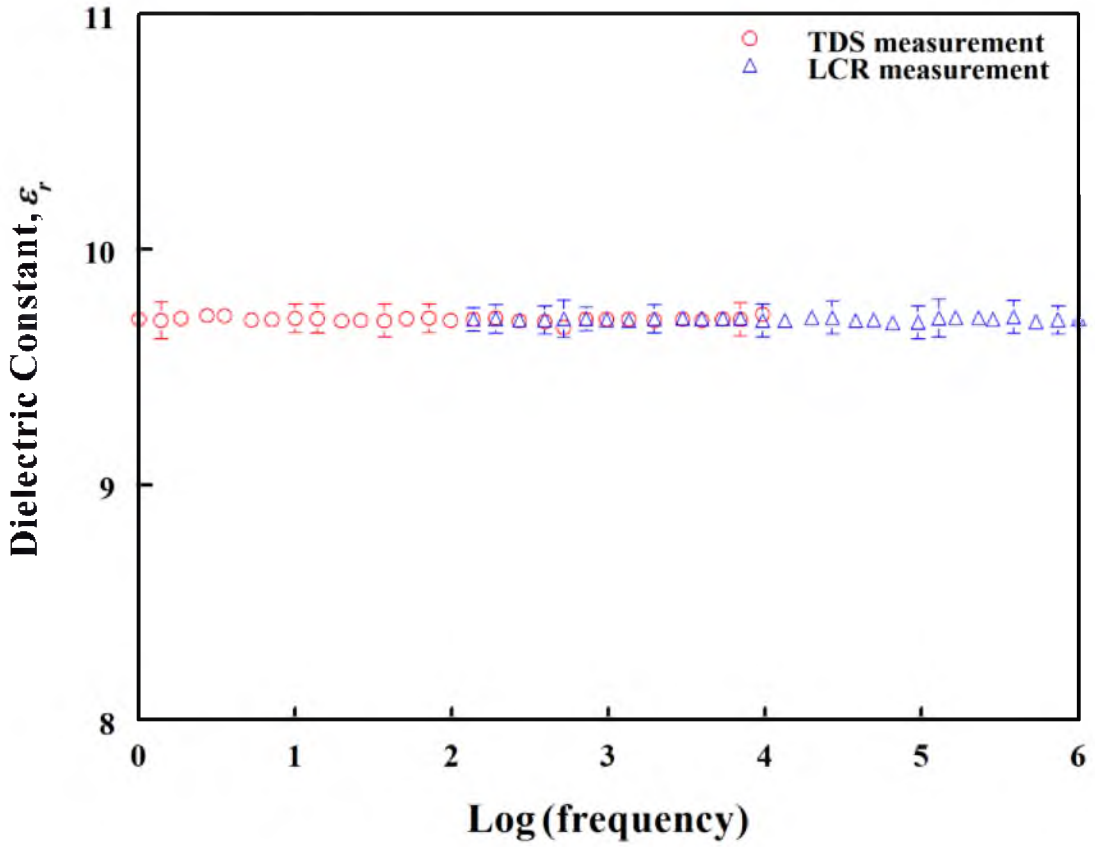

Figure 3.4 Dielectric constant of HPFG alumina plotted as a function of frequency from 1 Hz to 1 MHz.

Table 3.1 Measured dielectric constants at 60 Hz and 21°C.

Material	ε_r
castor oil	4.6 ± 0.13
Diala® oil	2.3 ± 0.06
Alumina (commercial-grade)	9.3 ± 0.12
Alumina (HPFG)	9.7 ± 0.16

the measured dielectric constants.

3.2 FEA Results

3.2.1 Validation of FEA Modeling

In order to validate the FEA modeling used in this study, the normalized electric field in a dielectric/electrodes system with known numerical solution was analyzed. Binns and Randal[47], Takuma and Kawamoto[48], and Poli[49] have all numerically analyzed the electric field on the surface of a dielectric plate in contact with a spherical electrode using methods such as finite difference method[50] and charge simulation method[47-50]. The model used in their analysis consists of a spherical electrode in contact with the top surface of dielectric plate (ε_d) immersed in a dielectric liquid (ε_l). The spherical electrode was maintained at a constant surface potential V and the bottom surface of the dielectric plate was grounded. Table 3.2 lists the FEA and literature values of the normalized maximum electric field within the dielectric plate for three different values of ε_s, where $\varepsilon_s = \frac{\varepsilon_d}{\varepsilon_l}$. All calculations were done with the electrode radius equal to the dielectric plate thickness ($R_1 = t$). The normalized electric field values calculated by FEA were in agreement with the values reported in the literature. The literature studies considered a dielectric plate infinite

Table 3.2 Normalized maximum electric field on the surface of a dielectric plate in contact with a spherical electrode.

$\frac{R_1}{t}$	ε_s	FEA	Binns and Randall[47]	Takuma and Kawamoto[48]	Poli[49]
1	1	1.78	1.77	1.82	1.77
1	2	2.39	2.4	2.38	2.38
1	4	3.52	3.45	3.86	3.53

in in-plane dimensions, while the FEA study modeled a disk of finite radius, R = 30 mm. Additional FEA calculations for R = 60 mm and R =120 mm showed no significant change in the maximum electric field. This finding indicated that the in-plane boundary conditions of the ceramic specimen did not affect either the maximum electric field or the radial variation of the electric field as long as $R >> t$.

3.2.2 Electric Field Distributions in Test Series A

Test series A used commercial-grade alumina disks with a radius of 38.1 mm and a thickness of 4 mm in castor or Diala® oil with stainless steel ball electrodes. The top electrode radius, R_1, was 1.5875, 3.175, 4.7625, 6.35, 7.9375, 9.525, 11.1125, or 12.7 mm while the bottom electrode radius, R_2, was fixed at 12.7 mm. This test series was designed to test the effect of top electrode radius and the dielectric constant of the dielectric liquid on electric field distributions and breakdown strengths of the specimens.

3.2.2.1 Electric Field Distributions in Castor Oil

Figure 3.5 shows plots of the normalized electric field, $\frac{E(r)}{\bar{E}}$, as a function of the normalized radial position, r/R, on the top surface of a specimen. r is the radial position, R is the radius of the specimen, $E(r)$ is the electric field calculated by FEA at the radial position r, and $\bar{E}$ is the nominal thickness-averaged electric field, $\bar{E} = \frac{V}{t}$, where V is the applied voltage and t is the specimen thickness. The FEA calculations were performed using an applied voltage of 75 kV. The maximum electric field in the specimen occurred at the contact point between the specimen and the top electrode. The electric field decreased with increasing radial distance. The maximum normalized electric field increased with decreasing electrode radius from 1.21 for R_1 = 12.7 mm to 4.39 for R_1 = 1.5875 mm. The gradient in the normalized electric field increased with decreasing top electrode radius.

Figure 3.6 shows the electric field variations on the bottom surface of a specimen. The electric field decreased with increasing radial distance. The maximum normalized electric field increased with increasing top electrode radius from 0.54 for R_1 = 1.5875 mm to 1.21 for R_1 = 12.7 mm. For R_1 = 12.7 mm, the electric fields on the top and the bottom surfaces were identical. The gradient in normalized electric field was independent of top electrode radius.

Figure 3.7 shows the electric field variations through the thickness of a specimen at its center. For R_1 = 12.7 mm, the electric field variation through the thickness was symmetrical about the mid-thickness of the specimen with the highest values located at the surfaces and the lowest value occurring at the mid-thickness. For all other top electrode radii, the electric fields were asymmetrical with respect to the mid-thickness of the

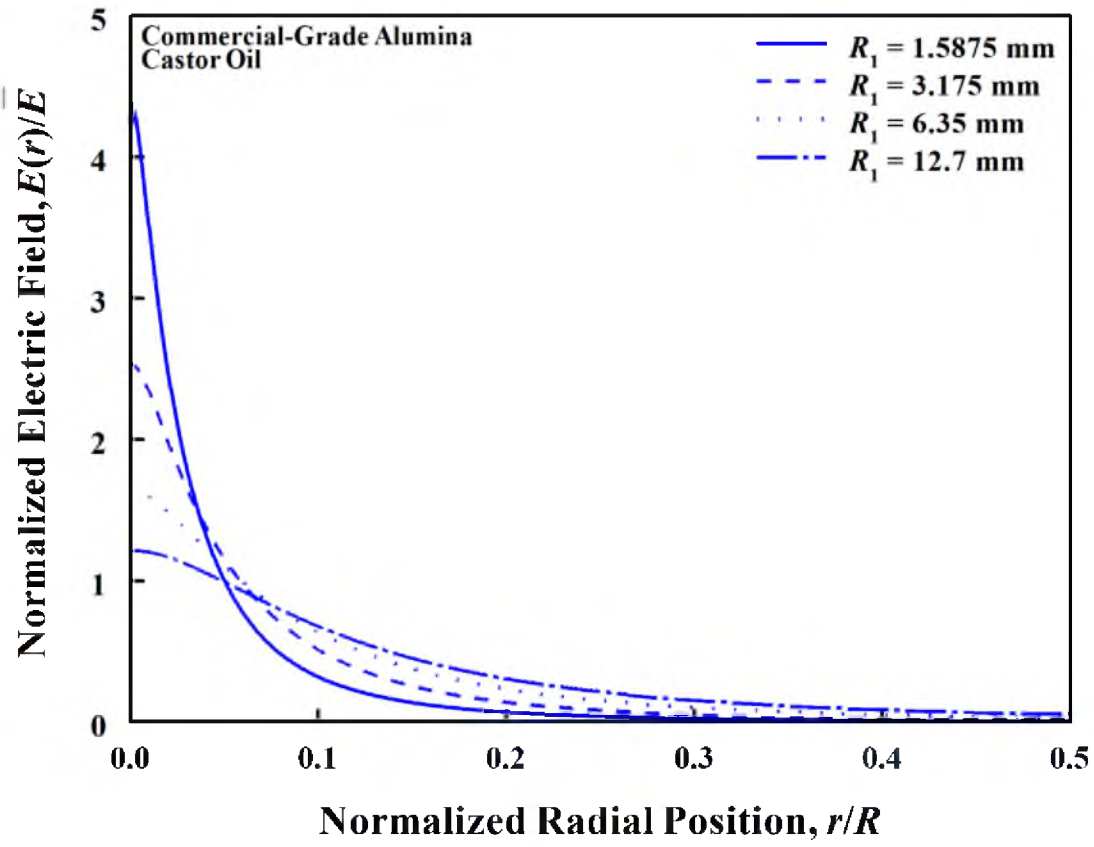

Figure 3.5 Normalized electric field plotted as a function of normalized radial position on the top specimen surface for different top ball electrode radii.

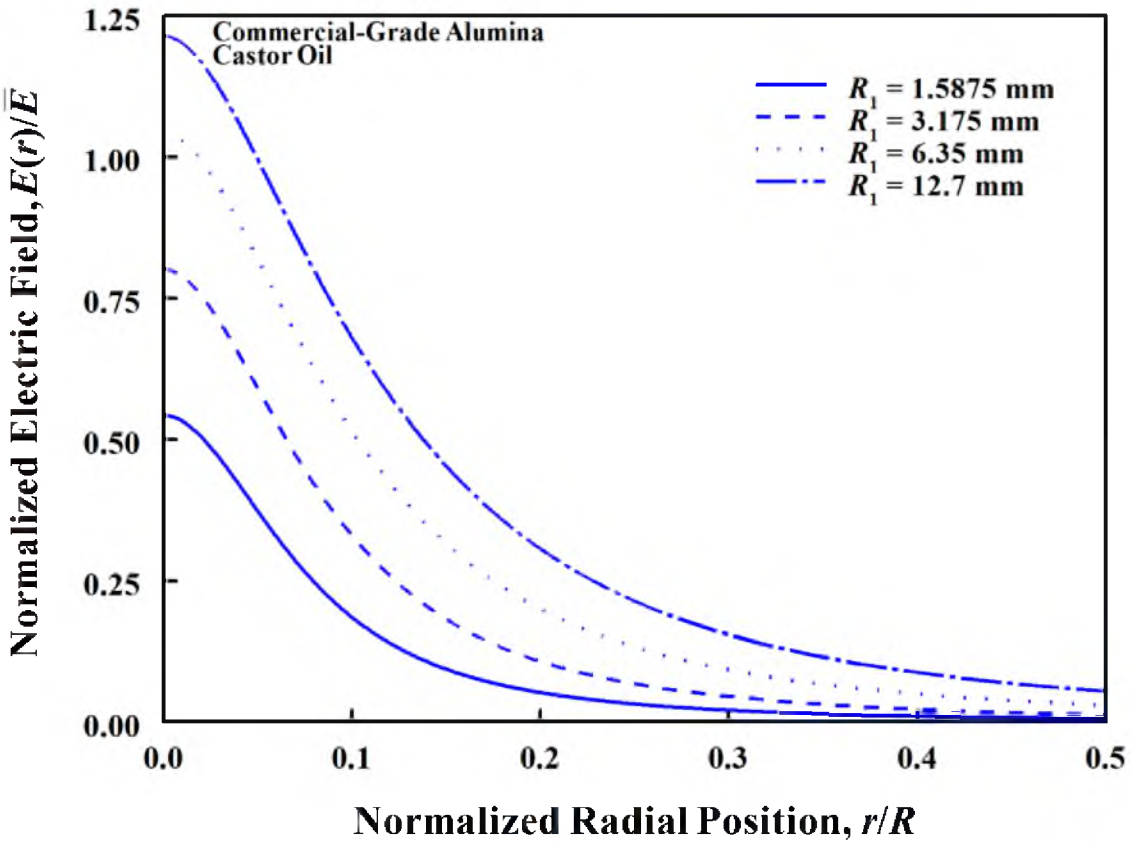

Figure 3.6 Normalized electric field plotted as a function of normalized radial position on the bottom specimen surface for different top ball electrode radii.

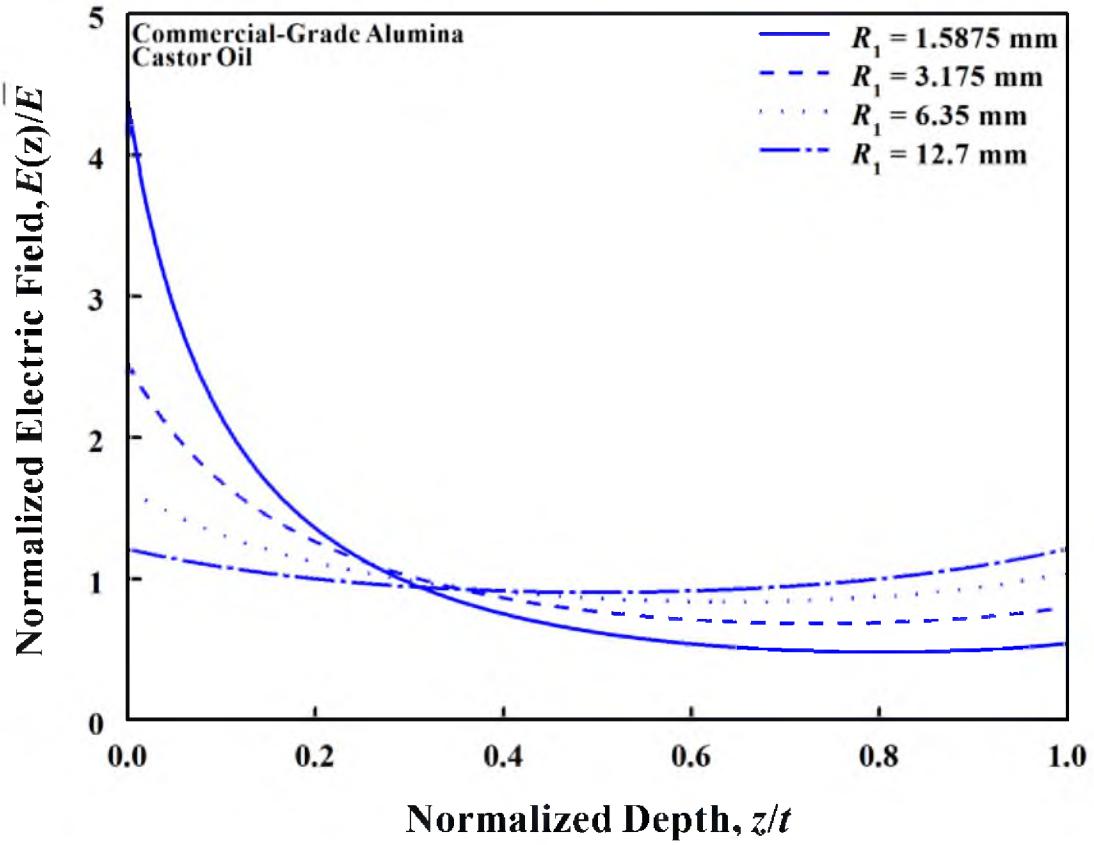

Figure 3.7 Normalized electric field plotted as a function of normalized depth at the center of a specimen for different ball electrode radii.

specimen. The gradient in the normalized electric field was increased with decreasing top electrode radius.

3.2.2.2 Electric Field Distributions in Diala® Oil

Figures 3.8, 3.9, and 3.10 show the normalized electric field variations in Diala® oil on the top surface, bottom surface, and through the thickness, respectively. The trends in electric field were the same as in castor oil. For the same top electrode size, the electric fields were greater in the Diala® oil than in the castor oil. The normalized maximum electric field on the top specimen surface increased from 1.4 to 6.7 as the top ball electrode radius decreased from 12.7 mm to 1.5875 mm. These represent increases of 17 and 55% over the corresponding values in castor oil.

The normalized maximum electric field on the bottom specimen surface increased from .53 to 1.4 as the top ball electrode radius decreased from 12.7 mm to 1.5875 mm. These represent changes of -2 and 17% from the corresponding values in castor oil.

3.2.3 Electric Field Distributions in Test Series B

Test series B used commercial-grade alumina disks with a radius of 38.1 mm and a thickness of 4 mm in Diala® oil with stainless steel ring electrodes. The top and bottom electrodes were identical. The contact circle radius of the electrodes on the disk specimen surfaces, R_c, was 19.05 mm and the electrode radius of curvature of the cross section, R_e, was 1.5875 or 12.7 mm. This test series was designed to test the effect of spatially distributed electric fields on electric field distributions and breakdown strengths of the specimens.

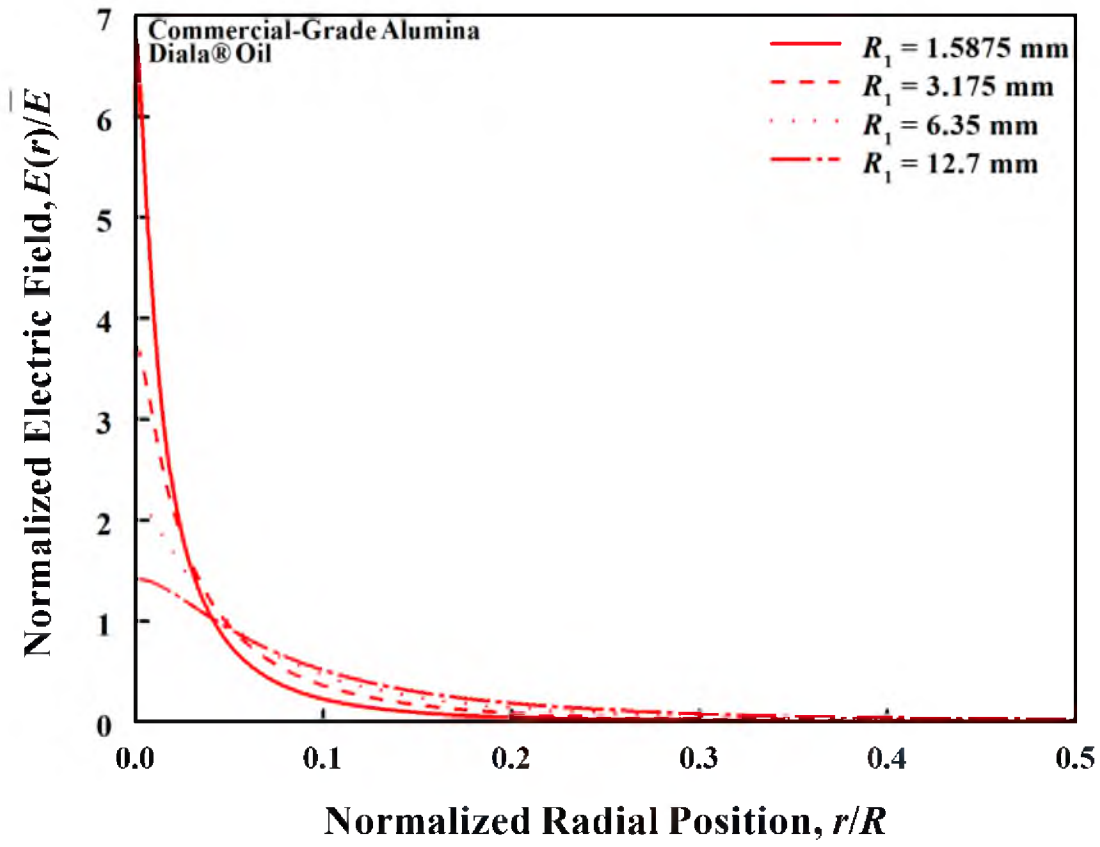

Figure 3.8 Normalized electric field plotted as a function of normalized radial position on the top specimen surface for different top ball electrode radii.

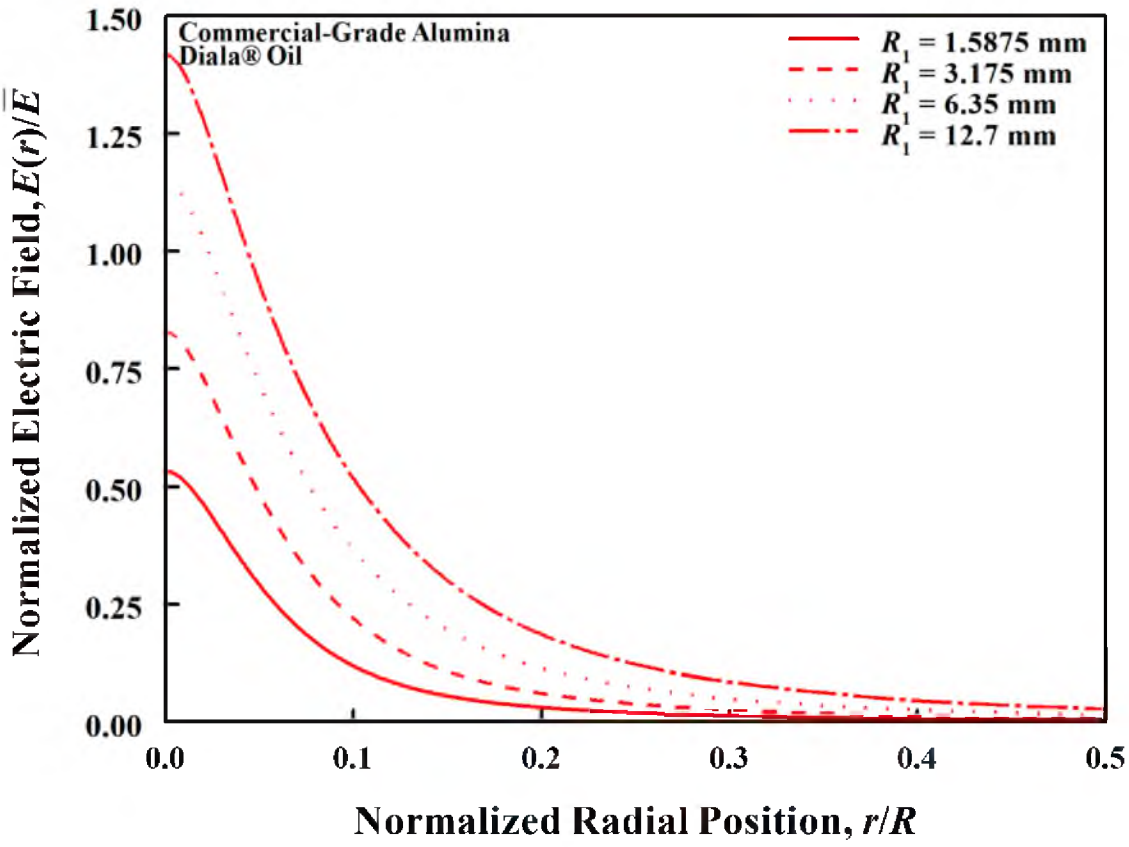

Figure 3.9 Normalized electric field plotted as a function of normalized radial position on the bottom specimen surface for different top ball electrode radii.

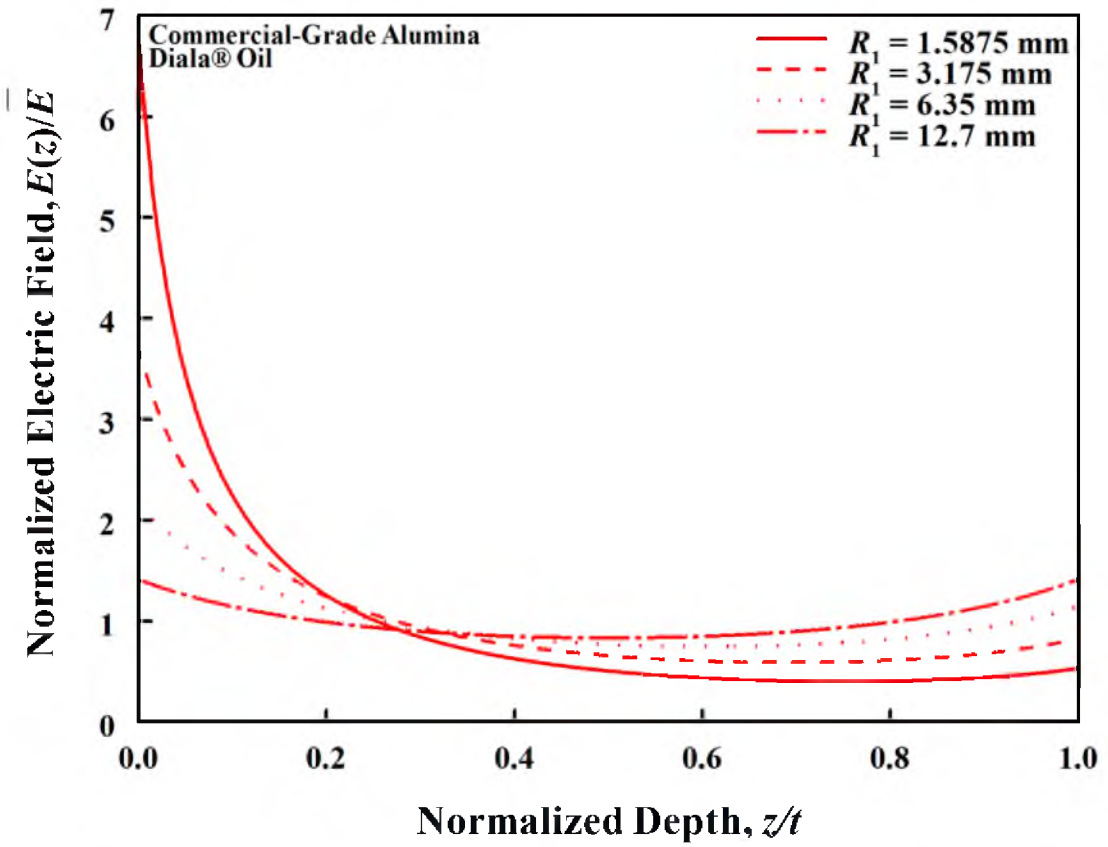

Figure 3.10 Normalized electric field plotted as a function of normalized depth at the center of a specimen for different ball electrode radii.

Figure 3.11 shows the normalized electric field variations on the surface of a specimen. The electric fields on the top and the bottom surfaces were identical because the top and the bottom electrodes had the same radii. The general trends in the electric fields with the ring electrodes were similar to those obtained with the ball electrodes. However, the normalized electric fields at the contact site were larger for the ring electrodes than the ball electrodes of the same radius. The maximum electric field increased with decreasing electrode radius from 1.19 for R_e = 12.7 mm to 2.19 for R_e = 1.5875 mm.

Figure 3.12 shows the normalized electric field variations through the thickness of a specimen at the contact line of the electrodes. The electric field decreased with depth and reached a minimum at the mid-thickness plane. The field distribution with depth was symmetric with respect to the midplane due to the symmetric electrodes employed in this test series.

3.2.4 Electric Field Distributions in Test Series C

Test Series C used commercial-grade alumina disks with a radius of 38.1 mm and thickness of 0.25, 0.50, 1.0, 2.0, or 4.0 mm in Diala® oil with stainless steel ball electrodes. The top electrode radius, R_1, was 3.175 mm and the bottom electrode radius, R_2, was 12.7 mm. This test series was designed to test the effect of specimen thickness on electric field distributions and breakdown strengths of the specimens.

Figure 3.13 shows the normalized electric field variations on the top surface of specimens with varying thicknesses. The maximum normalized electric field increases with increasing specimen thickness from 1.14 for t = 0.25 mm to 3.73 for t = 4.0 mm. Thus, for thin specimens, the maximum electric field approached the nominal electric field.

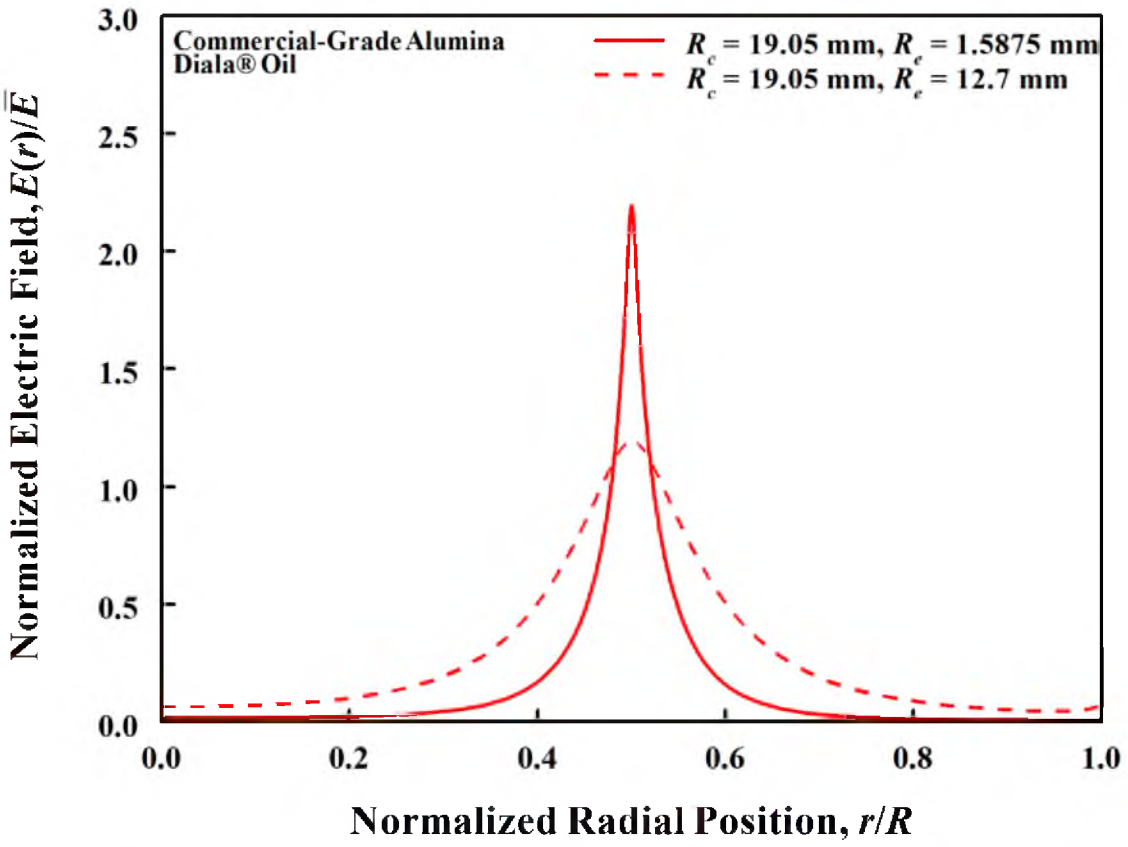

Figure 3.11 Normalized electric field plotted as a function of normalized radial position on the specimen surface for different ring electrode radii.

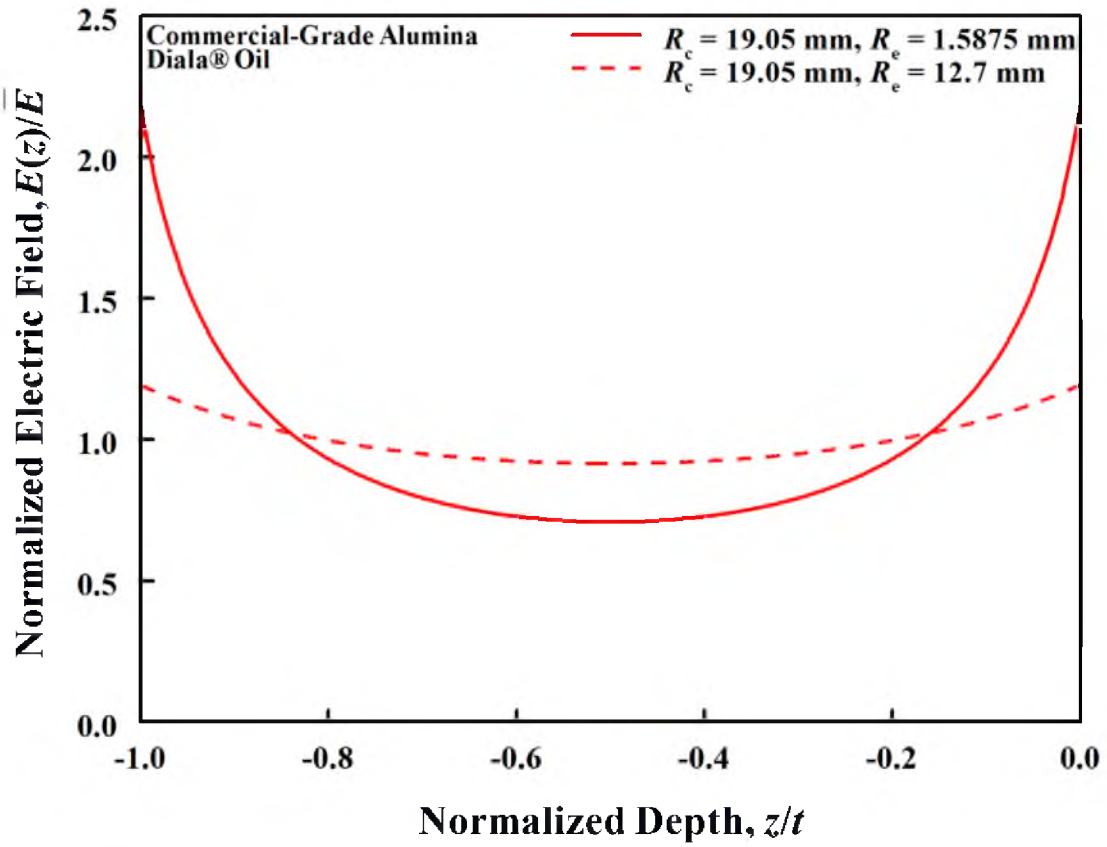

Figure 3.12 Normalized electric field plotted as a function of normalized depth on the contact line of a specimen for different ring electrode radii.

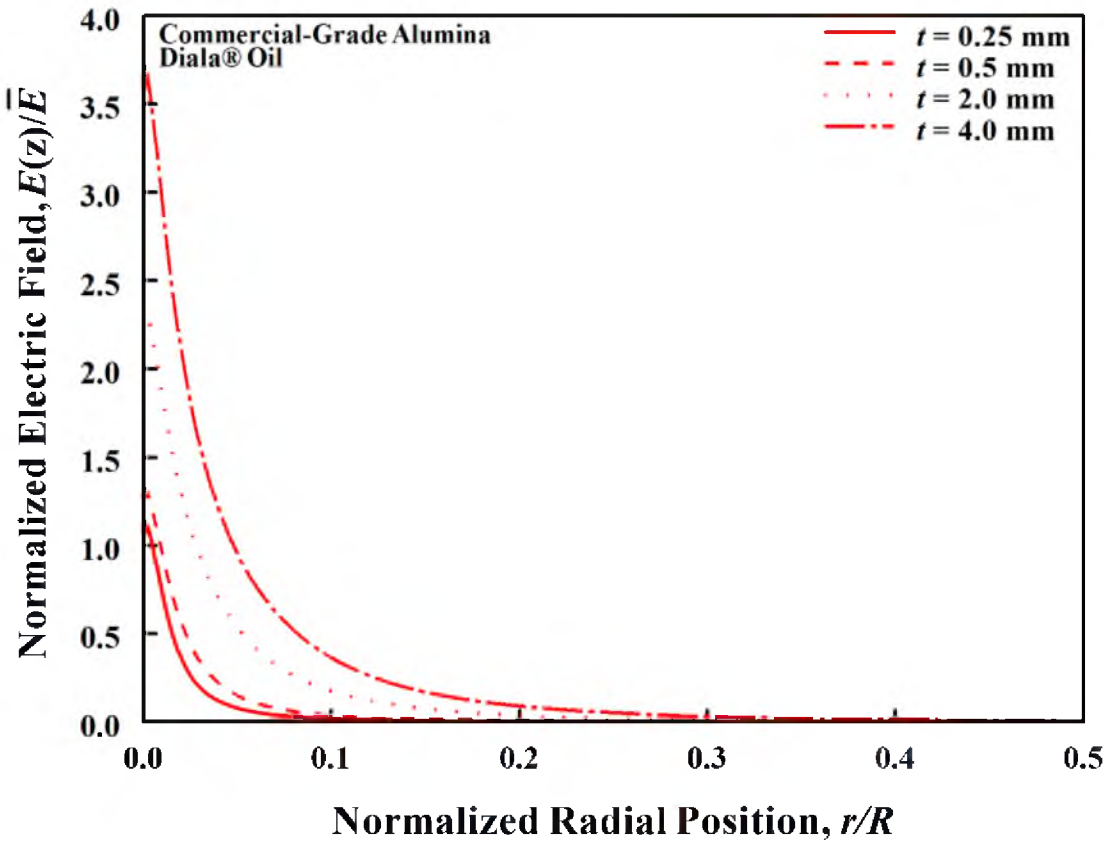

Figure 3.13 Normalized electric field plotted as a function of normalized radial position on the top specimen surface for different specimen thicknesses obtained with ball electrodes (R_1 = 3.175 mm, R_2 = 12.7 mm).

Figure 3.14 shows the normalized electric field variations along a radius on the bottom surface of specimens with varying thicknesses. The maximum normalized electric field increased with decreasing specimen thickness from 0.83 for t = 4.0 mm to 0.92 for t = 0.25 mm. The gradient in the normalized electric field increased with decreasing specimen thickness.

Figure 3.15 shows the normalized electric field variations through the thickness of specimens with varying thicknesses at their center. The asymmetry of the normalized electric field about the mid-thickness point increases with increasing specimen thickness. The gradient in the normalized electric field increased with increasing specimen thickness.

3.2.5 Electric Field Distributions in Test Series D

Test series D used both commercial-grade and HPFG disk specimens with a radius of 12.7 mm and a thickness of 1 mm in Diala® oil. Stainless steel ball electrodes were used. The top electrode radius, R_1, was 1.5875, 3.175, 6.35, or 12.7 mm while the bottom electrode radius, R_2, was fixed at 12.7 mm. This test series was designed to test the effect of alumina content on electric field distributions and breakdown strengths of the specimens.

Figures 3.16 and 3.17 show the normalized electric field variations on the top surface of commercial-grade alumina and HPFG alumina, respectively. The electric fields in the commercial-grade alumina and HPFG alumina were nearly identical. For R_1 = 1.5875 mm, the maximum electric field in the HPFG alumina was only 2% higher than in the commercial-grade alumina. For R_1 = 12.7, mm the maximum electric field in the HPFG was 0.4% higher than in the commercial-grade alumina. The maximum electric field in a commercial-grade specimen with a radius of 12.7 mm and a thickness of 1 mm for R_1 =

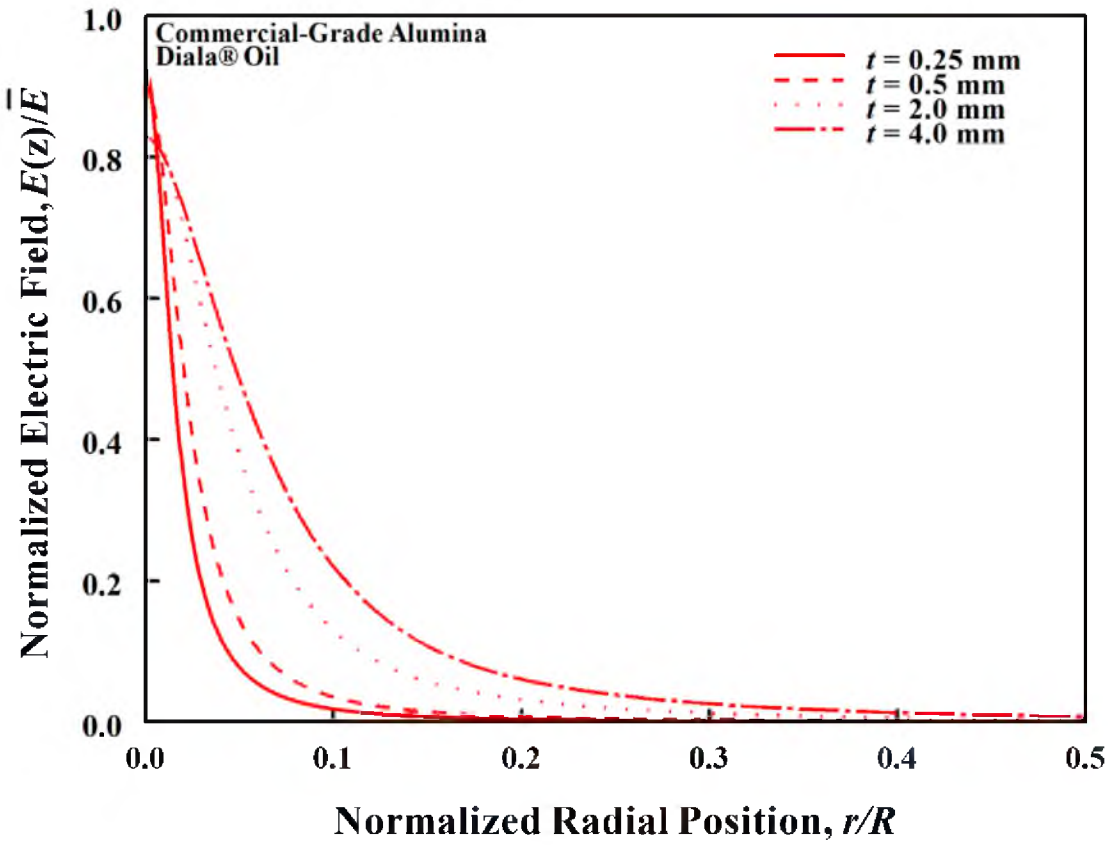

Figure 3.14 Normalized electric field plotted as a function of normalized radial position on the bottom specimen surface for different specimen thicknesses obtained with ball electrodes (R_1 = 3.175 mm, R_2 = 12.7 mm).

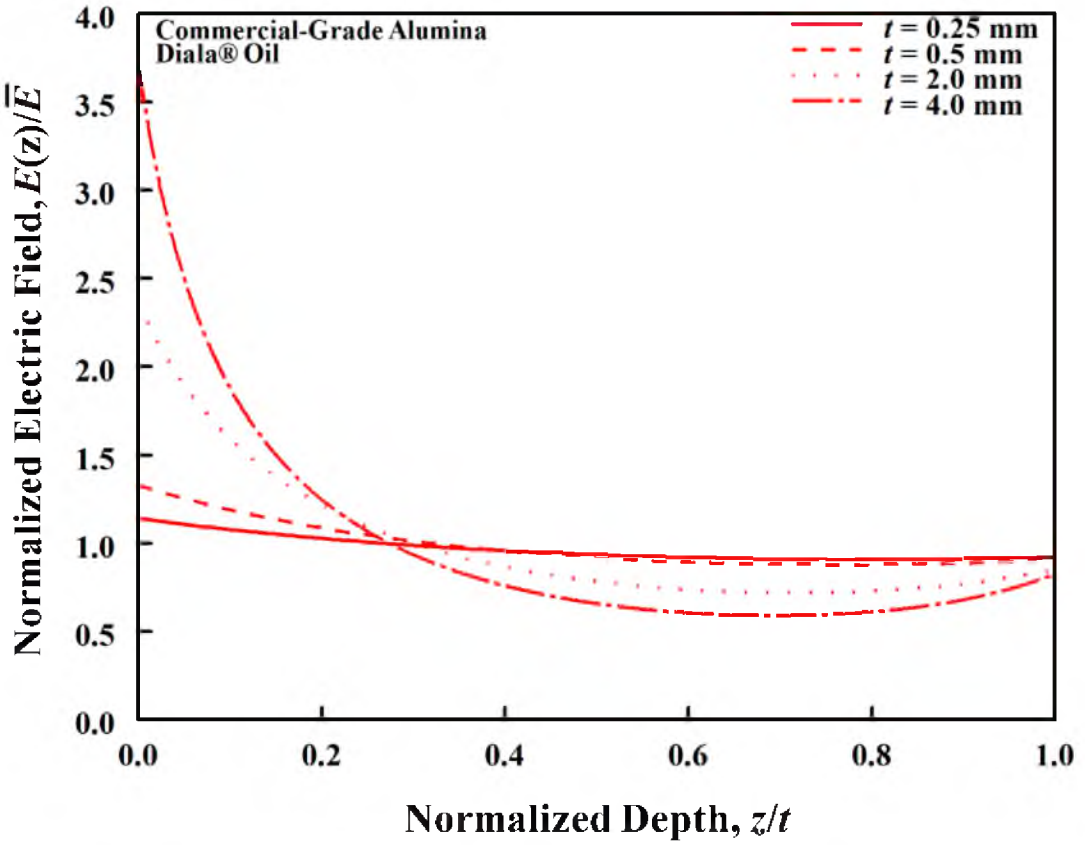

Figure 3.15 Normalized electric field plotted as a function of normalized depth at the center of a specimen for different specimen thicknesses obtained with ball electrodes (R_1 = 3.175 mm, R_2 = 12.7 mm).

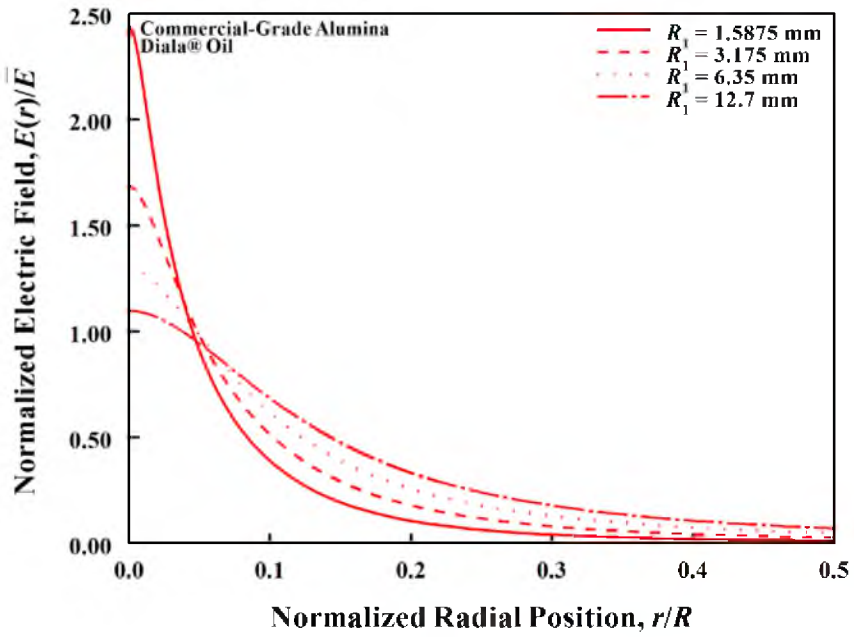

Figure 3.16 Normalized electric field plotted as a function of normalized radial position on the top specimen surface for different top ball electrode radii.

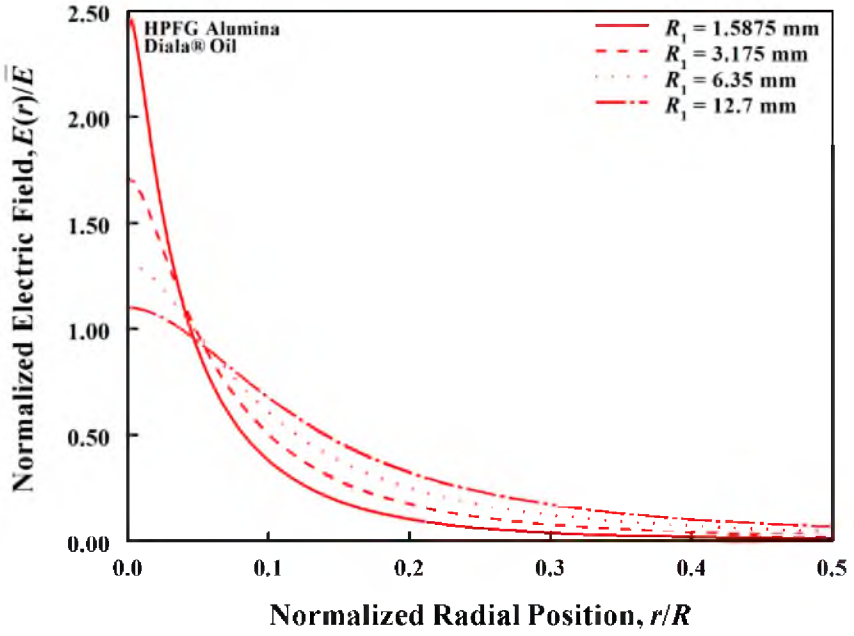

Figure 3.17 Normalized electric field plotted as a function of normalized radial position on the top specimen surface for different top ball electrode radii.

3.175 was the same as in a commercial-grade specimen with a radius of 38.1 mm and a thickness of 1 mm for R_1 = 3.175 mm as tested in series C. Thus, specimen radius has no effect on maximum electric field.

Figures 3.18 and 3.19 show the normalized electric field variations on the bottom surface of the commercial-grade alumina and the HPFG alumina, respectively. For R_1 = 1.5875 mm, the maximum electric field in the commercial-grade alumina was 0.6% higher than in the HPFG alumina. For R_1 = 12.7 mm, the maximum electric field in the HPFG was 0.4% higher than in the commercial-grade alumina.

Figure 3.20 and Figure 3.21 show the electric field variations through the thickness at the contact points of the commercial-grade alumina and the HPFG alumina, respectively. These results were similar to those obtained with test series A (see Figure 3.10).

3.3 Dielectric Breakdown Strength

Figure 3.22 shows plots of the means and the standard errors (two standard deviations) of the breakdown voltage, $\overline{V_b}$, as functions of the top electrode radius for ball and ring electrodes. In both dielectric liquids, the mean breakdown voltage initially increased with increasing electrode radius, but then plateaued and eventually decreased for the largest electrode. The mean breakdown voltages were higher in castor oil for all ball electrode radii. The mean breakdown voltage also increased with increasing ring electrode radius. However, the degree of change in breakdown voltage with electrode radius was much greater for the ball electrodes than it was for the ring electrodes.

A breakdown field, E^b_{max}, was calculated from the breakdown voltage, V_b, using the following equation:

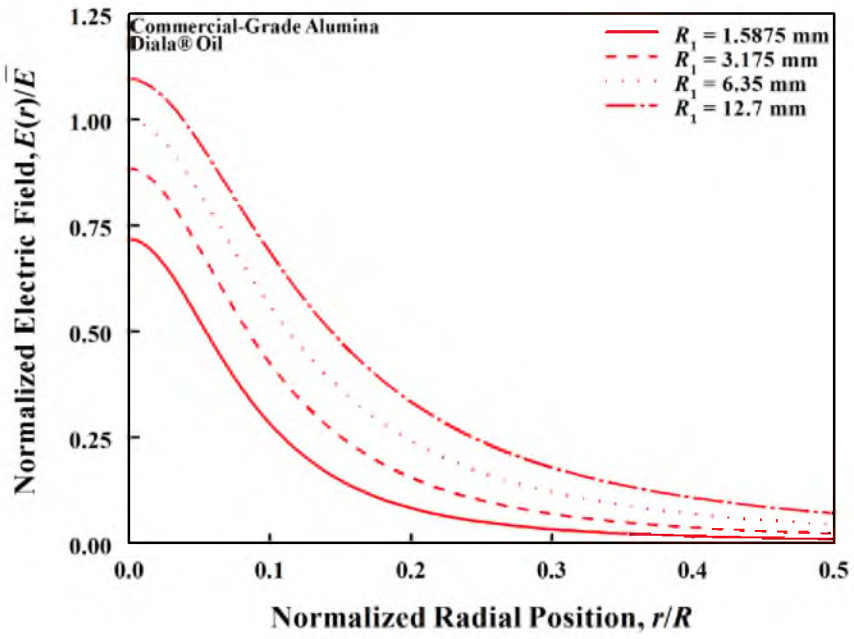

Figure 3.18 Normalized electric field plotted as a function of normalized radial position on the bottom specimen surface for different top ball electrode radii.

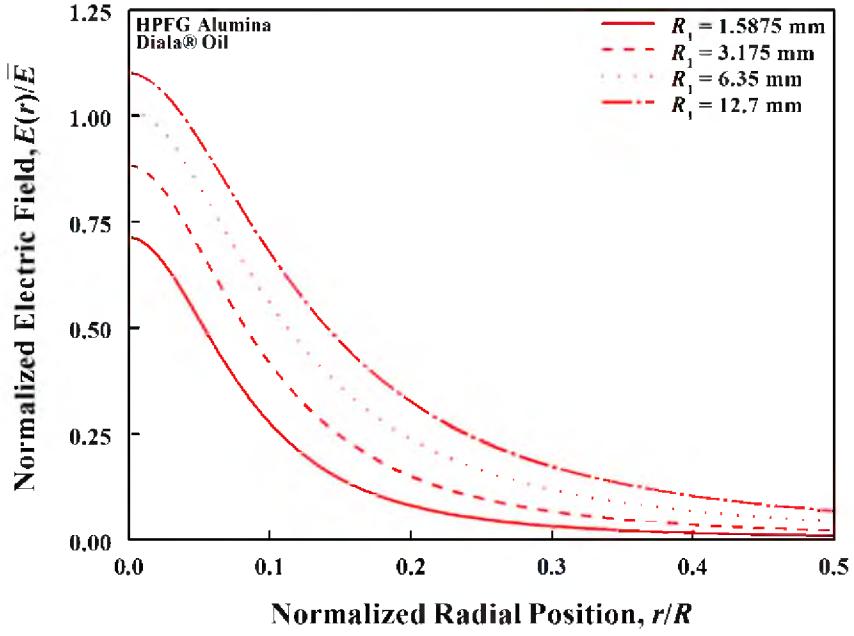

Figure 3.19 Normalized electric field plotted as a function of normalized radial position on the bottom specimen surface for different top ball electrode radii.

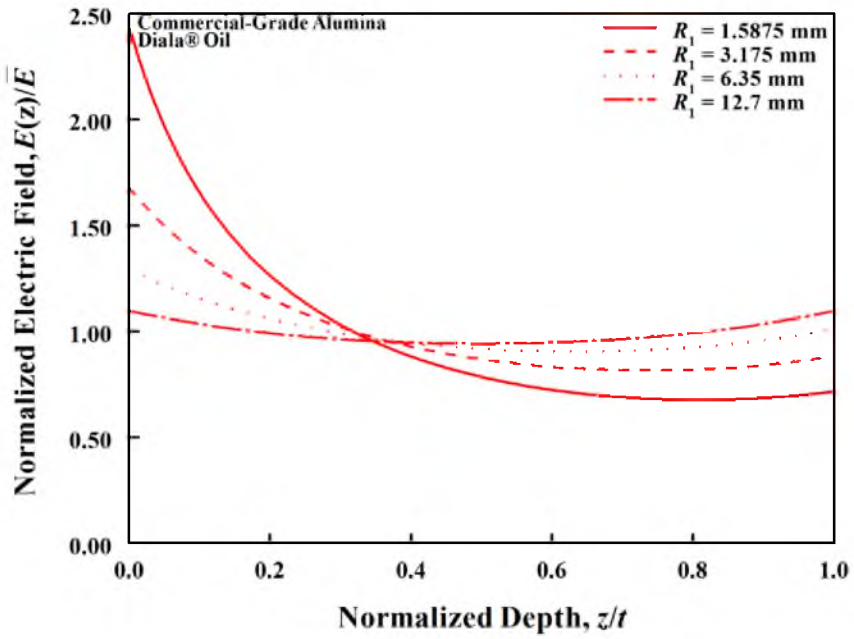

Figure 3.20 Normalized electric field plotted as a function of normalized depth at the center of a specimen for different ball electrode radii.

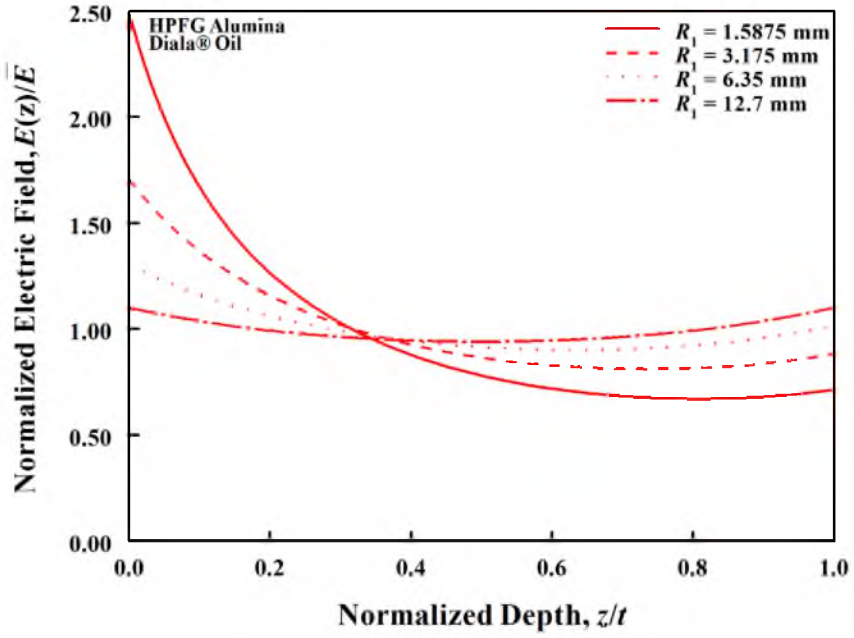

Figure 3.21 Normalized electric field plotted as a function of normalized depth at the center of a specimen for different ball electrode radii.

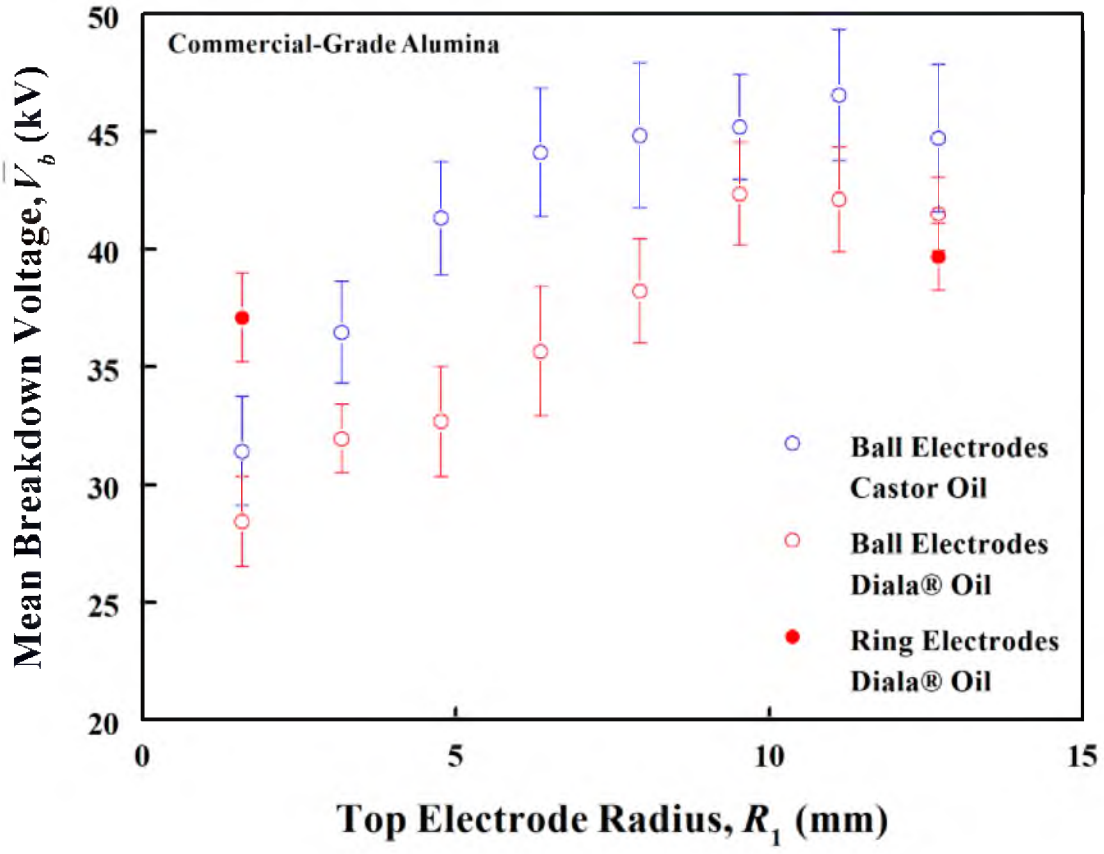

Figure 3.22 Means and standard errors of the measured breakdown voltages plotted as functions of top electrode radius.

$$E_{\max}^{b} = \frac{E(r=0)}{\overline{E}} \frac{V_b}{t} \tag{3.1}$$

In Equation (3.1), $E(r=0)/\overline{E}$ is the maximum field intensification factor obtained by FEA, V_b is the breakdown voltage, and t is the specimen thickness at the breakdown site.

Figure 3.23 shows plots of the means and standard errors of the breakdown electric field, E^{b}_{max}, as a function of the top electrode radius for the ball and the ring electrodes. The breakdown electric field increased with decreasing electrode radius. The breakdown electric fields were higher in the Diala® oil than in the castor oil. The relative change in the breakdown field with electrode radius was again greater for the ball electrodes than the ring electrodes.

Figure 3.24 shows plots of the mean breakdown voltage, $\overline{V_b}$, as a function of specimen thickness for test series C. The mean breakdown voltage increased with increasing specimen thickness. This increase was, however, nonlinear with a greater sensitivity at small thickness. Figure 3.25 shows plots of E^{b}_{max} as a function of specimen thickness. The breakdown electric field increased with decreasing specimen thickness. This increase was most pronounced in the reduction of thickness from 0.5 to 0.25 mm.

Figure 3.26 compares plots of the breakdown voltage as a function of top ball electrode radius for the two grades of alumina in test series D. The mean breakdown voltage increased with increasing top electrode radius. The mean breakdown voltages were consistently higher for the HPFG alumina than for the commercial-grade alumina, but the difference was small.

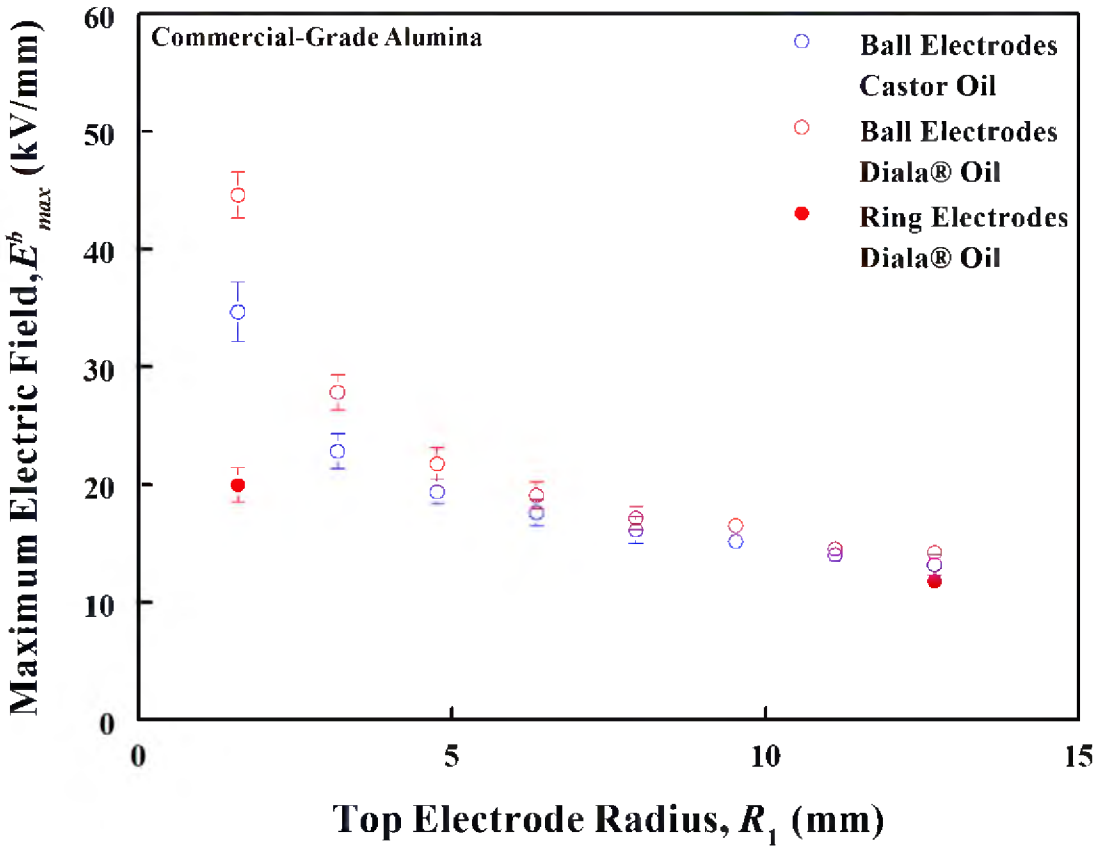

Figure 3.23 Means and standard errors of the breakdown electric fields plotted as functions of the top electrode radius.

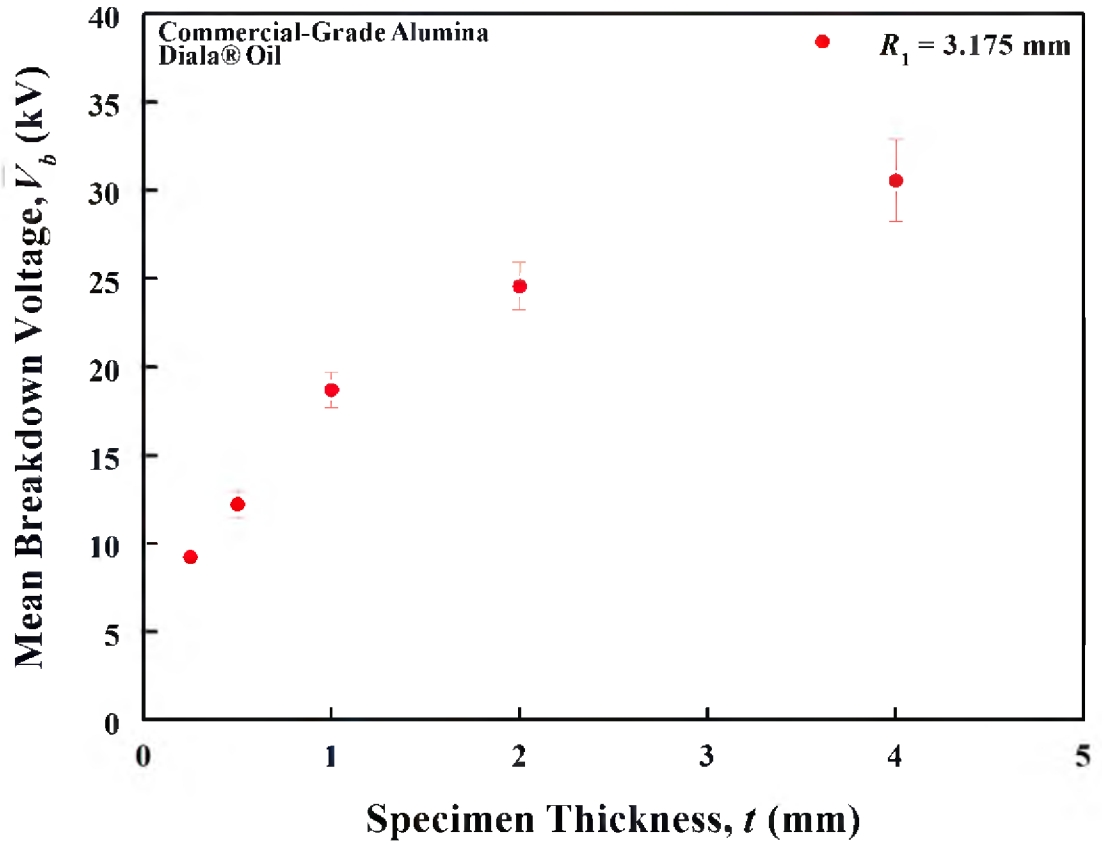

Figure 3.24 Means and standard errors of the measured breakdown voltages plotted as functions of specimen thickness.

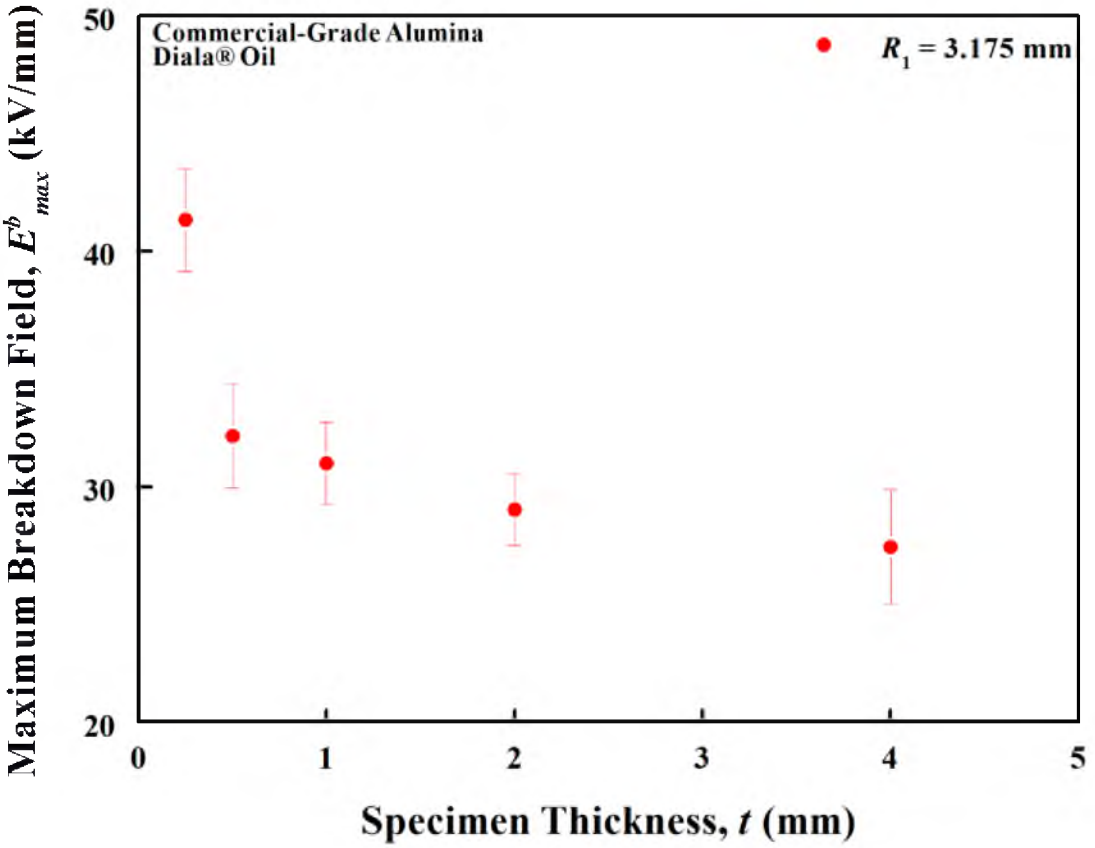

Figure 3.25 Means and standard errors of the breakdown electric fields plotted as functions of specimen thickness.

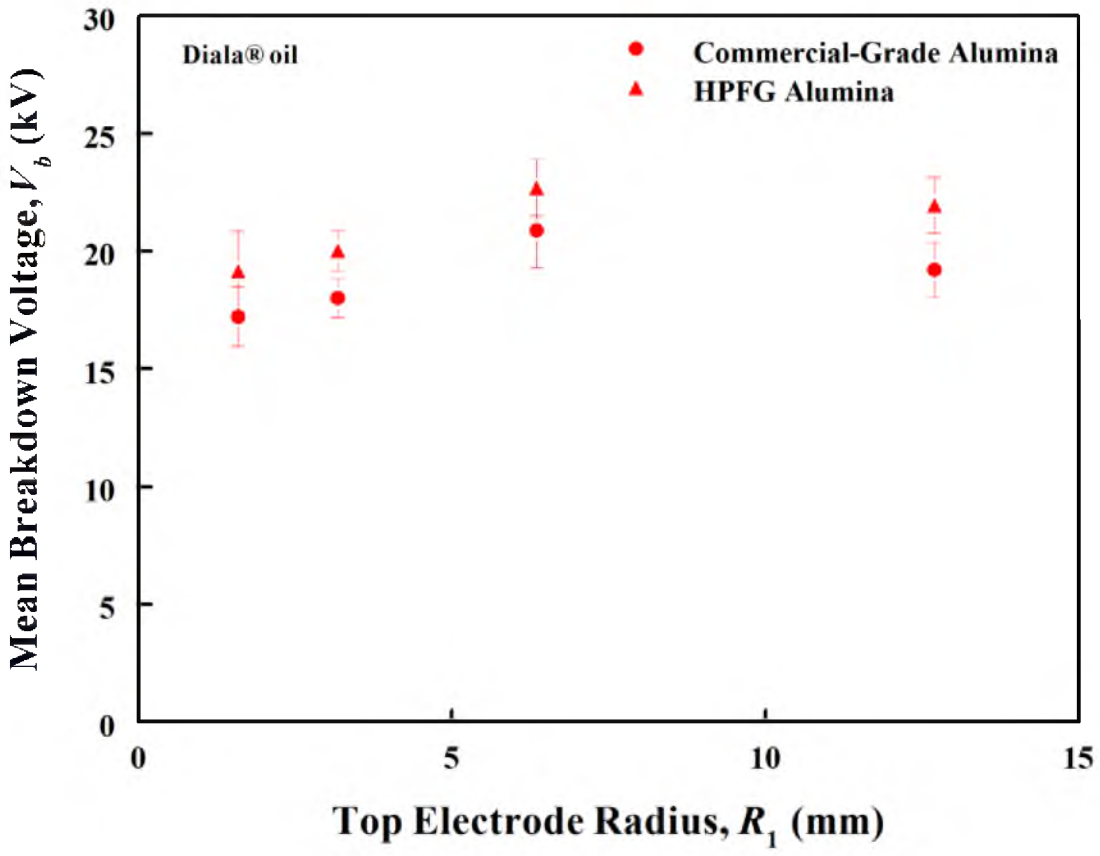

Figure 3.26 Means and standard errors of the measured breakdown voltages plotted as functions of top electrode radius.

Figure 3.27 shows plots of E^{b}_{max} as a function of top electrode radius for the two grades of alumina. The breakdown electric field decreased with increasing electrode radius for both aluminas. The values were higher for the HPFG alumina than for the commercial-grade alumina.

3.4 Failure Location Distribution

Figures 3.28 and 3.29 show the radial distribution of the breakdown failure locations for tests conducted using ball electrodes (R_1 = 1.5875 mm, 12.7 mm R_2 = 12.7 mm) in Diala® oil. The highest fraction of breakdowns occurred in the radial interval, 1 – 2 mm and 2 – 3 mm for a top electrode radius of R_1 = 1.5875 mm and R_1 = 12.7 mm, respectively. It is important to note that the most probable breakdown location does not occur at the electrode contact point. This is due to the fact that the radial breakdown location is a function of both the local electric field and the area element at the radial distance (dA = 2πdr). The area element increases with r shifting the most probable breakdown location away from the contact point.

Figures 3.30 and 3.31 show the radial distribution of breakdown failure locations for tests conducted using ring electrodes in Diala® oil. The highest fraction of breakdowns occurred in the radial interval, 20 – 21 mm and 21 – 22 mm for R_c = 1.5875 and R_c = 12.7 mm, respectively. Although the electric field distributions are the same on both sides of the contact point, a higher fraction of breakdowns occur at radial positions greater than the position of the contact point (19.05 mm). This further illustrates that the breakdown location is a function of both the local electric field and the area element at the radial distance.

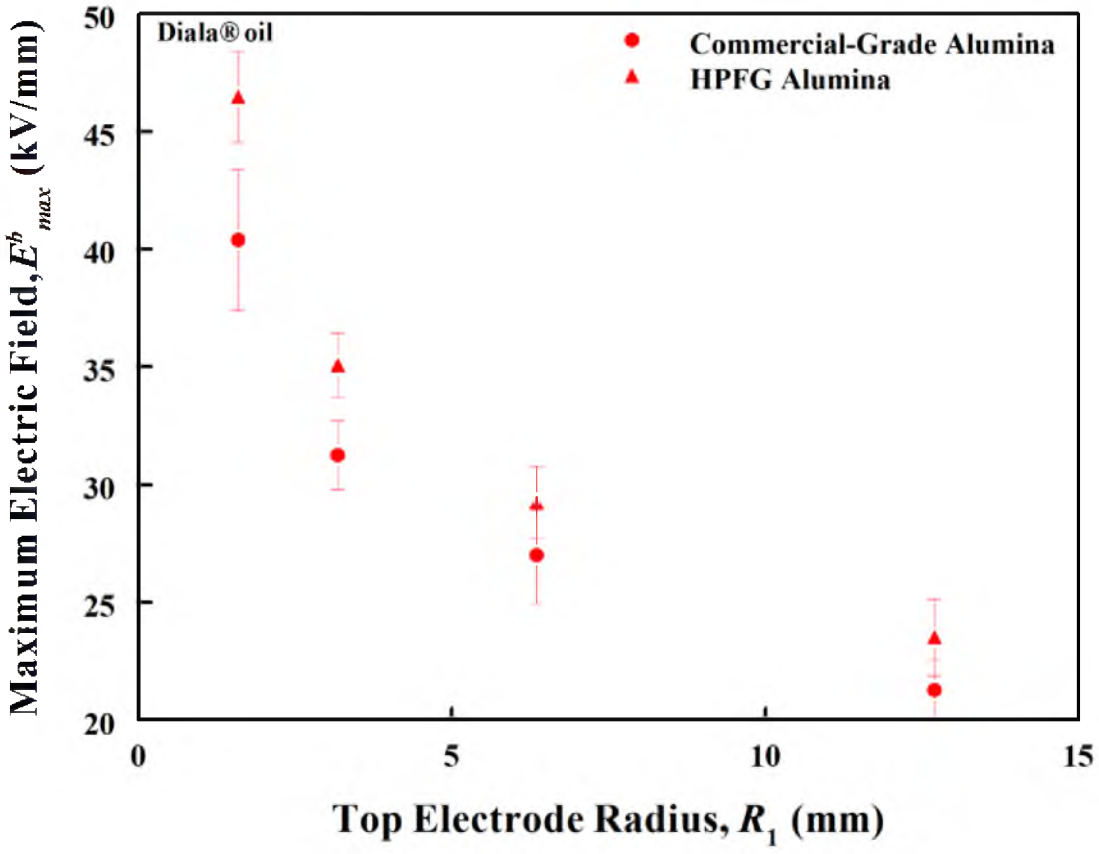

Figure 3.27 Means and standard errors of the breakdown electric fields plotted as functions of top electrode radius.

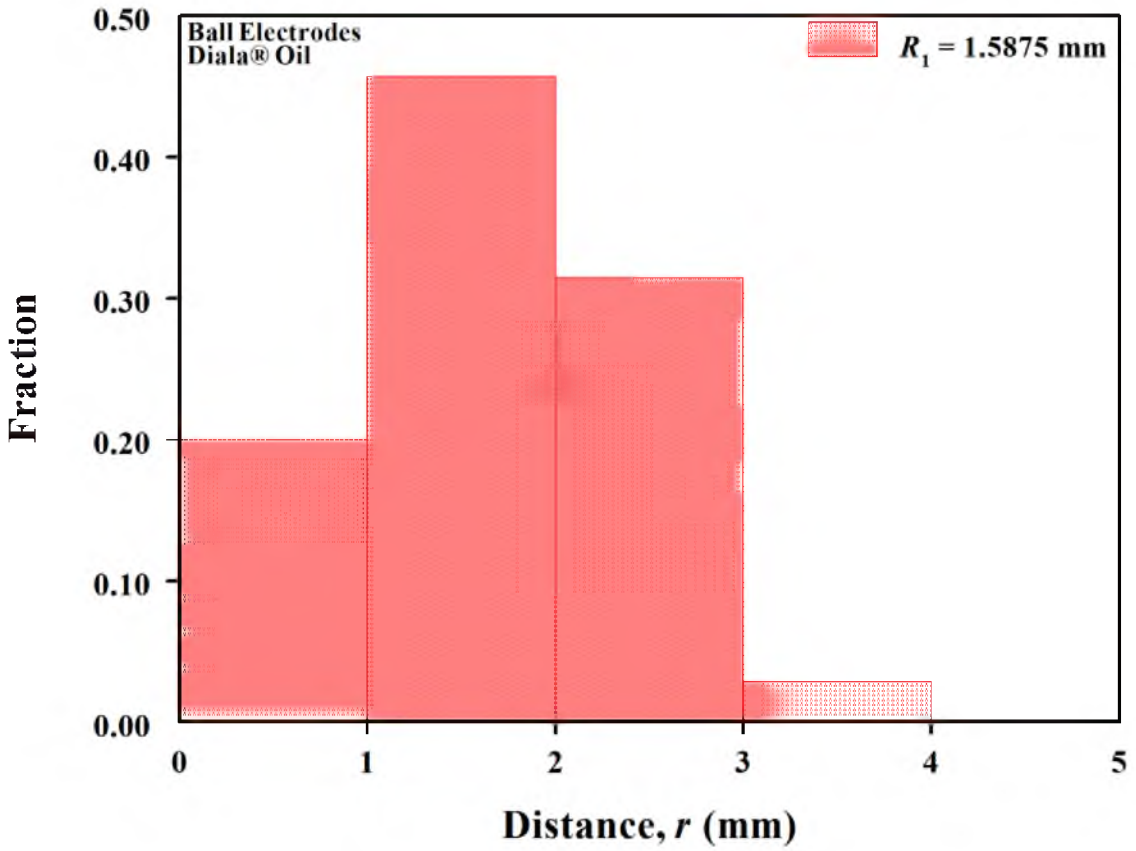

Figure 3.28 Histogram of the fraction of breakdown locations versus the radial position obtained using ball electrodes (R_1 = 1.5875 mm) in Daila® oil.

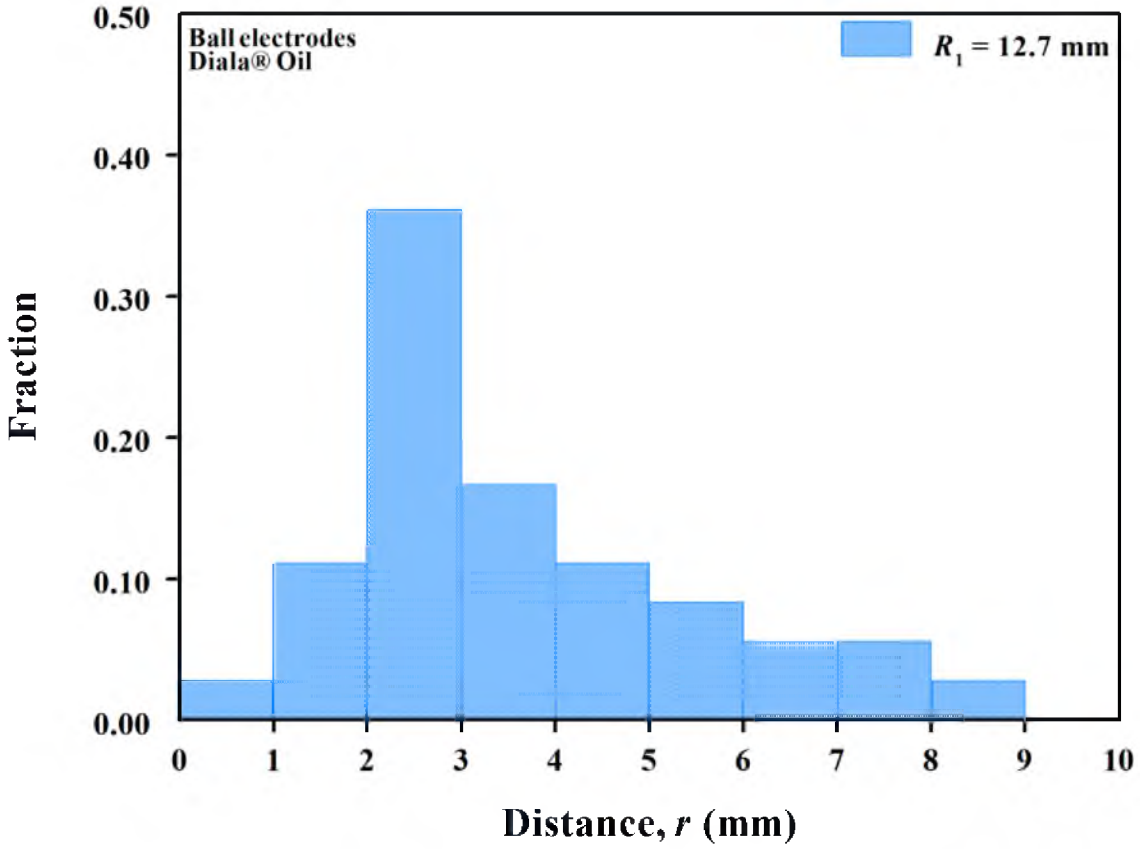

Figure 3.29 Histogram of the fraction of breakdown locations versus the radial position obtained using ball electrodes (R_1 = 12.7 mm) in Daila® oil.

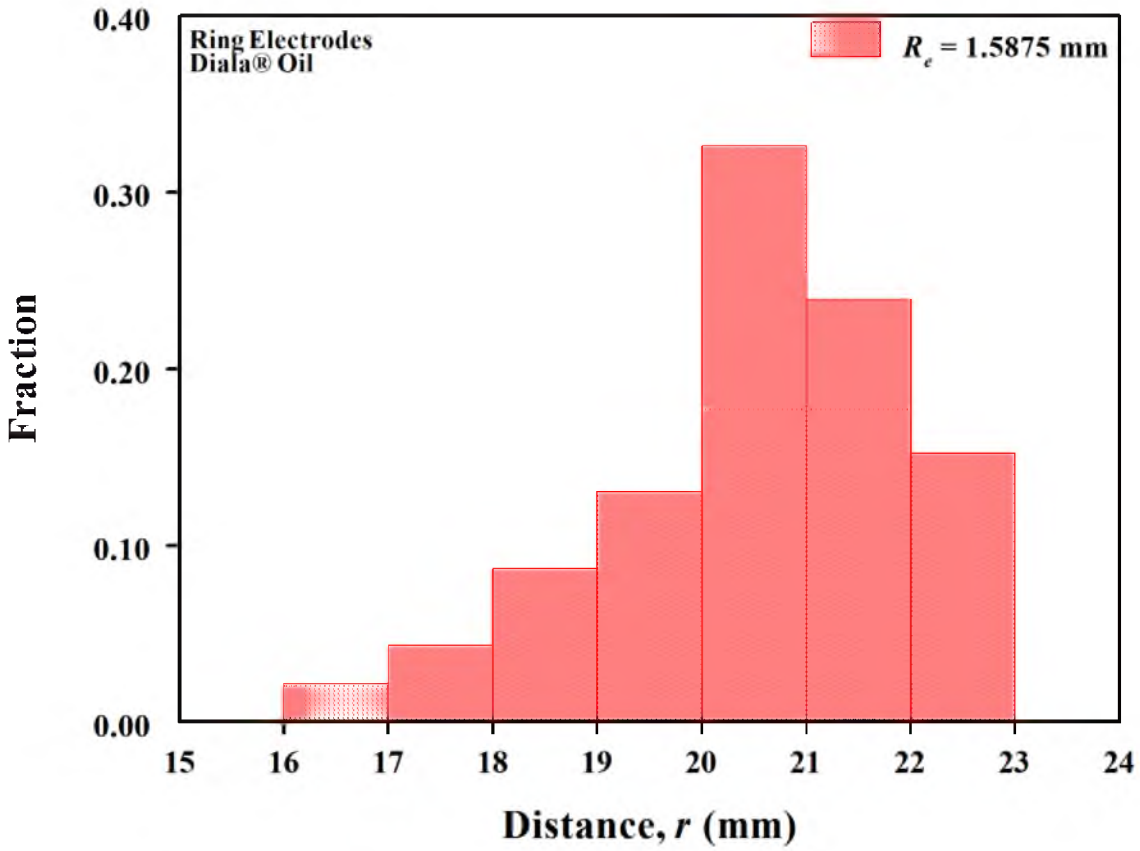

Figure 3.30 Histogram of the fraction of breakdown locations versus the radial position obtained using ring electrodes (R_1 = 1.5875 mm) in Daila® oil.

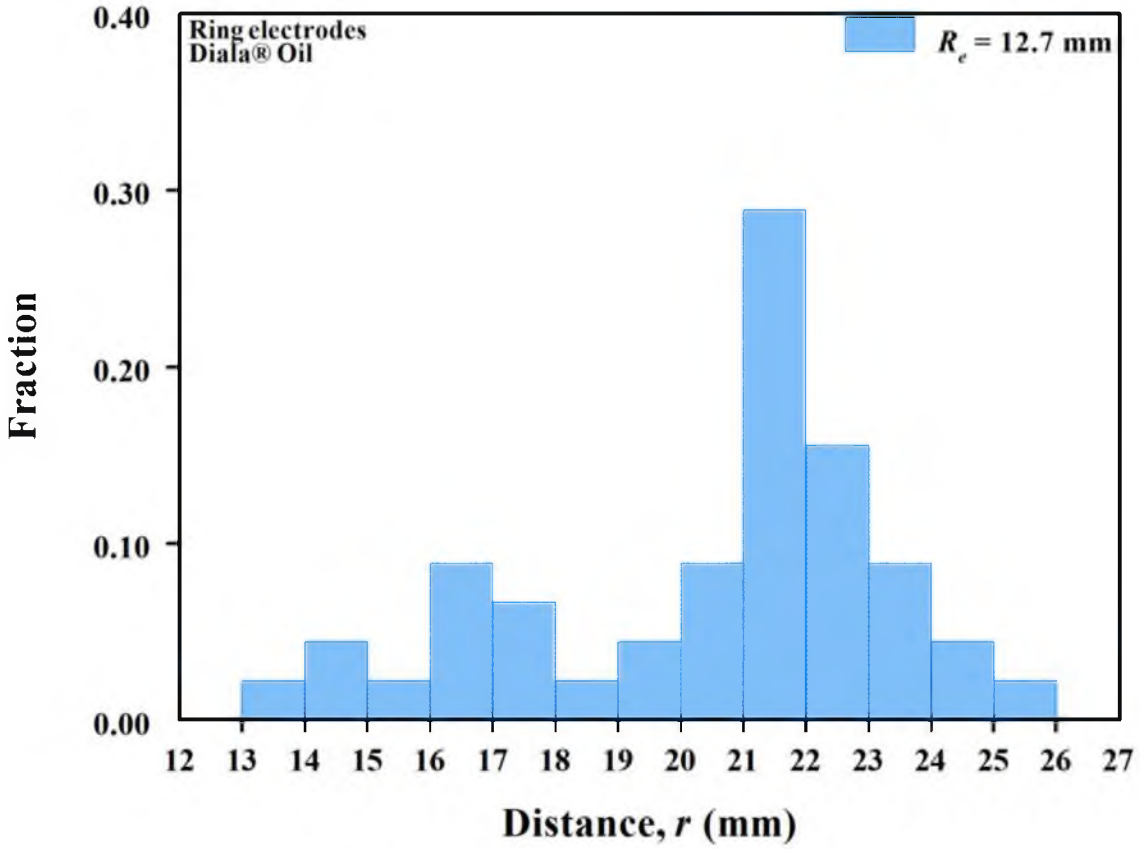

Figure 3.31 Histogram of the fraction of breakdown locations versus the radial position obtained using ring electrodes (R_1 = 12.7 mm) in Daila® oil.

CHAPTER 4

ANALYSES OF BREAKDOWN STRENGTHS AND DISCUSSION

4.1 Weakest-Link Failure Analysis

The results of this study show a systematic increase in the breakdown strength of alumina with the spatial localization of the electric field in the test specimen. The electric field can be spatially localized by decreasing the electrode radius, specimen thickness, and the dielectric constant of the dielectric liquid. This indicates a scaling of the breakdown strength with the electrically stressed specimen volume or surface area. Such a scaling suggests that the dielectric breakdown of alumina may be described as a weakest-link failure phenomenon analogous to brittle fracture[21,22]. Weakest-link failure theory has been used in the past to rationalize the variations of dielectric breakdown field with electrode radius and/or shape in paper capacitors[51], casting resins[52], epoxy resin[53], metal-oxide films[54], transformer oil[55], and liquid nitrogen[39, 40].

In the weakest-link failure description, dielectric breakdown initiates at defects that enhance the local electric field. A consequence of this defect-controlled breakdown is that the ceramic does not exhibit a unique breakdown electric field. The measured breakdown field is determined by the most severe defect (the weakest link) in the stressed volume or area. The theoretical basis of weakest-link failure is the theory of extreme values, or more specifically, the mathematical relation between a population distribution and the

distribution of lowest values in samples of size n drawn from the population. We define the population density distribution of the breakdown field in a ceramic as $f(E)$ and the corresponding cumulative distribution as $F(E)$. The distribution of the lowest value in samples of size n drawn from the population is given by the probability density function[22]:

$$g_n(E) = nf(E)[1 - F(E)]^{n-1} \tag{4.1}$$

The corresponding cumulative distribution of the lowest value in samples of size n is given by the following equation:

$$G_n(E) = 1 - [1 - F(E)]^n \tag{4.2}$$

Equations (4.1) and (4.2) are valid for any population distribution and sample size. When the sample size, n is large, the following asymptotic forms of Equations (4.1) and (4.2) are valid:

$$g_n(E) = nf(E)\exp[-nF(E)] \tag{4.3}$$

$$G_n(E) = 1 - \exp[-nF(E)] \tag{4.4}$$

In general, it is difficult, if not impossible, to identify and characterize the defects that determine the breakdown fields in a ceramic. Epstein and Brooks[51] were successful in correlating breakdown fields in paper capacitors with the size distribution of the largest metal particles in the paper-capacitors. Chao and Shetty[56] correlated fracture strength

distributions of a sintered silicon nitride with the distributions of the largest pore in the test specimens. Even if the defects cannot be sufficiently characterized, it is still possible to determine the population distribution which correctly scales the breakdown field with stressed volume or surface area. To illustrate this, we first define the most probable breakdown field, E_n^*, for a sample containing n defects:

$$\frac{dg_n}{dE}\left(E_n^*\right) = 0 \tag{4.5}$$

This definition leads to specific scaling relations between E_n^* and n and for different population distributions $f(E)$. In this study, Laplace and Weibull distributions were considered for the population. The dependence of E_n^* on sample size n is different for different population distributions.

Scaling relations between E_n^* and n are useful only if n can be directly measured or calculated. An additional complicating factor is the non-uniform distribution of the electric fields in the test specimens. Defects in different spatial locations in the specimens experience different electrical fields. To circumvent these problems, we make two assumptions. First, the defects responsible for breakdown are distributed uniformly in the specimen surface area (concentration, ρ_A) and volume (concentration, ρ_V). Second, we assume that the measured breakdown fields correspond to either the defects in the volume or on the surface, but not a mixture of the two. First, consider area-distributed defects in a ceramic. The effective number of defects, n_{eff}, sampled in a test specimen with non-uniform distribution of electric field is defined as:

$$n = n_{eff} = \rho_A A_{eff} \tag{4.6}$$

In Equation (4.6), A_{eff} is an effective stressed area of a hypothetical specimen with a uniform electric field E_{max} that has the same cumulative probability of breakdown as a specimen with non-uniform electric field in an area, A. This equality of cumulative breakdown probabilities of the two specimens can be mathematically represented by the following equation for A_{eff}.

$$A_{eff} = \frac{1}{F(E_{\max})} \int_0^A F(E) dA \tag{4.7}$$

The area and the volume integrals were calculated for each test setup by numerical integration of the FEA results using Simpson's Rule[57]. The numerical integration algorithm took advantage of the axial symmetry of the electric field distribution and considered a large number of slices of the specimen in the axial direction:

$$A_{eff}(z_i) = 2\pi \int_{r=0}^{R} \left[\frac{F(E(r, z_i))}{F(E_{\max})} \right] r dr \tag{4.8}$$

In Equation (4.8), R is the radius of the specimen, $E(r,z_i)$ is the electric field at the radial distance r and a depth of z_i, and E_{max} is the maximum electric field in the specimen. The effective stressed area is calculated by solving Equation (4.8) for the top ($z_i = 0$) and the bottom ($z_i = t$) surfaces.

Alternatively, the breakdown controlling defects can be assumed to be volume defects rather than surface defects. Then, the effective number of defects sampled in a test is related to the volume density of the defects (ρ_V) and an effective stressed volume of the specimen, V_{eff}:

$$n = n_{eff} = \rho_V V_{eff} \tag{4.9}$$

V_{eff} was calculated using the following formula:

$$V_{eff} = \sum_{i=1}^{p} A_{eff}(z_i)\delta z_i \tag{4.10}$$

In Equation (4.10), $A_{eff}(z_i)$ is the effective stressed area on a plane at a depth z_i, δz_i is the thickness of a slice at a depth z_i, and p is the total number of slices through the thickness.

4.2 Most Probable Breakdown Field

In order to select the appropriate population distribution and the scaling relation for breakdown fields, the most probable breakdown field, E_n^*, must be assessed for each test setup. This was done by plotting the maximum breakdown field, E^b_{max}, for each test on a histogram. Figure 4.1 shows an example of such a histogram for breakdown fields of commercial-grade alumina tested with ball electrodes (R_1 = 3.175 mm, R_2 = 12.7 mm) in castor oil. A bin size of 1 kV/mm was used for all the tests. The midpoint value of the bin with the highest fraction was defined as E_n^* for that test setup. If two adjacent bins had the same maximum fraction, the value of E_n^* was defined as the average of the midpoints.

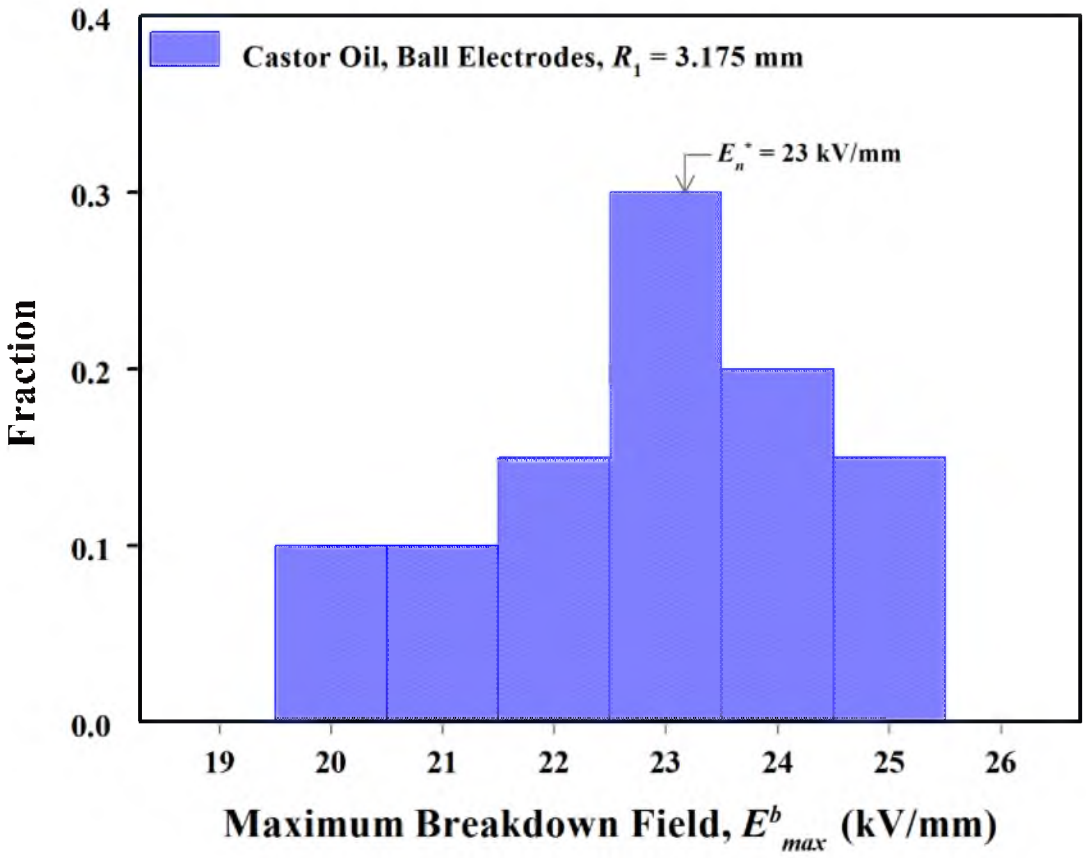

Figure 4.1 A histogram of breakdown fields for commercial-grade alumina measured using ball electrodes (R_1 = 3.175 mm, R_2 = 12.7 mm) in castor oil.

The most probable breakdown field, E_n^*, exhibited the same dependences on test variables as the mean breakdown field. E_n^* increased with decreasing electrode radius for both dielectric liquids. The values were higher in Diala® oil than in castor oil. E_n^* increased with decreasing specimen thickness. The values were higher for the HPFG alumina than for the commercial-grade alumina.

4.3 Analysis of the Scaling of En*

As discussed in Section 4.1, the scaling of E_n^* with effective stressed volume, V_{eff}, or the effective stressed area, A_{eff}, is key to identifying the underlying population distribution of breakdown fields. The scaling of E_n^* with V_{eff} (or A_{eff}) is compared with the theoretical scaling relations obtained from Equation (4.5) for different population distributions.

The population distribution that gives the best agreement with the measured scaling and the various test distributions is selected as the most appropriate. In this study, we selected the Weibull and the Laplace distributions for the population because they lead to relatively simple scaling relations from which the population distribution parameters and defect densities can be extracted. Since it is not known *a priori* if defects distributed in the volume or on the surface cause dielectric breakdown, scaling of E_n^* will be analyzed with respect to both effective stressed volume and effective stressed area for both the Weibull and the Laplace distributions. The results of defect characterization presented in Sections 4.4 and 4.5 will provide insight on the nature and distribution of the breakdown-controlling defects.

4.3.1 Weibull (Population) Distribution

The Weibull population density distribution, $f(E)$, and the corresponding cumulative distribution, $F(E)$, are defined by the following equations:

$$f(E) = m\frac{E^{m-1}}{E_0{}^m}\exp\left[-\left(\frac{E}{E_0}\right)^m\right] \tag{4.11}$$

$$F(E) = 1-\exp\left[-\left(\frac{E}{E_0}\right)^m\right] \tag{4.12}$$

In Equations (4.11) and (4.12), m is the shape parameter of the Weibull distribution and E_0 is the scale parameter. The most probable breakdown field, E_n^*, as a function of the effective stressed area, A_{eff}, i.e., the scaling relation for the Weibull population distribution, is obtained from Equation (4.5) as follows (see Appendix C for derivation):

$$\log_{10}\left(E_n^*\right) = \log_{10}\left(E_0\frac{\left(1-\frac{1}{m}\right)^{\frac{1}{m}}}{\left(\rho_A\right)^{\frac{1}{m}}}\right) - \frac{1}{m}\log_{10}\left(A_{eff}\right) \tag{4.13}$$

It should be noted that the scaling relation contains three unknown parameters: the two population distribution parameters, m and E_0, and the surface concentration of the defects, ρ_A. A_{eff} was calculated for each test series using the following equation:

$$A_{eff} = 2\pi \int_{r=0}^{R} \left[\frac{E(r, z_i)}{E_{\max}} \right]^m r dr \tag{4.14}$$

This calculation used an initial estimated value for the shape parameter m. Then, $\log_{10} En^*$ was plotted versus $\log_{10} A_{\text{eff}}$ to test the scaling relationship of Equation (4.13). The slope of this plot is equal to $-\frac{1}{m}$. The value of m so obtained was used to recalculate A_{eff} and replot $\log_{10} E_n^*$ versus $\log_{10} A_{eff}$ until successive iterations gave the same value of m to the third decimal place. After seventeen iterations, an m value of 5.5 was obtained. Figure 4.2 shows the plot of $\log_{10} E_n^*$ versus $\log A_{eff}$ corresponding to m = 5.5. The intercept of the plot in Figure 4.2 is equal to $\log_{10} E_0 + \frac{1}{m}\log_{10}\left(1 - \frac{1}{m}\right) - \frac{1}{m}\log_{10} \rho_A$. Therefore, two parameters, E_0 and ρ_A, had to be determined from the intercept. The following procedure was used for estimating E_0 and ρ_A. An initial value for E_0 was assumed, typically greater than the highest value of breakdown field measured in all the tests. The corresponding value of ρ_A was calculated from the intercept. The three material parameters so obtained, m, E_0 and ρ_A, were used to calculate the cumulative distributions of breakdown fields for the various test setups, $G_n(E_{\max})$, using Equation (4.4) and Equation (4.6). A goodness-of-fit was assessed by calculating the coefficient of determination (R^2) for each test setup. The value of E_0 was increased incrementally to calculate a new value of ρ_V and a new set of R^2 values. The combination of parameters, E_0 and ρ_V, along with the value of m from the slope of Figure 4.2 that gave the highest R^2 value was taken as the "best-fit" Weibull parameters of the material. This procedure yielded m = 5.5, E_0 = 105.1 KV/mm, and ρ_A = 1718 defects/mm^2. Figure 4.3 shows the experimental data and the cumulative distribution plots

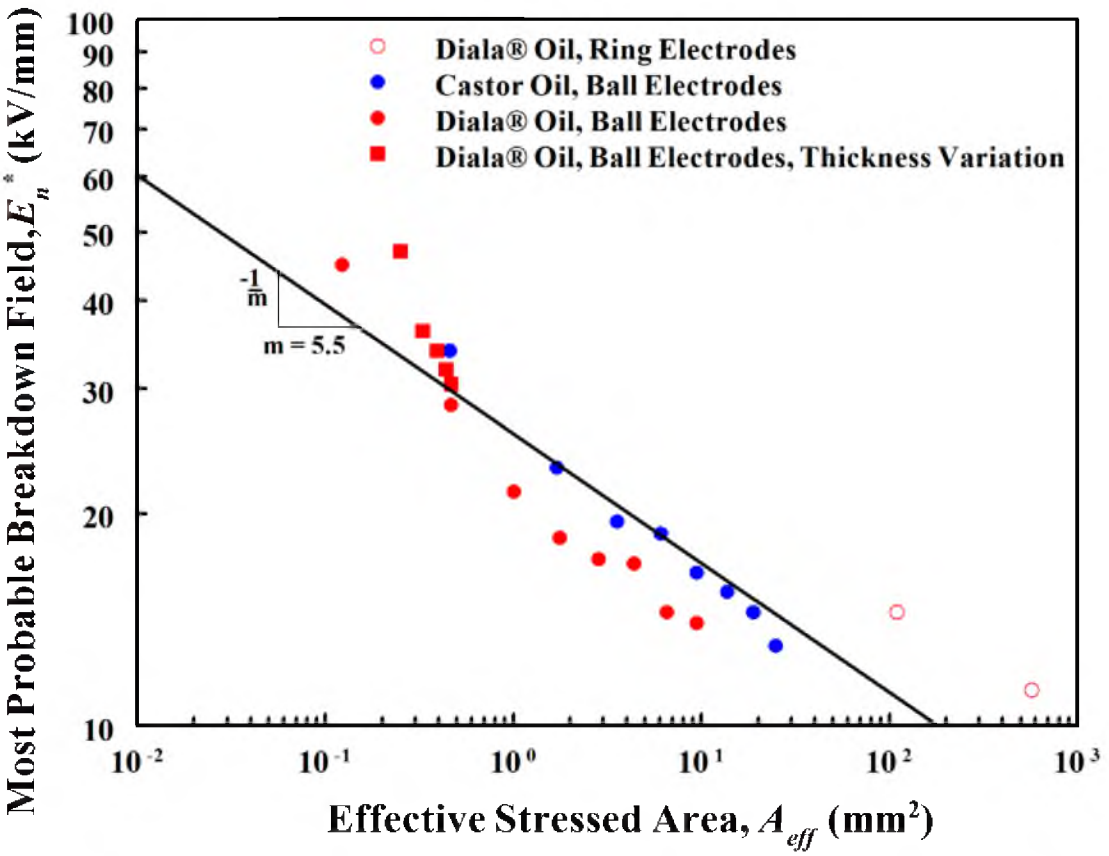

Figure 4.2 Scaling of the most probable breakdown field, E_n^*, with effective stressed surface area defined for the Weibull population distribution.

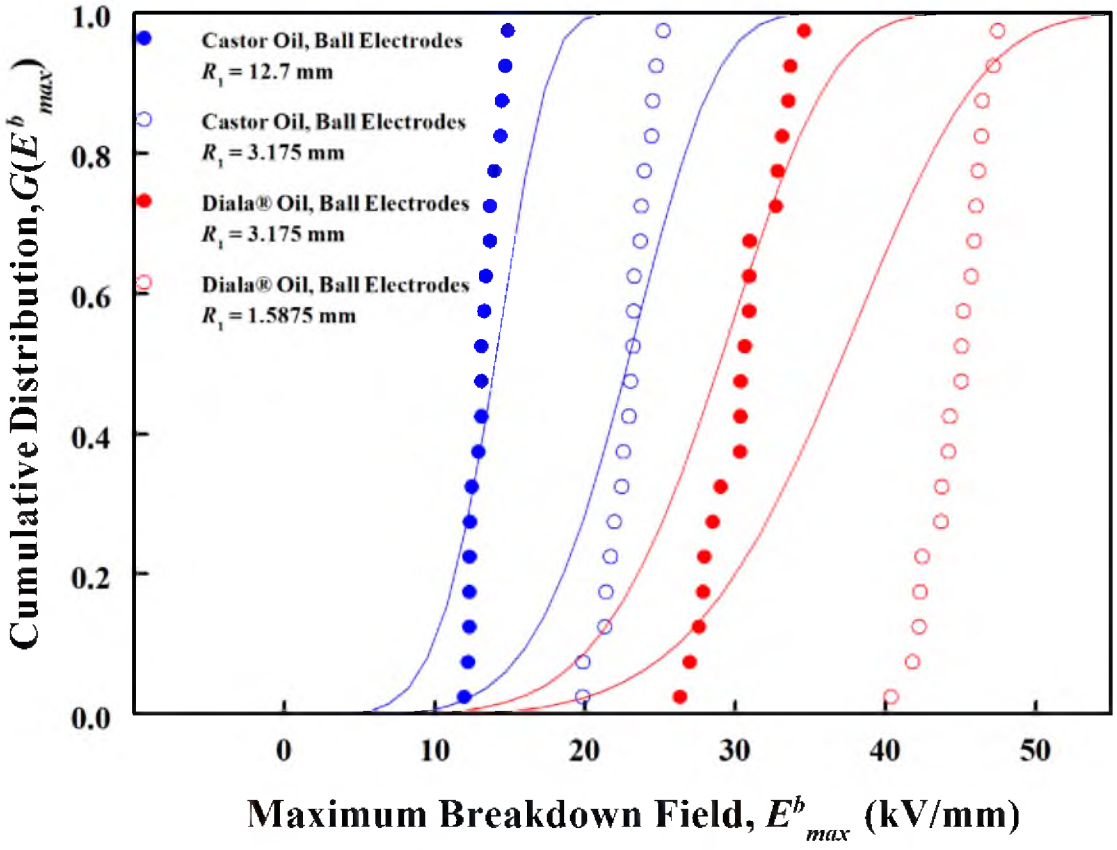

Figure 4.3 Cumulative distribution plots of the breakdown fields measured in four test series compared with extreme-value distributions based on the Weibull (population) distribution with parameters, m = 5.5, E_0 = 105.1 KV/mm, and $\boldsymbol{\rho_A = 1718\ \frac{defects}{mm^2}}$.

for four representative test setups. The cumulative distribution plots were obtained using the following equation:

$$G_n(E) = 1 - \exp\left[-n\left(1 - \exp\left[-\left(\frac{E}{E_0}\right)^m\right]\right)\right] \tag{4.15}$$

It is clear from Figures 4.2 and 4.3 that the Weibull distribution provides a poor fit for the data. First, the Weibull shape parameter obtained from the scaling relation of Figure 4.2 does not give good fits to the cumulative distribution plots in Figure 4.3, particularly for small sample sizes or low values of A_{eff}. The experimentally obtained breakdown field distributions are much narrower than the corresponding distributions predicted from the Weibull population distribution. Second, the breakdown fields measured with specimens of varying thickness did not follow the Weibull scaling relation in Figure 4.2. Finally, the goodness-of-fit of the scaling relation in Figure 4.2 was modest ($R^2 = 0.85$).

A similar analysis was carried out using the Weibull distribution for the population and assuming the defects to be distributed in the volume, i.e., by correlating the most probable breakdown field, En* with an effective stressed volume, Veff. The most probable breakdown field, En*, as a function of the effective stressed area, Aeff, i.e., the scaling relation for the Weibull population distribution, is obtained from Equation (4.5) as follows (see Appendix C for derivation):

$$\log_{10}\left(E_n^*\right) = \log_{10}\left[E_0 \frac{\left(1-\frac{1}{m}\right)^{\frac{1}{m}}}{\left(\rho_V\right)^{\frac{1}{m}}} \right] - \frac{1}{m}\log_{10}\left(V_{eff}\right) \tag{4.16}$$

It should be noted that the scaling relation contains three unknown parameters: the two population distribution parameters, m and E_0, and the volume concentration of the defects, ρ_V. V_{eff} was calculated for each test series using the following equation:

$$V_{eff} = 2\pi \int_{z=0}^{t} \int_{r=0}^{R} \left[\frac{E(r,z_i)}{E_{max}} \right]^m r dr dz \tag{4.17}$$

The scaling relation and cumulative distribution plots obtained from the optimum Weibull parameters, m = 7.2, E_0 = 102.6 kV/mm, and ρ_A = 1.79 * 10^5 defects/mm^3, are shown in Figure 4.4 and Figure 4.5, respectively. It is again clear from these figures that the Weibull distribution is not a good choice for the population distribution of breakdown fields of the alumina ceramic for scaling with V_{eff}. First, the Weibull shape parameter obtained from the scaling relation of Figure 4.4 does not give good fits to the cumulative distribution plots in Figure 4.5, particularly for small sample sizes or low values of V_{eff}. The experimentally obtained breakdown field distributions are much narrower than the corresponding distributions predicted from the Weibull population distribution. Second, the breakdown fields measured with specimens of varying thickness did not follow the Weibull scaling relation in Figure 4.4. Finally, the goodness-of-fit of the scaling relation in Figure 4.4 was modest (R^2 = 0.88). The Weibull distribution is not a good choice whether the defects are assumed to be distributed on the surface or in the volume.

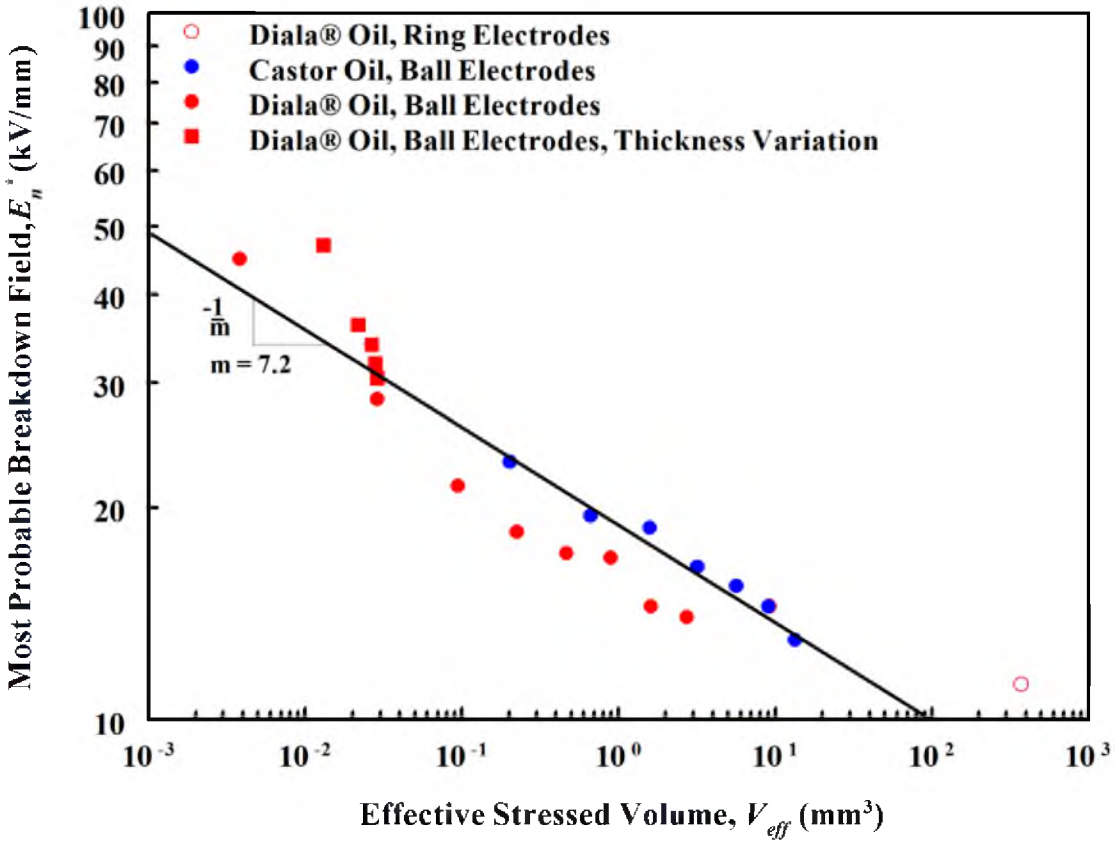

Figure 4.4 Scaling of the most probable breakdown field, E_n^*, with effective stressed volume defined for the Weibull population distribution.

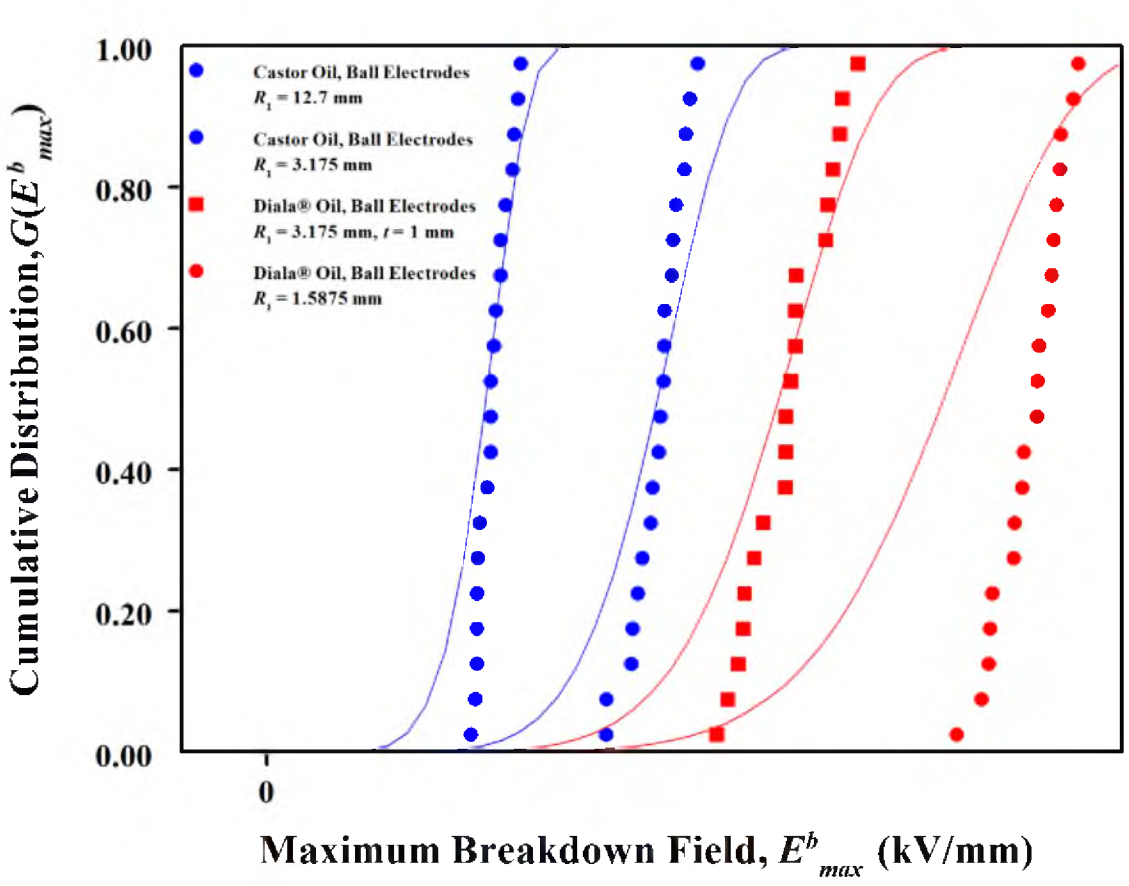

Figure 4.5 Cumulative distribution plots of the breakdown fields measured in four test series compared with extreme-value distributions based on the Weibull (population) distribution with parameters, m = 7.2, E_0 = 102.6 KV/mm, and $\boldsymbol{\rho_V = 1.79 * 10^5 \frac{defects}{mm^3}}$.

4.3.2 Laplace (Population) Distribution

The Laplace population density distribution, $f(E)$, and the corresponding cumulative distribution, F(E), are defined by the following equations:

$$f(E) = \frac{1}{2\lambda} \exp\left[\frac{E-\mu}{\lambda}\right] \tag{4.18}$$

$$F(E) = \frac{1}{2} \exp\left[\frac{E-\mu}{\lambda}\right] \tag{4.19}$$

In Equations (4.17) and (4.18), μ is the location parameter and λ is the scale parameter.

A similar analysis, to what was done for the Weibull distribution, was carried out using the Laplace distribution for the population and assuming the defects to be distributed on the surface, i.e., by correlating the most probable breakdown field, E_n^* with an effective stressed area, A_{eff}. The most probable breakdown field, E_n^*, as a function of the effective stressed area, A_{eff}, i.e., the scaling relation for the Laplace distribution, is obtained from Equation (4.5) as follows (see Appendix D for derivation):

$$E_n^* = \mu - \lambda \log_e\left(\frac{\rho A_{eff}}{2}\right) \tag{4.20}$$

It should be noted that the scaling relation again contains three unknown parameters: the two population distribution parameters, μ and λ, and the surface concentration of defects, ρ_A. A_{eff} was calculated for each test series using the following equation:

$$A_{eff} = 2\pi \int_{r=0}^{R} \left[\exp\left[\frac{\mathrm{E}(\mathrm{r}, \mathrm{z}_i) - E_{\max}}{\lambda} \right] \right] r dr \tag{4.21}$$

The scaling relation and the cumulative distribution plots obtained from the optimum Laplace parameters, λ = 3.2 kV/mm, μ = 44.77 kV/mm, and ρ_A = 1998 defects/mm^2, are shown in Figure 4.6 and Figure 4.7, respectively. The cumulative distribution plots were obtained using the following equation:

$$G_n(E) = 1 - \exp\left[-n\left(\frac{1}{2} \exp\left[\left(\frac{E-\mu}{\lambda} \right) \right] \right) \right] \tag{4.22}$$

The Laplace population distribution represents the scaling (R^2 = 0.91 for Figure 4.6) and the cumulative distributions more accurately than the Weibull distribution. In particular, the shapes of the cumulative distributions are better described by the Laplace distribution function. The breakdown fields measured with specimens of varying thickness are also in line with the scaling relation. The dashed lines in Figure 4.7 represent the 90% confidence bands of the cumulative probabilities of breakdown for the ball electrode tests (R_1 = 12.7 mm) and the tests with 0.5 mm thick disks. The dashed lines in Figure 4.6 also represent the 90% confidences bands of the most probable breakdown field. The Laplace distribution is a good choice whether the defects are assumed to be distributed in the volume or on the surface.

A similar analysis was also carried out using the Laplace distribution for the population and assuming the defects to be distributed in the volume, i.e., by correlating the most probable breakdown field, E_n^* with an effective stressed volume, V_{eff}. The most

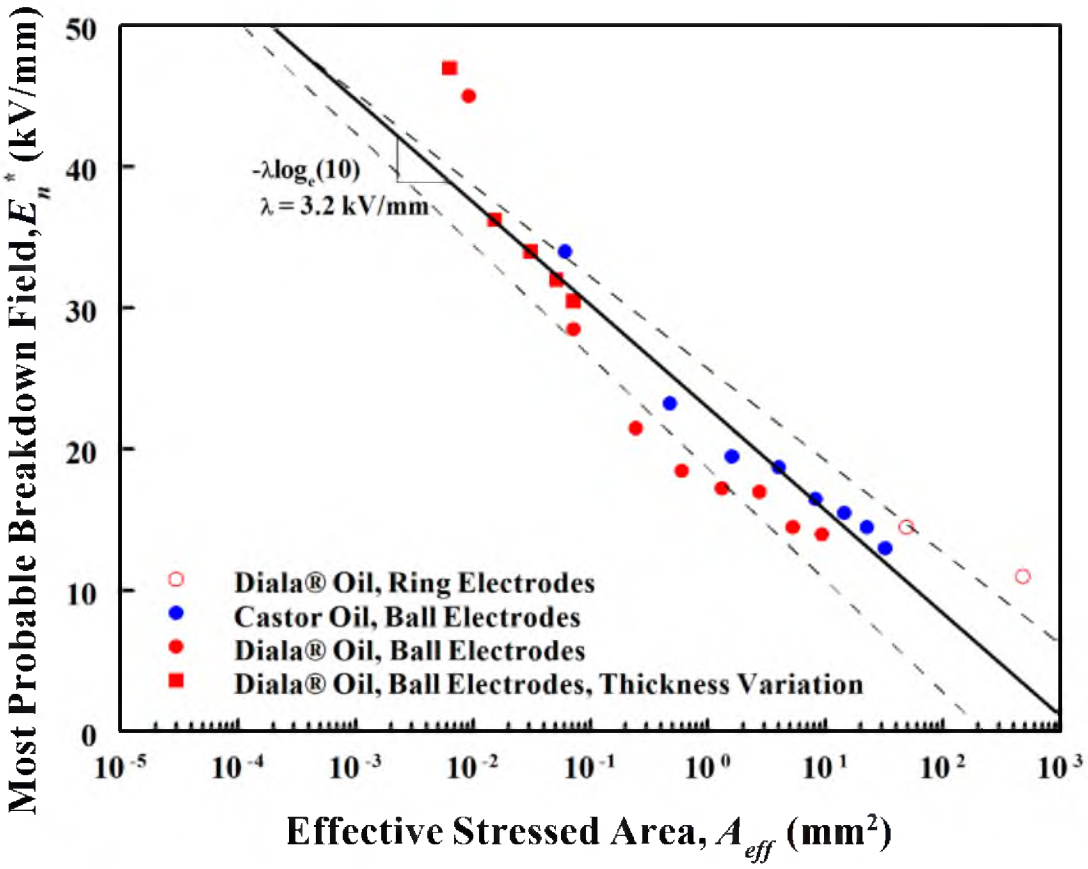

Figure 4.6 Scaling of the most probable breakdown field, E_n^*, with effective stressed area defined for the Laplace population distribution.

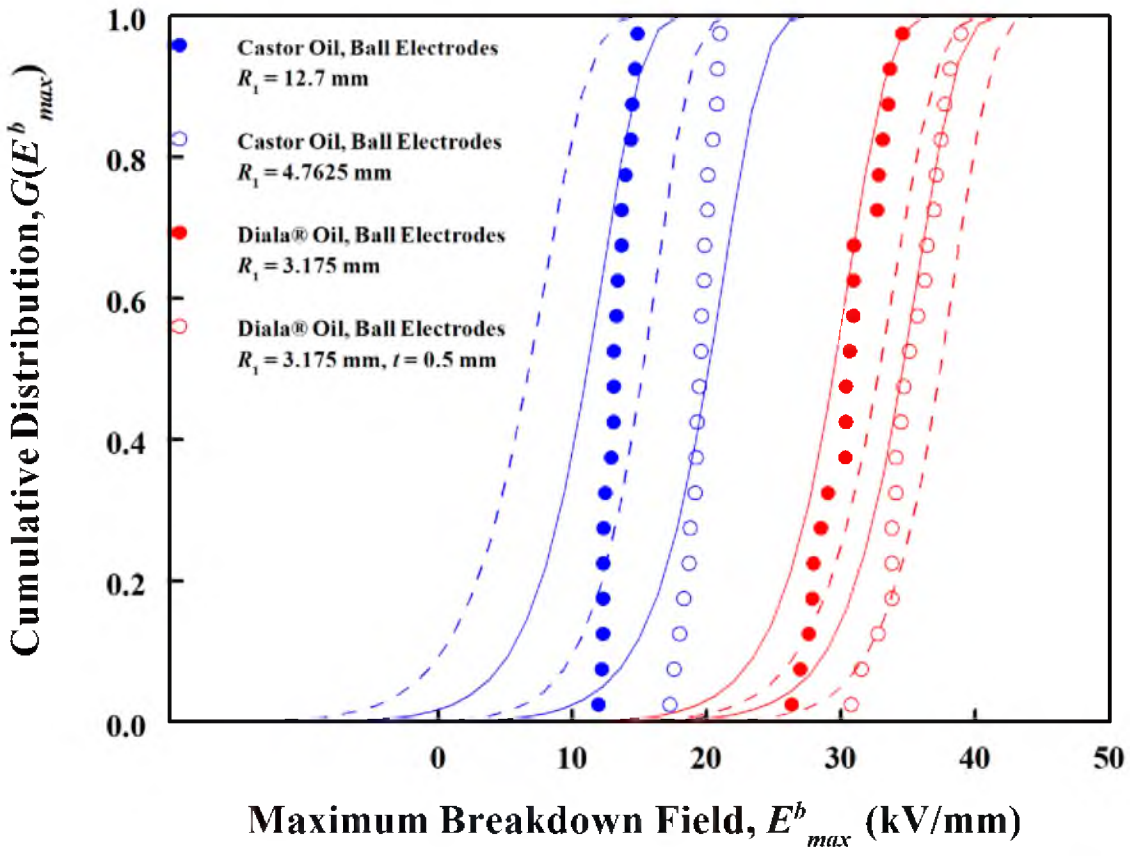

Figure 4.7 Cumulative distribution plots of the breakdown fields measured in four test series compared with extreme-value distributions based on the Laplace (population) distribution with parameters, λ = 3.2 kV/mm, μ = 44.8 kV/mm, and ρ_V = 1998 $\frac{\text{defects}}{\text{mm}^3}$.

probable breakdown field, E_n^*, as a function of the effective stressed volume, V_{eff}, i.e., the scaling relation for the Laplace distribution, is obtained from Equation (4.5) as follows (see Appendix D for derivation):

$$E_n^* = \mu - \lambda \log_e\left(\frac{\rho V_{eff}}{2}\right) \tag{4.23}$$

It should be noted that the scaling relation again contains three unknown parameters: the two population distribution parameters, μ and λ, and the volume concentration of defects, ρ_V. V_{eff} was calculated for each test series using the following equation:

$$V_{eff} = 2\pi \int_{z=0}^{t} \int_{r=0}^{R} \left[\exp\left[\frac{E(r, z_i) - E_{max}}{\lambda} \right] \right] r dr dz \tag{4.24}$$

The scaling relation and the cumulative distribution plots obtained from the optimum Laplace parameters, λ = 2.1 kV/mm, μ = 54.1 kV/mm, and $\rho_V = 1.29*10^8$ defects/mm^3, are shown in Figure 4.8 and Figure 4.9, respectively. It is clear from these figures that the Laplace population distribution represents the scaling (R^2 = 0.92 for Figure 4.6) and the cumulative distributions more accurately than the Weibull distribution. In particular, the shapes of the cumulative distributions are better described by the Laplace distribution function. The breakdown fields measured with specimens of varying thickness are also in line with the scaling relation. The dashed lines in Figure 4.9 represent the 90% confidence bands of the cumulative probabilities of breakdown for the ball electrode tests (R_1 = 12.7 mm) and the tests with 0.5 mm thick disks. The confidence bands were calculated using the 90% confidence limits of the three Laplace distribution parameters, λ, μ, and ρ_V and the

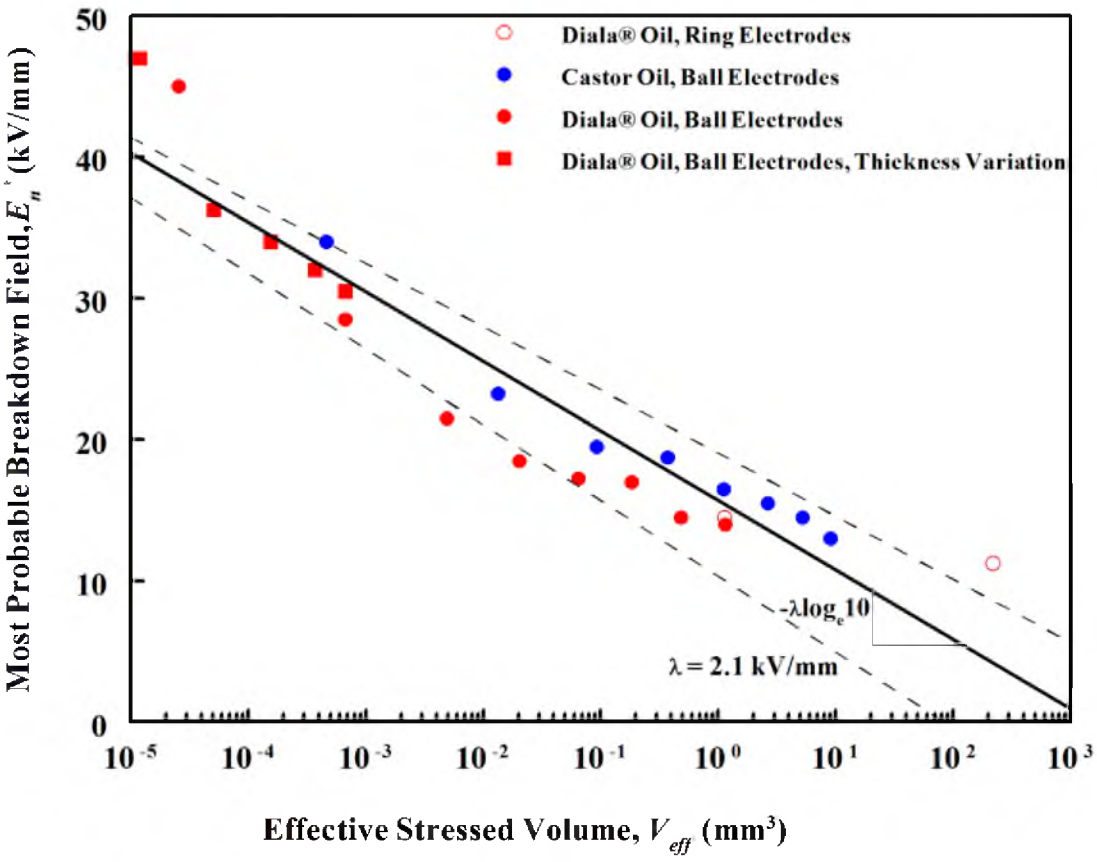

Figure 4.8 Scaling of the most probable breakdown field, E_n^*, with effective stressed volume defined for the Laplace population distribution.

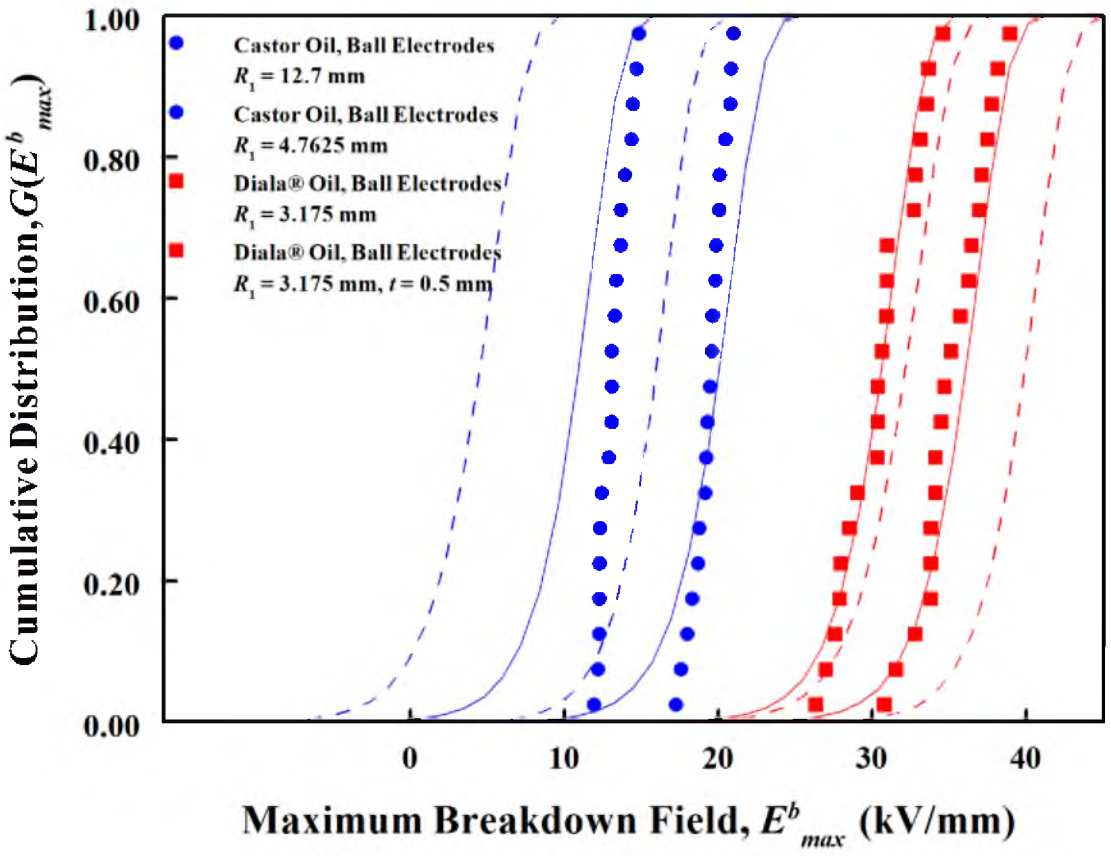

Figure 4.9 Cumulative distribution plots of the breakdown fields measured in four test series compared with extreme-value distributions based on the Laplace (population) distribution with parameters, λ = 2.1 kV/mm, μ = 54.1 kV/mm, and $\rho_V = 1.29*10^8 \frac{\text{defects}}{\text{mm}^3}$.

parametric boot-strap technique.[58] See Appendix E for details regarding the calculation of the confidence bands. The dashed lines in Figure 4.8 also represent the 90% confidence bands of the most probable breakdown field.

4.4 Characterization of Defects and Defect Concentrations

The analysis presented in Section 4.3 indicated that the scaling of the breakdown field of the commercial-grade alumina was in good agreement with a weakest-link failure analysis based on Laplace (population) distribution. The weakest-link failure hypothesis is based on two implicit assumptions: (1) there are defects in the ceramic that raise the local electric field and initiate breakdown, and (2) there should be an adequate concentration of defects, either in the volume (ρ_V) or on the surface (ρ_A) to account for the scaling of the breakdown fields. An attempt was made to identify the nature of such defects and quantify their concentration. The measured defect concentration is then compared with those estimated using weakest-link analysis. Such a comparison can reveal whether volume-distributed defects or surface-distributed defects are pertinent for weakest-link analysis.

4.4.1 Surface Defects on As-Received Commercial-Grade Alumina

Figure 4.10 shows the surface of a commercial-grade alumina specimen as-received from the material supplier. The specimen surface exhibited a number of well-defined cavities with shapes similar to and dimensions comparable to the grains. It was, therefore, concluded that at least a majority of these cavities were grain pullouts resulting from the surface finishing process. Some of the cavities are possibly residual pores exposed on the surface. A secondary structure was observed on the surface of the commercial-grade

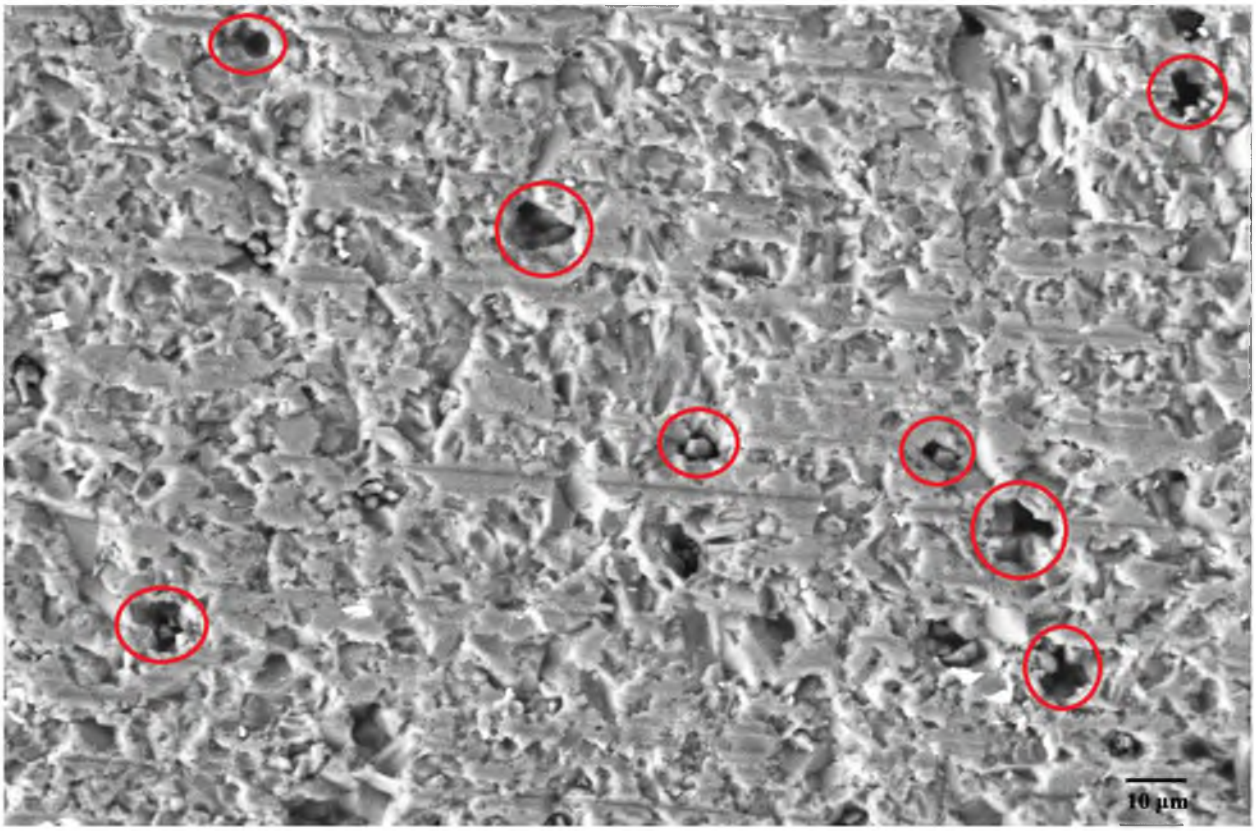

Figure 4.10 SEM image of the surface of commercial-grade alumina with a surface finish as provided by the material supplier (representative cavities circled in red).

alumina. These features were less than 0.5 um in size and did not exhibit the same depth or shape as the larger cavities. These features were attributed to the roughness of the surface finish and were not included in the defect analysis. The measured surface roughness, R_{RMS}, was 0.304 μm.

Figure 4.11 shows a histogram of the distribution of the largest dimension of the defects on the surface of as-received commercial-grade alumina. The average defect size was 8.8 μm. The smallest and the largest defects measured were 2.4 and 21.4 μm, respectively. The surface defect size distribution data were obtained from measuring the sizes of 1000 randomly selected cavities on three specimens using multiple SEM images.

The surface concentration of defects was calculated by counting the total number of cavities on 6 SEM images. Each SEM image represented 0.2 mm^2 surface area. The surface concentration of the defects for the 6 areas ranged from 1883 to 2240 defects/mm^2. The average surface concentration of the defects was 1982 defects/mm^2. This measured surface concentration of defects is close to the value estimated from the surface area scaling of the breakdown field with Laplace distribution (1998 defects/mm^2). A volume concentration of defects was estimated by assuming that all surface cavities were exposed volume cavities and they had the same size as the average. The relation between ρ_V and ρ_A is defined by the following equation[59]:

$$\rho_V = \frac{\rho_A}{\bar{l}} \tag{4.25}$$

In Equation (4.25), ρ_V is the concentration of volume defects, ρ_A is the concentration of surface defects, and $\bar{l}$ is the mean length of the surface cavities. The calculated volume

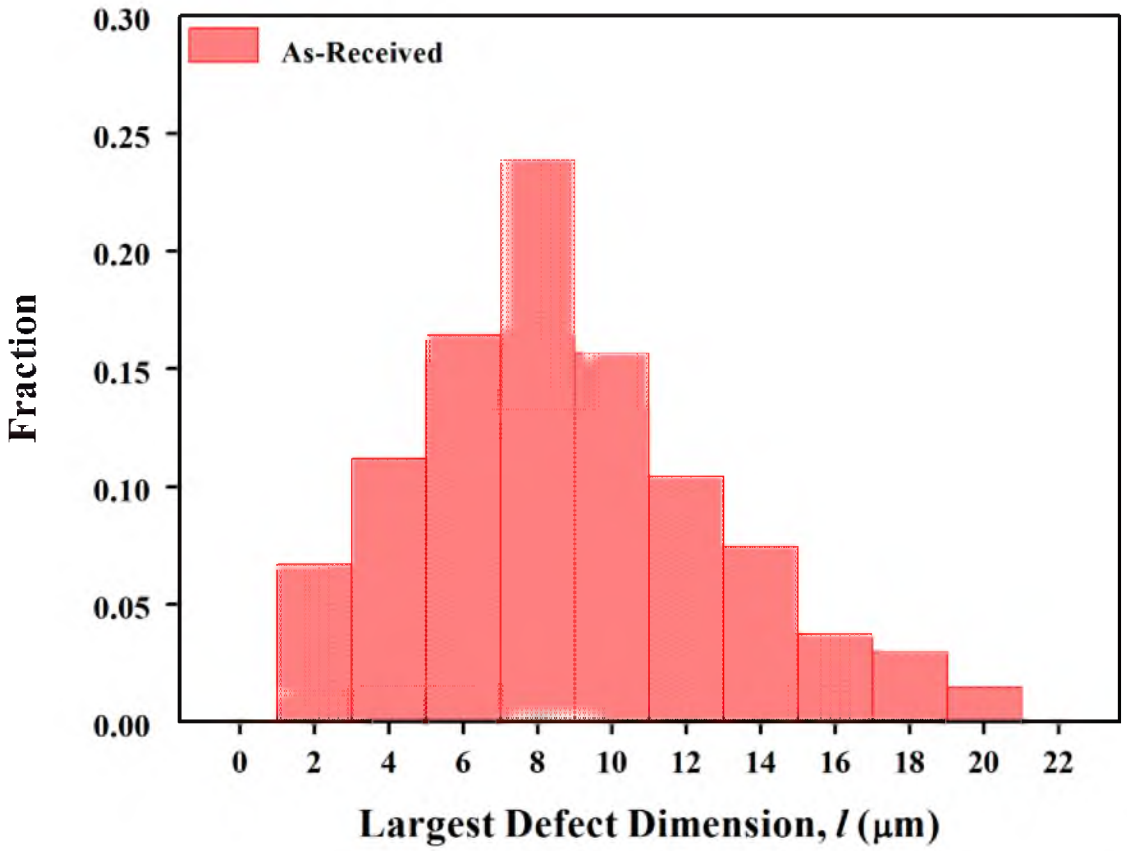

Figure 4.11 Histogram of the defect diameter distribution on the surface of as-received commercial-grade alumina.

concentration of defects was $2.3*10^5$ defects/mm^3. The volume scaling of the breakdown field with Laplace distribution required a volume concentration of defects of $1.3*10^8$ defects/mm^3. The two values differ by three orders of magnitude. This analysis suggested that dielectric breakdown in commercial-grade alumina is likely controlled by surface defects.

4.4.2 Surface Defects on Re-finished Commercial-Grade Alumina

The surfaces of several commercial-grade alumina specimens were re-finished in an attempt to reduce the concentration of surface defects and/or the average size of surface defects. If breakdown is initiated at surface defects, then the breakdown field should scale with the concentration of surface defects. The surfaces of several commercial-grade alumina specimens were re-finished using a grinding/polishing machine (Model MetPrep 4™, Allied High Tech Products, Inc., Rancho Dominquez, CA) (see Appendix A for surface finishing protocol).

Figure 4.12 shows the surface of a commercial-grade alumina specimen with a re-finished surface. The specimen surface exhibited a number of large, well-defined cavities with sizes comparable to the grain size. It was, therefore, concluded that at least a majority of these cavities were grain pullouts resulting from the surface finishing process. Some of the defects are possibly residual pores exposed on the surface. The rest of the surface area is smooth and devoid of the smallest defects which were present on the surface of as-received specimens. The measured surface roughness, R_{RMS}, was 0.0652 μm.

Figure 4.13 shows superimposed histograms of the sizes of the defects on the re-finished surface and the as-received surface. The average defect size on the re-finished

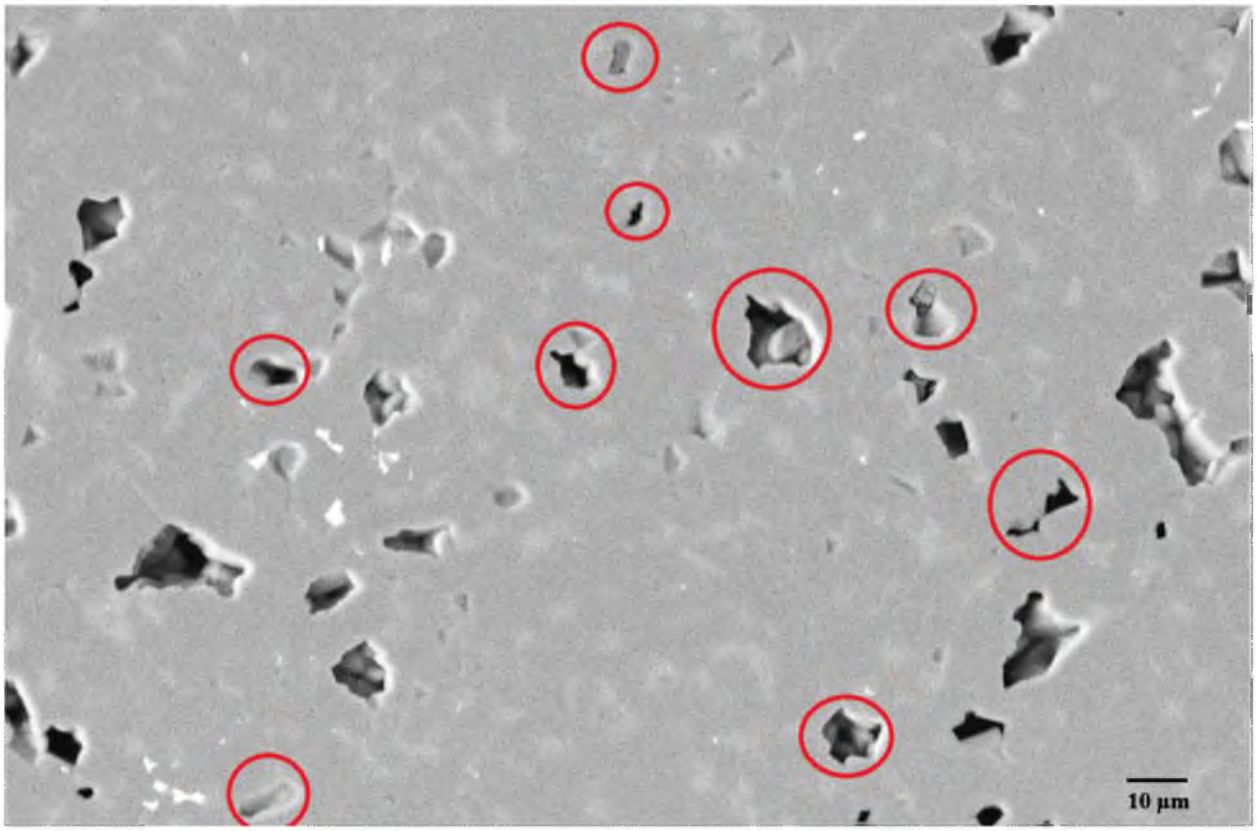

Figure 4.12 SEM image of the surface of commercial-grade alumina with re-finished surface (representative defects circled in red).

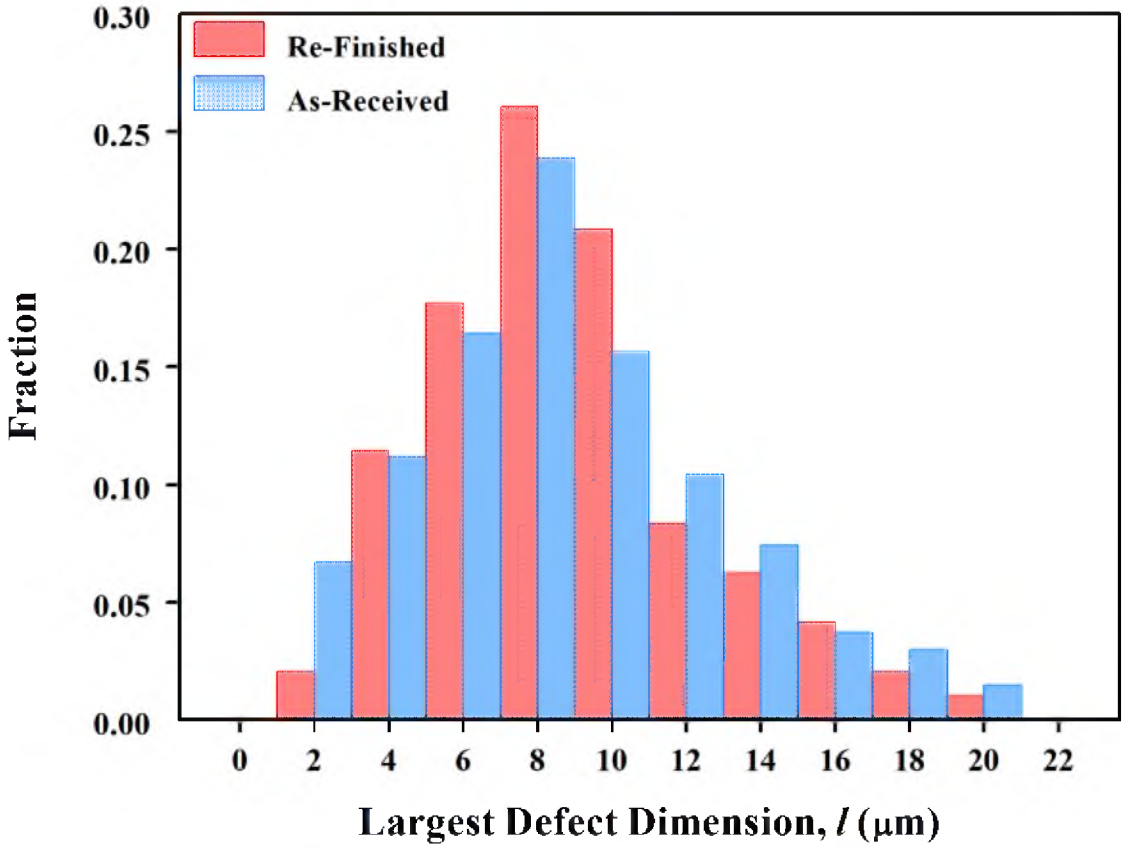

Figure 4.13 Histogram of the defect diameter distribution on the surface of as-received and re-finished commercial-grade alumina.

surface was of 8.5 μm. The smallest and the largest defects measured were 2.9 and 20.8 μm in size, respectively. Refinishing the specimen surface did not significantly affect the surface defect size distribution. Both defect distributions were slightly skewed to the larger side.

The surface concentration of defects on the re-finished surface ranged from 472 defects/mm^2 to 988 defects/mm^2. The average surface concentration of defects was 680 defects/mm^2. Therefore, the defect concentration on the re-finished surface was approximately one third of the defect concentration on the as-received surface. This reduction in the surface concentration of defects likely reflects reduced grain pullout during re-finishing and a higher fraction of intrinsic or volume defects exposed on the surface.

4.4.3 Surface Defects on As-Received and Re-Finished HPFG Alumina

An attempt was made to measure the concentration of surface defects for HPFG alumina. Figure 4.14 shows the surface of a HPFG alumina specimen as-received from the ceramic finisher. The grain structure is visible within the surface recessions. The recessions indicate that multiple neighboring grains are pulled out during surface finishing. The surface recessions do not have smooth defined boundaries. Narrow bands of grains bridge many of the large recessions. For this reason, it was not possible to define where one defect ended and another began. Figure 4.15 shows the surface of a HPFG specimen with a re-finished surface. The specimen surface is smooth, uniform, and free of observable defects. Defect concentrations could not be measured for either of the HPFG alumina surface finishes. The measured surface roughnesses, R_{RMS}, were 0.303 and 0.0517 μm for the as-received and the re-finished surfaces, respectively.

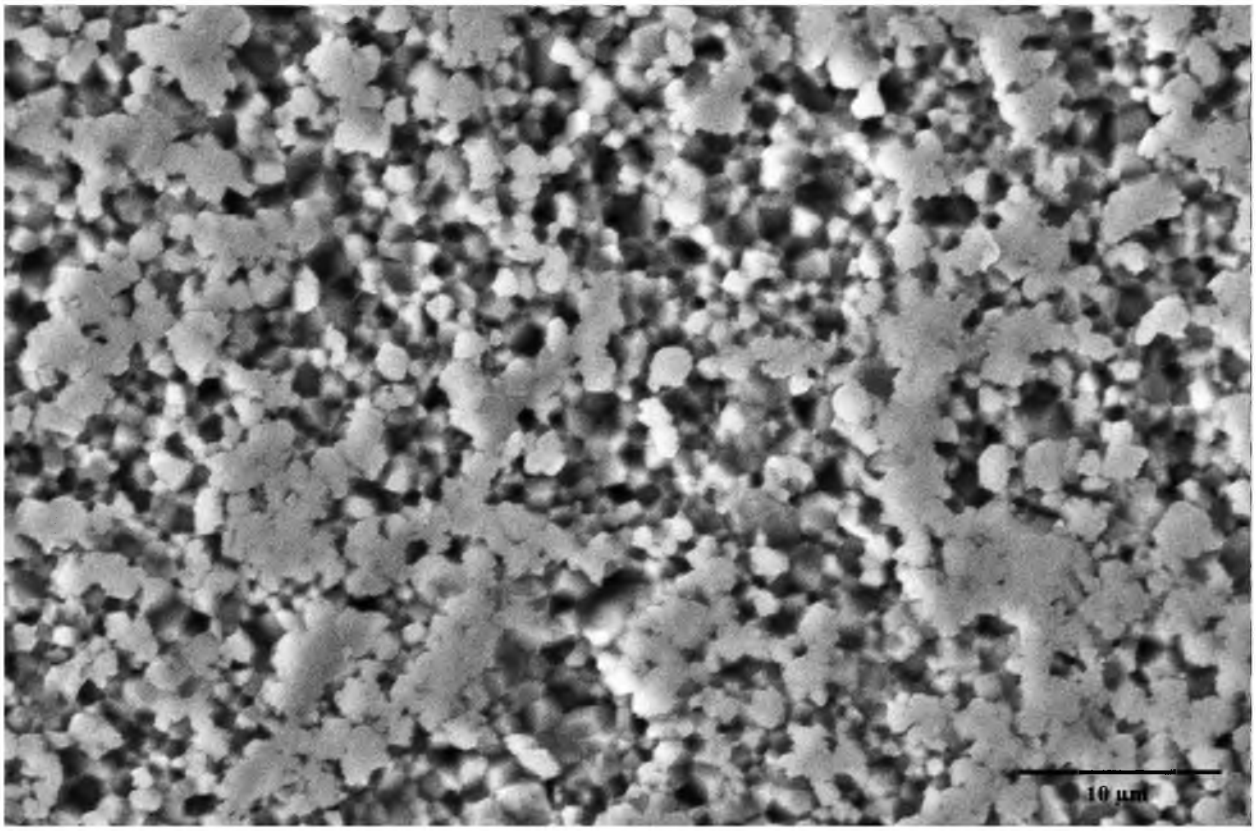

Figure 4.14 SEM image of the surface of HPFG alumina with a surface finish as provided by the ceramic finisher.

Figure 4.15 SEM image of the surface of HPFG alumina with a re-finished surface.

4.4.4 Dielectric Breakdown Fields of As-Received and Re-finished Aluminas

Breakdown testing was conducted on the as-received and the re-finished specimens of commercial-grade and HPFG aluminas. These tests were performed on disk specimens with a radius of 12.7 mm and a thickness of 1 mm with ball electrodes (R_1 = 3.175 mm, R_2 = 12.7 mm) in Diala® oil. Table 4.1 lists the means and standard deviations of the breakdown fields for the as received and the re-finished specimens. The mean breakdown field for the as-received commercial-grade alumina was 30.2 kV/mm.

The mean breakdown field increased to 36.8 kV/mm for the re-finished specimens. The mean breakdown field of the as-received HPFG alumina was 35.1 kV/mm. The mean breakdown field increased to 40.3 kV/mm for the re-finished specimens. The experimental data showed a clear separation between the breakdown electric fields for the as-received and the re-finished specimens. The standard deviation of the breakdown electric field decreased with improved surface finish. These results further support the thesis that surface defects play a crucial role in determining the breakdown fields of the aluminas. The

Table 4.1 Means and standard deviations of the breakdown electric fields for as-received and re-finished specimens.

Specimen Type	E^b_{max} (kV/mm)
Commercial-Grade (as-received)	30.2 ± 2.5
Commercial-Grade (re-finished)	36.8 ± 1.2
HPFG (as-received)	35.1 ± 2.5
HPFG (re-finished)	40.3 ± 2.5

breakdown electric fields for the re-finished commercial-grade alumina were higher than for as-received HPFG alumina. This illustrates that extrinsic factors, such as surface finish, have a greater impact on the breakdown electric field than intrinsic factors.

An attempt was made to see if the increased breakdown field of the re-finished commercial-grade specimens could be explained using the weakest-link theory by using the lower surface defect concentration measured on those surfaces. Figure 4.16 shows the breakdown fields of the commercial-grade and the HPFG aluminas plotted on a cumulative distribution plot. The two solid lines fitted through the data for the commercial-grade alumina were calculated as follows. The extreme-value distribution corresponding to the Laplace (population) distribution can be written in the following form:

$$G_n(E_{\max}^b) = 1 - \exp\left[-\frac{\rho_A A_{eff}}{2}\exp\left\{\left(\frac{E_{\max}^b - \mu}{\lambda}\right)\right\}\right] \tag{4.26}$$

The population distribution parameters, μ = 44.7 kV/mm and λ = 3.2 kV/mm, were already determined for the as-received commercial-grade alumina in Section 4.3.2. It is appropriate to use these parameters for the re-finished commercial-grade alumina because the defect size distribution did not change significantly during refinishing. The ρ_A values used in Equation (4.18) came from the measured concentrations of surface defects on the as-received specimens (ρ_A = 1998 defects/mm^2) and the re-finished specimens (ρ_A = 680defects/mm^2). A_{eff} was calculated using Equation (4.9) using the electric field values from the relevant FEA analysis. The cumulative distribution plots for the as-received and the re-finished commercial-grade alumina show a reasonable fit to the experimental data.

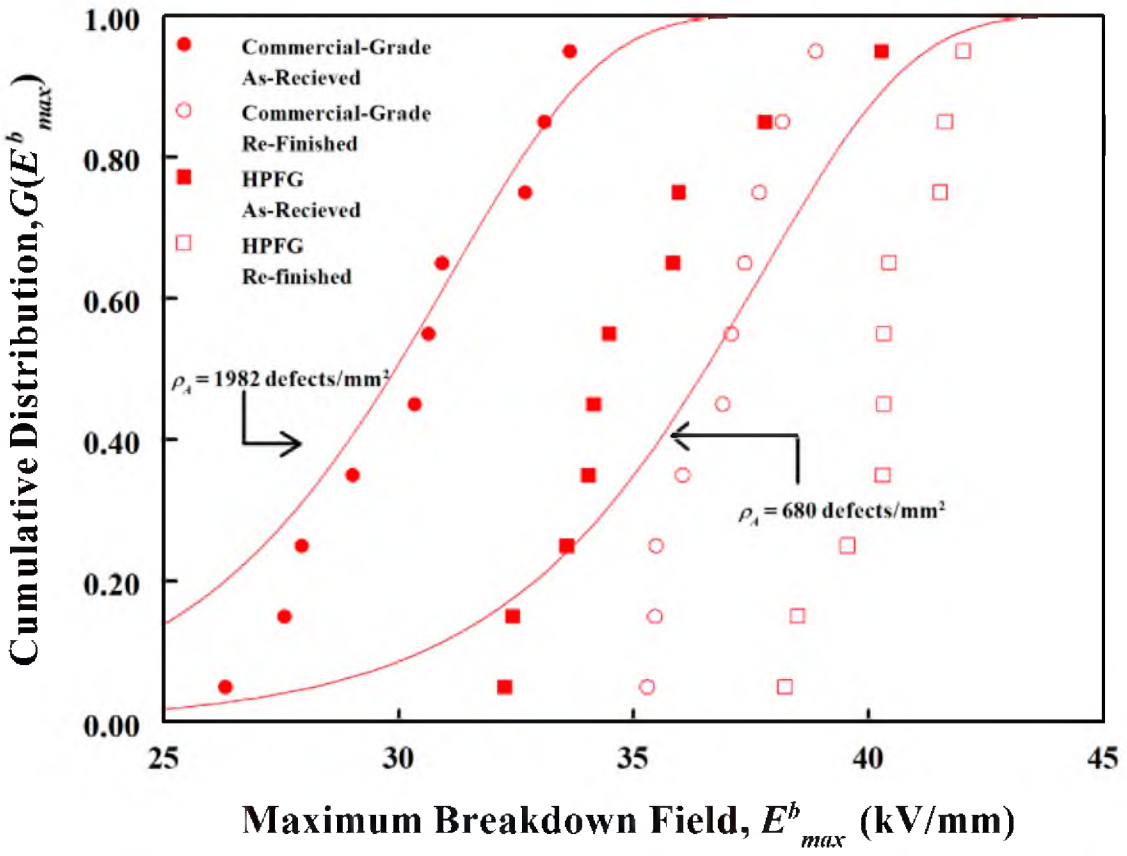

Figure 4.16 Cumulative distribution plots of the breakdown fields measured in four test sets with different surface finishes.

The scaling relation between breakdown field and the concentration of surface defects can be explained using the weakest-link theory.

4.5 FEA Analysis of Surface and Volume Defects

The results of Sections 4.3 and 4.4 indicated that surface cavities are the most likely sites that initiate breakdown in the commercial-grade alumina. This suggests that electric field concentration is greater at surface cavities than volume cavities. An FEA analysis was conducted to test this hypothesis. The FEA model considered both surface and volume cavities of different shapes, sizes, and locations along the central axis. Because of the axi-symmetric model used in the FEA, the geometric shapes of the cavities were limited to hemispheres/spheres, right circular cylinders, and right circular cones centered on the axis of symmetry. The parameters varied in the FEA were sizes of the cavities, their location on the axis of symmetry, and the top electrode radius. All results are reported in terms of normalized electric field concentrations, i.e., the ratio of the maximum electric field in the vicinity of the cavity and the maximum electric field in the absence of the cavity. The surface cavities were assumed to contain Diala® oil, while the volume cavities were assumed to contain air. The minimum thickness of the oil layer between the specimen surface and the electrodes was maintained at $\delta = 0.0001$ mm for all cavities.

4.5.1 Cavity Shape Analysis

Figures 4.10 and 4.12 show a variety of cavity shapes on the surface of as-received and re-finished commercial-grade alumina. Therefore, surface and volume cavities of

different shapes were studied to determine the effect of cavity shape on electric field. If the scaling of electric field with cavity diameter was similar for all defect cavities, then a representative cavity shape could be used to compare the electric field concentrations at surface and volume cavities.

Figure 4.17 shows schematics of the surface cavities and their dimensions for conical, cylindrical, and hemispherical cavities. The cavities were centered at the contact point on the top specimen surface. The height, h, was half of the diameter, d, for all cavity shapes. The FEA was conducted for disk specimens (r = 38.1 mm t = 4 mm) of commercial-grade alumina with ball electrodes (R_1 = 1.5875 mm R_2 = 12.7 mm) in Diala® oil.

Figure 4.18 shows plots of the normalized maximum electric field, (E_{max}^c/E_{max}), as functions of the cavity size and cavity shape. E_{max}^c was the maximum electric field in the ceramic in the presence of a cavity and E_{max} was the maximum electric field in the specimen in the absence of the cavity. The maximum electric field, E_{max}^c always occurred on the specimen surface at the cavity rim. The normalized maximum electric field increased with increasing cavity diameter for all cavity shapes. However, the increase in the normalized maximum electric field with cavity diameter was rapid for small cavities less than 5 μm in diameter. The increase in the field concentration for cavities with diameters larger than 5 μm was more gradual. The scaling of the normalized electric field with cavity diameter was similar for all cavity shapes.

Figure 4.19 shows schematics of subsurface cavities in the shapes of cone, cylinder, and sphere. The cavities were centered at a depth z from the surface along the electrode axis. The height, h, was equal to the diameter, d, for all the cavity shapes. The FEA was conducted for disk specimens (r = 38.1 mm t = 4 mm) of commercial-grade alumina with

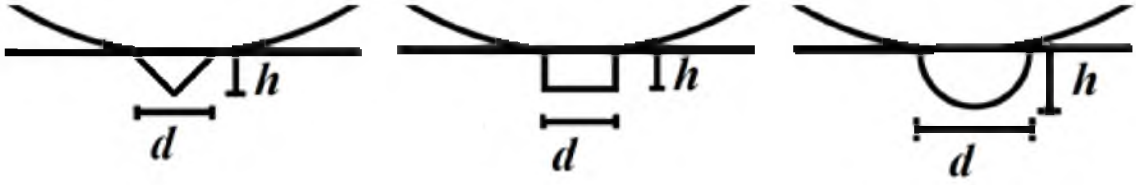

Figure 4.17 Schematics of surface cavities and their dimensions for conical, cylindrical, and hemispherical cavities.

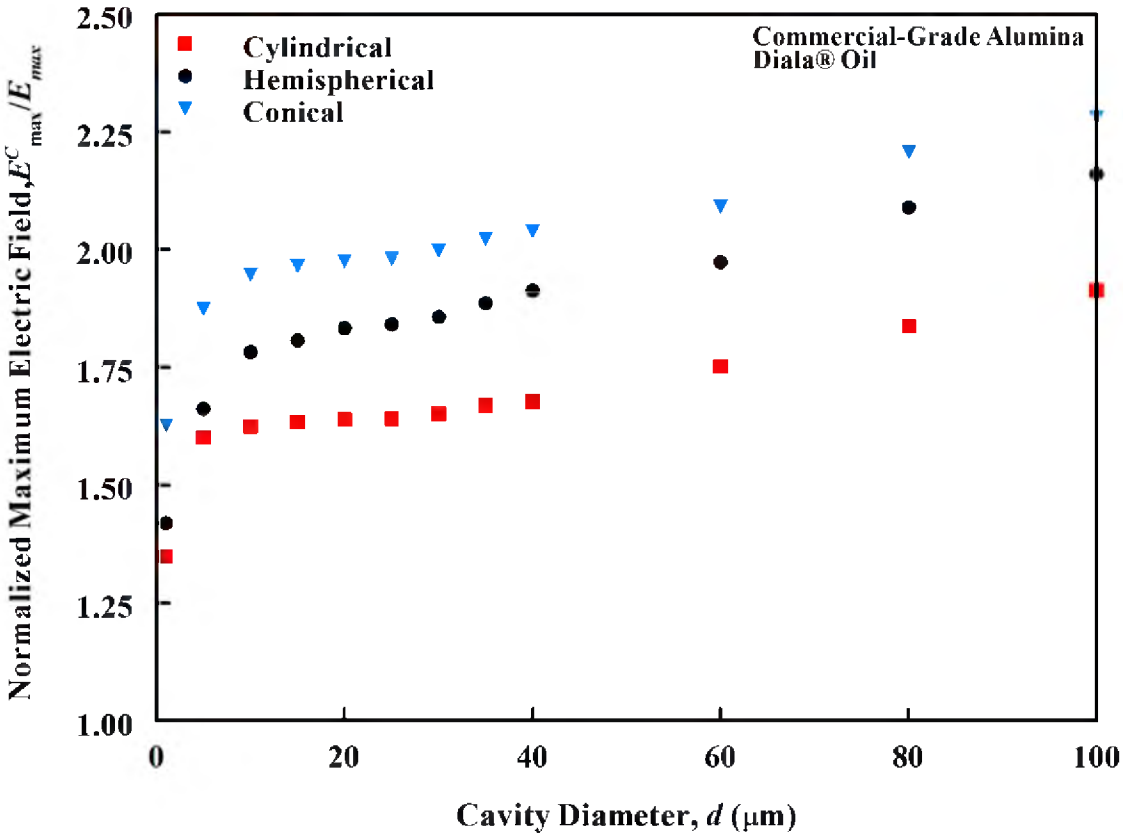

Figure 4.18 Variations in the normalized maximum electric field with cavity shape and diameter on the top specimen surface at the electrode contact point.

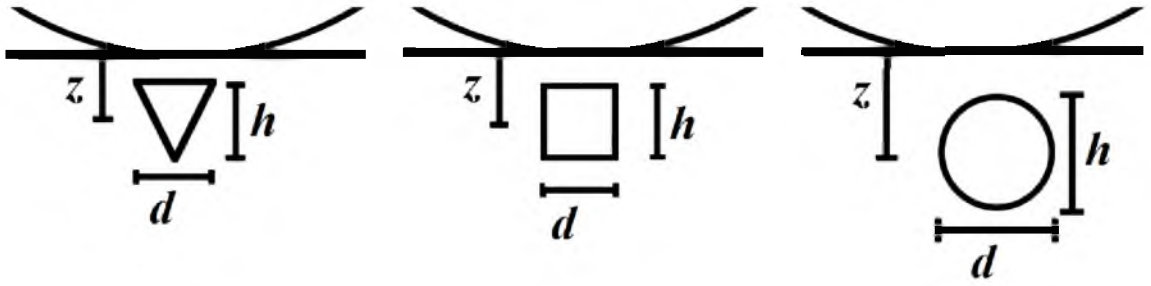

Figure 4.19 Schematics of volume cavities and their dimensions for subsurface conical, cylindrical, and spherical cavities.

conducted for disk specimens (r = 38.1 mm t = 4 mm) of commercial-grade alumina with ball electrodes (R_1 = 1.5875 mm R_2 = 12.7 mm) in Diala® oil.

Figure 4.20 shows plots of the normalized maximum electric field as functions of cavity depth and shape for the subsurface cavities with a diameter of 5 μm. For spherical cavities, the normalized maximum electric field occurred along the equator. For conical cavities, the normalized maximum electric field occurred along the base of the cone. For cylindrical cavities, the normalized maximum electric field occurred along the base nearest to the surface. The normalized maximum electric field decreased with increasing cavity depth for all cavity shapes tested. The normalized maximum electric field occurred on the specimen surface, not at the cavity, for cavity depths greater than 192 μm, 94 μm, and 68 μm for cylindrical, spherical, and conical cavities, respectively. Therefore, only the cavities near the specimen surface are likely to influence the breakdown. The scaling of the normalized electric field with cavity depth, z, was similar for all cavity shapes.

4.5.2 Electrode Radius Analysis

The results of Section 3.2 showed that the electrical field near the contact point varies significantly in intensity and scaling with electrode radius. Therefore, top ball electrodes of varying radii were used to determine the scaling of the normalized electric field with electrode radius for a given cavity diameter, d, and depth, z, for surface and volume cavities. The testing was conducted using the commercial-grade alumina (r = 38.1 mm t = 4 mm) with ball electrodes (R_1 = 1.5875, 3.175, 6.35, or 12.7 mm R_2 = 12.7 mm) in Diala® oil.

Figure 4.21 shows the variation in maximum normalized electric field with cavity

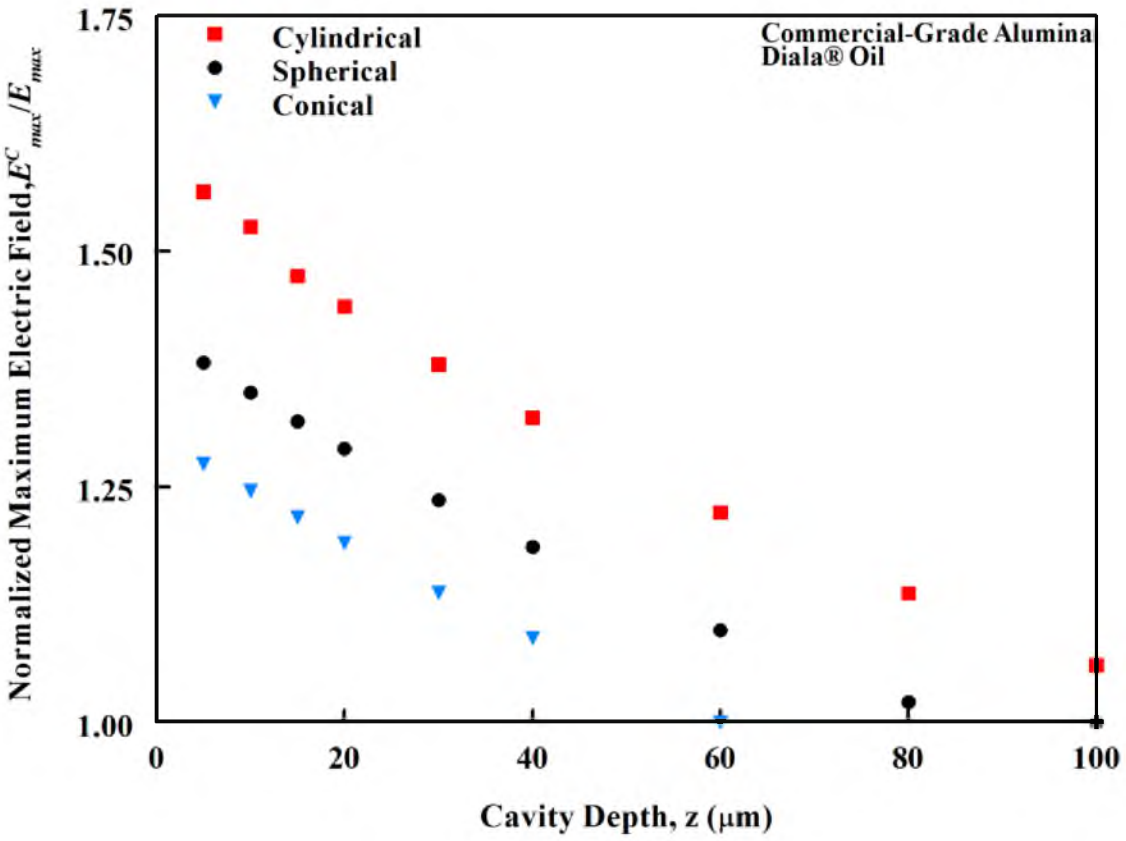

Figure 4.20 Variations in the normalized maximum electric fields with cavity depth and shape for a cavities of 5 μm diameter.

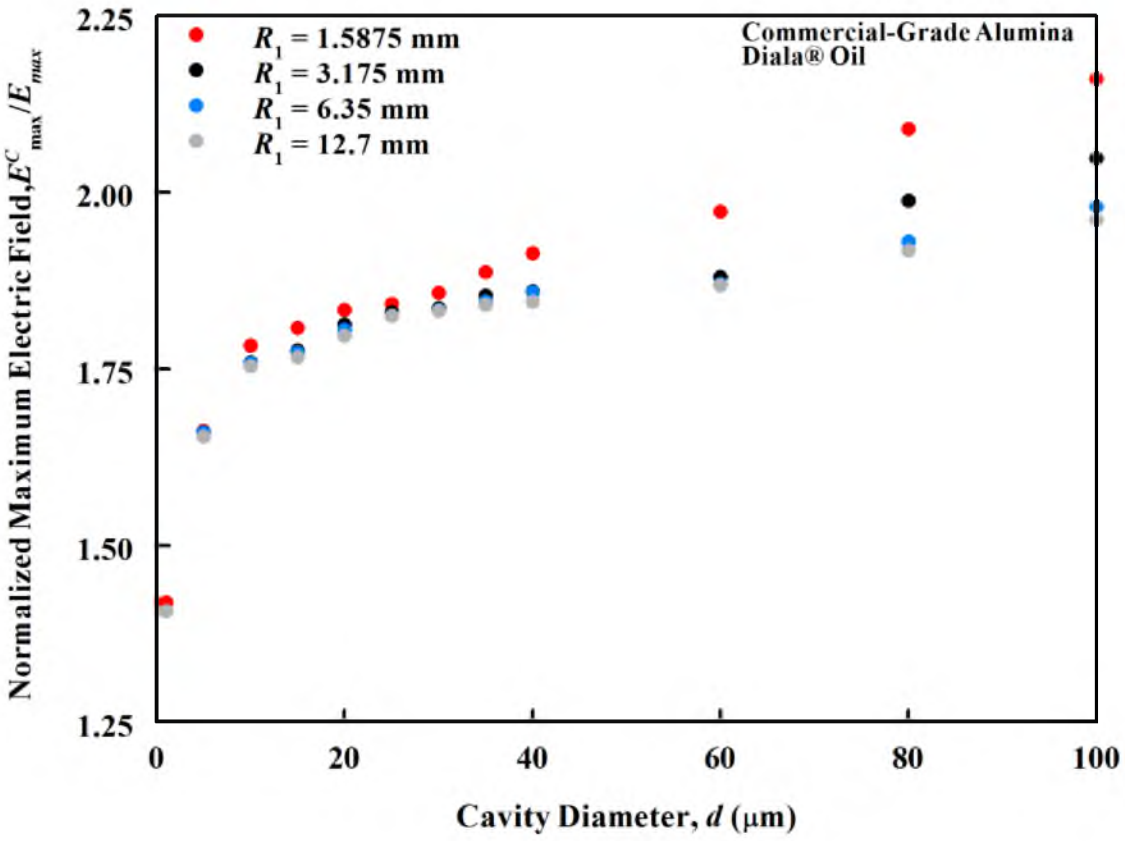

Figure 4.21 Variation in maximum normalized electric field with hemispherical surface cavity diameter and top electrode radius.

diameter and top electrode radius for hemispherical surface cavities. The cavities were centered at the contact point on the top specimen surface. The height, h, was half of the diameter, d, for all cavity shapes. For a given cavity diameter, the value of maximum normalized electric field increased with decreasing top electrode radius. The maximum normalized electric field going from a cavity diameter of 0 μm to a cavity diameter of 100 μm increased by a factor of 2.16 and 1.96 for R_1 = 1.5875 mm and R_1 = 12.7 mm, respectively.

Figure 4.22 shows the variation in maximum normalized electric field with cavity depth and top electrode diameter for a spherical volume cavity with a diameter of 5 μm. The cavities were centered at the contact point on the top specimen surface. The midpoints of the cavities were located at a depth, z, below the top specimen surface. The height, h, was equal to the diameter, d, for all cavity shapes. For a given cavity diameter, the maximum normalized electric field increased with increasing top electrode radius. The maximum normalized electric field occurred on the specimen surface, not at the cavity site, for cavity depths greater than 94 μm, 167 μm, 483 μm, and 795 μm for R_1 = 1.5875 mm, R_1 = 3.175 mm, R_1 = 6.35 mm, and R_1 = 12.7 mm, respectively. Therefore, only volume cavities near the specimen surface influence breakdown strength. Additionally, smaller electrodes further bias towards surface and near-surface cavities.

4.5.3 Surface and Volume Cavity Electric Field Comparison

In Sections 4.5.1 and 4.5.2, it was determined that maximum normalized electric field decreases with increasing depth for a volume cavities irrespective of electrode radius

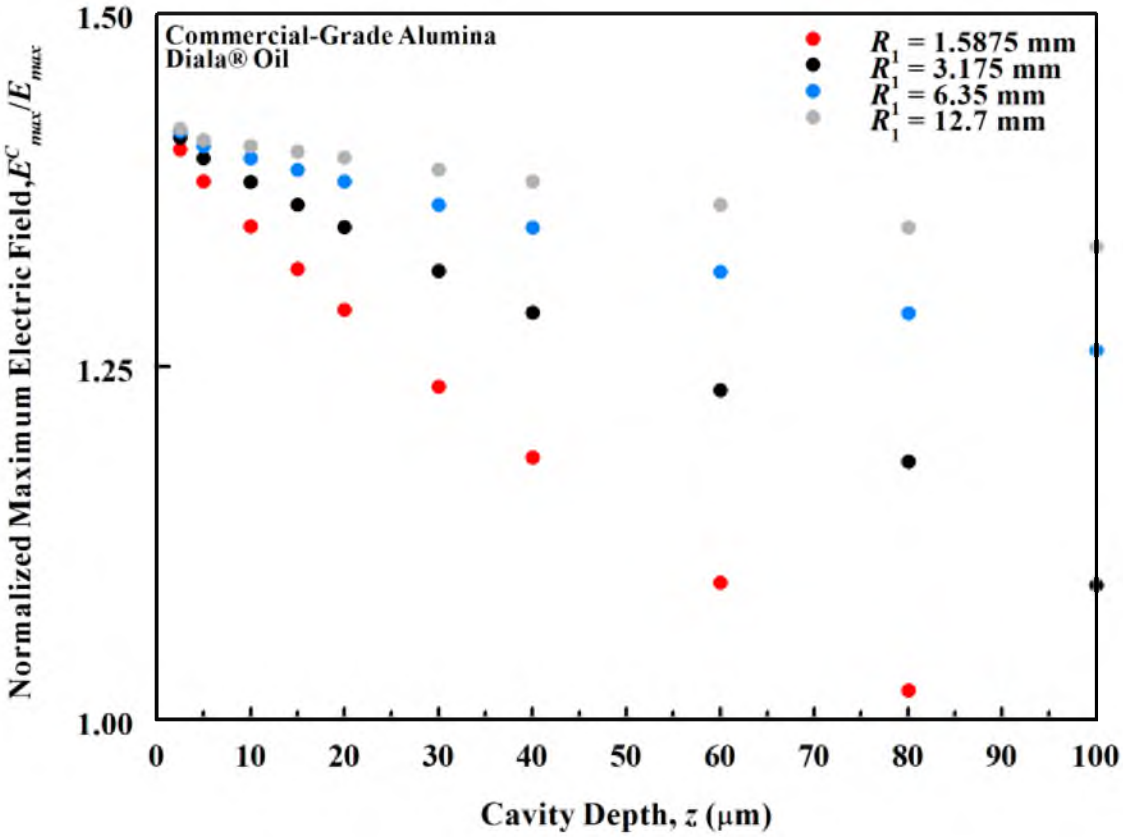

Figure 4.22 Variation in maximum normalized electric field with cavity depth and top electrode radius for a spherical volume cavity with a diameter of 5 μm.

and cavity shape. Therefore, the value of the maximum normalized electric field for spherical volume cavities 0.001 μm below the specimen surface were compared to hemispherical surface cavities with respect to cavity diameter. The testing was conducted using the commercial-grade alumina (r = 38.1 mm t = 4 mm) with ball electrodes (R_1 = 1.5875 mm R_2 = 12.7 mm) in Diala® oil.

Figure 4.23 shows the maximum normalized electric field versus cavity diameter for hemispherical surface cavities and spherical volume cavity with a cavity depth, $z = r +$ 0.001 μm. For a given cavity diameter, a surface cavity always results in a larger maximum normalized electric field value than a volume cavity. The maximum normalized electric field for surface cavities is 1.01 and 1.95 times the value for volume cavities for d = 1 μm and d = 100 μm, respectively. Based on Figure 4.13, 86 and 82% of cavities are larger than 6 μm for commercial-grade alumina with concentrations of defects of 680 and 1982 defects/mm^2, respectively. A hemispherical surface cavity with a diameter of 6 μm has a maximum normalized electric field value that is 1.21 and 1.25 times the maximum normalized electric field value of a spherical volume cavity with a diameter of 1 μm and 6 μm, respectively. Therefore, it can be concluded that the breakdown initiation sites are surface cavities.

4.6 Breakdown Mechanism

The primary dielectrics breakdown mechanisms reported in the literature are electrical (avalanche) breakdown and thermal breakdown. Electrical breakdown occurs when the applied voltage is sufficiently large so that the electrode emits free electrons by Fowler-Nordhem or Shottky emission[10, 60]. These electrons have a sufficient energy to

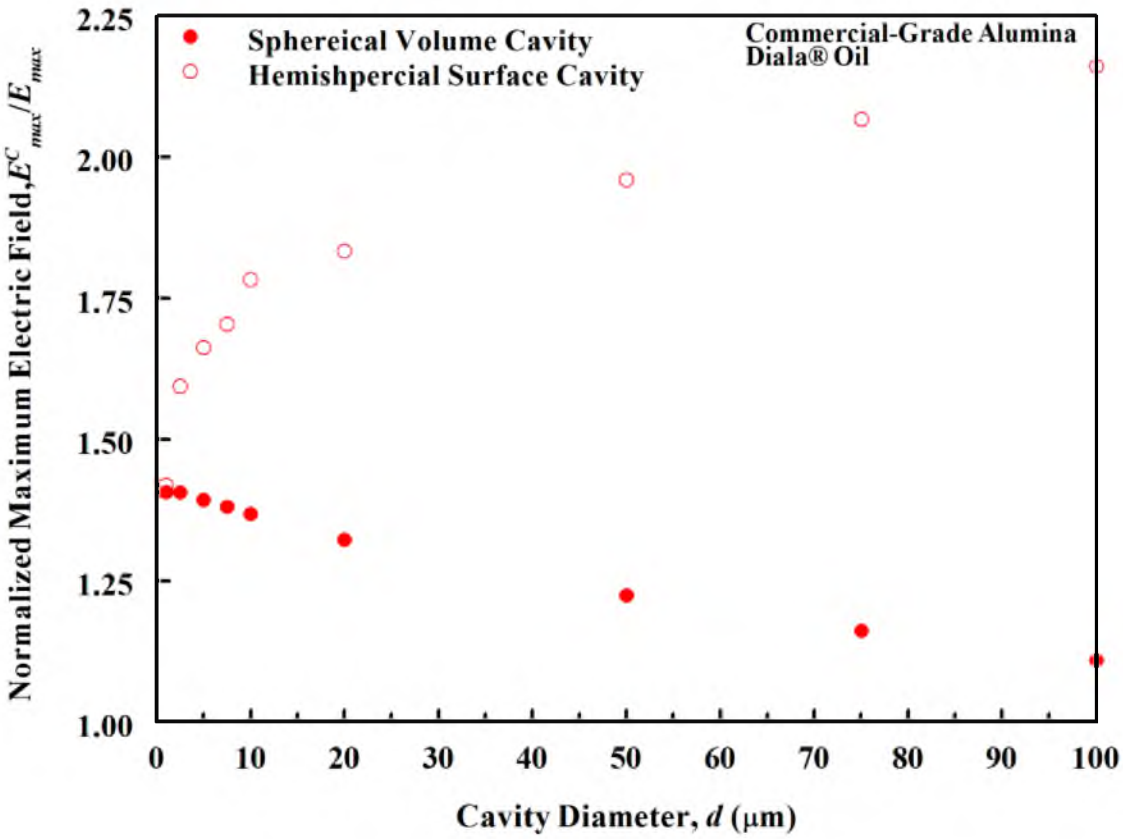

Figure 4.23 Variation in maximum normalized electric field with cavity diameter for hemispherical surface cavities and volume cavities (z = radius + 0.001 μm)

cause impact ionizations. This promotes a second electron from a state in the valence band to a state in the condition band, creating an electron-hole pair[61]. The presence of defects lowers the applied voltage necessary to reach electrical breakdown by concentrating the electric field. Free electrons continually create new electron-hole pairs by impactionization[10]. Once sufficient electron density has been generated, the alumina specimen is irreversibly damaged and local heating occurs leading to melting[10, 11, 62, 63]. Thermal breakdown occurs when the rate of heat generation is greater than the rate of heat dissipation. Heat is generated as molecules continually rearrange to align with the electric filed generated by an alternating current (dielectric heating) or from charged particle collisions (joule heating). As the temperature rises, the material properties such as electrical conductivity, heat capacity, and dielectric loss factor scale with temperature. This leads to a faster rise in temperature until the melting point of the material is exceeded. The literature suggests that electric breakdown is the primary mechanism at lower temperatures while thermal breakdown is the primary mechanism at higher temperatures. Additionally, research involving barium titanate ceramics has suggested that electrical breakdown is associated with extrinsic defects while thermal breakdown is associated with intrinsic defects [64, 65].

In this study, all successful breakdown tests exhibit a large through-thickness cylindrical puncture with melting and solidification features. It was unclear whether the melting was due to thermal breakdown or electrical breakdown. Attempts were made to arrest specimen in a "prebreakdown" state by varying the threshold current of the breakdown tester between 1 μA and 75 μA. All testing conducted with a threshold current of $\geq$ 4 μA resulted in a typical puncture site with visible melting. All testing conducted

with a threshold current of ≤ 2 μA resulted in no visible puncture and no surface damage. Testing conducted with a threshold current between 2 and 4 μA resulted in either no surface damage or a typical puncture with visible melting. This study was unable to confirm the breakdown mechanism with any certainty.

CHAPTER 5

CONCLUSIONS

1. The dielectric breakdown field of alumina exhibits a scaling effect. Electrode size and shape, dielectric media, and specimen thicknesses that spatially confine the electric field to small volumes or areas produce high breakdown fields.
2. Extrinsic factors (electrode size and shape, dielectric media, specimen thickness, surface finish) have a much greater influence on breakdown strength than intrinsic factors (purity and grain size).
3. The scaling of the breakdown field of alumina with electrically-stressed area is consistent with the weakest-link failure concept.
4. Lowest-values distribution based on the Laplace (population) distribution accurately represent the scaling and the cumulative distribution of breakdown fields measured in tests employing different electrode geometries, dielectric liquid media, and specimen thicknesses.
5. Lowest-value distribution based on the Weibull distribution does not adequately describe the scaling and the cumulative distributions. Specifically, the shapes of the cumulative breakdown distributions for small stressed volumes deviate significantly from the measured distributions.

6. Dielectric breakdown of alumina is controlled by surface defects. This is evidenced by an increase in breakdown fields with decreasing concentration of surface defects. This is also evidenced by FEA of surface and volume defects. Surface defects increase the local electric field by a greater degree than volume defects.

CHAPTER 6

RECOMMENDATIONS FOR FURTHER STUDY

In this study, all tests stressed multiple defects and it was not possible to determine the defect at which breakdown was initiated. To circumvent this problem, it is suggested that "artificial" defects be applied to the specimen surface of alumina disks. The disks should be polished using the protocol described in Appendix A to remove as many defects from the specimen surface as possible. The artificial defects should be applied using a Vicker's indenter. By varying the load, defects of varying size can be created. Testing should be conducted with the ball electrode contact point centered on the defect. Re-finished HPFG alumina specimens should be used due to the limited number of surface defects.

Each defect should be imaged before and after the breakdown testing to determine the defect size, the presence and size of cracking, and to determine if the defect site was the location at which breakdown was initiated. If the breakdown location is shown to be located at the defect site, two additional experiments should be conducted. First, the electrode contact point should be located at varying distances away from the defect location. The breakdown voltage should be compared to the distance between the electrode and defect location. Using FEA modeling of the electrode and defect position, it may be possible to determine the electric field required to initiate breakdown for a given defect

size. Second, two defects of varying size should be created near the electrode contact point. By introducing a second defect and comparing the breakdown results to those for a single defect, it may be possible to determine the interactions between multiple defects.

Additional FEA studies should be conducted to determine the interactions of multiple defects. A three-dimensional FEA model should be used in these studies. The model used to date was an axi-symmetrical model which limited studies with symmetrical defects located along the axis of symmetry. The results of this study show that the majority of breakdowns are not located at the contact point. It is therefore critical to understand the concentration of the electric field caused by defects away from the axis of symmetry.

In this study, we concluded that the smallest-value distribution based on the Laplace (population) distribution accurately represent the scaling and the cumulative distribution of breakdown fields. Although the fits were reasonable, work should be done to select a new probability distribution that fits the data better. This can be done by testing additional probability distributions or developing a novel probability distribution to fit the data sets.

APPENDIX A

SURFACE FINISHING PROTOCOL

Commercial-grade and HPFG alumina specimens with a radius of 12.7 mm and a thickness of 1 mm were placed at the bottom of a 2-part mounting cup (19.05 mm radius). EpoxyMount (Allied High Tech Products, Inc., Rancho Dominguez, CA) was poured into the mounting cup to a height of 40 mm. The cups were then placed under vacuum for 1 hour to remove all air pockets from the epoxy. After being vacuumed, the epoxy was allowed to harden overnight. The specimens were polished three at a time using an automated grinding/polishing machine (Model MetPrep 4™ Grinding/Polishing Machine, Allied High Tech Products, Inc., Rancho Dominguez, CA). The protocol in Table A.1 was used to finish the surface of both commercial-grade and HPFG alumina specimens. After the surface finishing was completed, the epoxy was removed from the specimens using Epoxy Dissolver (Allied High Tech Products, Inc., Rancho Dominguez, CA).

Table A.1 Surface re-finishing protocol.

Step	Particle Size	Duration	Force	RPM	Pad
1	30 um	30 min	111 N	200	NA
2	15 um	20 min	111 N	200	Texmet® 2500
3	9 um	30 min	111 N	200	Texmet® 2500
4	3 um	40 min	111 N	200	Texmet® 2500
5	1 um	20 min	89 N	200	Texmet® 1500
6	0.05 um	40 min	45 N	200	Texmet® 1000

APPENDIX B

DERIVATION OF of *En** IN SAMPLES OF SIZE *n* DRAWN FROM A WEIBULL DISTRIBUTION

Let the cumulative distribution of the breakdown electric fields of a specimen be given by the following Weibull distribution:

$$F(E) = 1 - \exp\left[-\left(\frac{E}{E_0}\right)^m\right] \tag{B.1}$$

In Equation (B.1), m is the shape parameter and E_0 is the scale parameter. The corresponding population density distribution, $f(E)$, is given by:

$$f(E) = \frac{dF(E)}{dE} = m\frac{E^{m-1}}{E_0{}^m}\exp\left[-\left(\frac{E}{E_0}\right)^m\right] \tag{B.2}$$

The distribution of the smallest value in samples of size n drawn from the population is given by the probability density function:

$$g_n(E) = nf(E)[1 - F(E)]^{n-1} \tag{B.3}$$

or by the cumulative distribution function:

$$G_n(E) = 1 - [1 - F(E)]^n \tag{B.4}$$

Substitute Equations (B.1) and (B.2) into Equation (B.3):

$$g_n(E) = n\left(m\frac{E^{m-1}}{E_0^{\,m}} \exp\left[-\left(\frac{E}{E_0}\right)^m \right] \right) \left[\exp\left[-\left(\frac{E}{E_0}\right)^m \right] \right]^{n-1} \tag{B.5}$$

The most probable value of the breakdown field, E_n^*, in samples of size n is defined by

$$\frac{dg_n}{dE}\left(E_n^*\right) = 0 \tag{B.6}$$

Take the first derivative of Equation (B.5):

$$\frac{dg_n}{dE} = n\frac{d}{dE}\left(\left(m\frac{E^{m-1}}{E_0^{\,m}} \exp\left[-\left(\frac{E}{E_0}\right)^m \right] \right) \left[\exp\left[-\left(\frac{E}{E_0}\right)^m \right] \right]^{n-1} \right)$$

$$\frac{dg_n}{dE} = n\left\{ \begin{array}{l} m\frac{E^{m-1}}{E_0^{\,m}} \exp\left[-\left(\frac{E}{E_0}\right)^m \right] \frac{d}{dE}\left[\exp\left[-\left(\frac{E}{E_0}\right)^m \right] \right]^{n-1} \\ + \left[\exp\left[-\left(\frac{E}{E_0}\right)^m \right] \right]^{n-1} \frac{d}{dE} m\frac{E^{m-1}}{E_0^{\,m}} \exp\left[-\left(\frac{E}{E_0}\right)^m \right] \end{array} \right\}$$

$$\frac{dg_n}{dE} = n\left\{\begin{array}{l} m\frac{(m-1)E^{m-2}}{E_0^{\,m}}\exp\left[-\left(\frac{E}{E_0}\right)^m\right]\exp\left[-\left(\frac{E}{E_0}\right)^m\right]^{n-1} \\ -m\frac{E^{m-1}}{E_0^{\,m}}\exp\left[-\left(\frac{E}{E_0}\right)^m\right]\frac{mE^{m-1}}{E_0^{\,m}}\left[\exp\left[-\left(\frac{E}{E_0}\right)^m\right]\right]^{n-1} \\ -m\frac{E^{m-1}}{E_0^{\,m}}\exp\left[-\left(\frac{E}{E_0}\right)^m\right](n-1)\left[\exp\left[-\left(\frac{E}{E_0}\right)^m\right]\right]^{n-2} \\ *\,m\frac{E^{m-1}}{E_0^{\,m}}\exp\left[-\left(\frac{E}{E_0}\right)^m\right] \end{array}\right\} \qquad \text{(B.7)}$$

Substitute Equation (B.7) into Equation (B.6):

$$0 = nm(m-1)\frac{E_n^{*m-2}}{E_0^{\,m}} - \frac{nm^2E_n^{*(m-1)}}{E_0^{\,2m}} - \frac{n(n-1)m^2E_n^{*2(m-1)}}{E_0^{\,2m}}$$

$$0 = \left[nm(m-1) - \frac{nm^2E_n^{*m}}{E_0^{\,2m}} - \frac{n(n-1)m^2E_n^{*m}}{E_0^{\,m}}\right]\frac{E_n^{*m-2}}{E_0^{\,m}}$$

$$0 = \left[nm(m-1) - \frac{nm^2E_n^{*m}}{E_0^{\,2m}} - \frac{n(n-1)m^2E_n^{*m}}{E_0^{\,m}}\right]$$

$$\frac{E_n^{*m}}{E_0^{\,m}}\left[nm^2 + n(n-1)m^2\right] = nm(m-1)$$

$$\frac{E_n^{*m}}{E_0^{\,m}}\left[m + m(n-1)\right] = (m-1)$$

$$E_n^{*m} = E_0{}^m \frac{m-1}{mn}$$

$$E_n^* = E_0 \frac{\left(1-\frac{1}{m}\right)^{\frac{1}{m}}}{n^{\frac{1}{m}}} \tag{B.8}$$

Equation (B.8) defines the dependence of the most probable breakdown field, E_n^* on the sample size *n* drawn from a Weibull Distribution.

APPENDIX C

DERIVATION OF E_n^* IN SAMPLES OF SIZE n DRAWN FROM A LAPLACE DISTRIBUTION

Let the cumulative distribution of the breakdown electric fields of a specimen be given by the following Laplace distribution:

$$F(E) = \frac{1}{2}\exp\left[\left(\frac{E-\mu}{\lambda}\right)\right] \tag{C.1}$$

In Equation (C.1), μ is the location parameter and λ is a scale parameter. The corresponding population density distribution, $f(E)$, is given by:

$$f(E) = \frac{dF(E)}{dE} = \frac{1}{2\lambda}\exp\left[\frac{E-\mu}{\lambda}\right] \tag{C.2}$$

The distribution of the smallest value in samples of size n drawn from the population is given by the probability density function:

$$g_n(E) = nf(E)[1-F(E)]^{n-1} \tag{C.3}$$

or by the cumulative distribution function:

$$G_n(E) = 1 - [1 - F(E)]^n \tag{C.4}$$

Substitute Equations (C.1) and (C.2) into Equation (C.3):

$$g_n(E) = n\frac{1}{2\lambda}\exp\left[\frac{E-\mu}{\lambda}\right]\left[1 - \frac{1}{2}\exp\left[\frac{E-\mu}{\lambda}\right]\right]^{n-1} \tag{C.5}$$

The most probable value of the breakdown field, E_n^*, in samples of size n is defined by

$$\frac{dg_n}{dE}\left(E_n^*\right) = 0 \tag{C.6}$$

Take the first derivative of Equation (C.5):

$$\frac{dg_n}{dE} = n\frac{1}{2\lambda}\frac{d}{dE}\exp\left[\frac{E-\mu}{\lambda}\right]\left[1 - \frac{1}{2}\exp\left[\frac{E-\mu}{\lambda}\right]\right]^{n-1}$$

$$\frac{dg_n}{dE} = n\frac{1}{2\lambda}\left\{\begin{array}{l}\left[1 - \frac{1}{2}\exp\left[\frac{E-\mu}{\lambda}\right]\right]^{n-1}\frac{d}{dE}\exp\left[\frac{E-\mu}{\lambda}\right] \\ +\exp\left[\frac{E-\mu}{\lambda}\right]\frac{d}{dE}\left[1 - \frac{1}{2}\exp\left[\frac{E-\mu}{\lambda}\right]\right]^{n-1}\end{array}\right\}$$

$$\frac{dg_n}{dE} = n\frac{1}{2\lambda}\left\{\begin{array}{l}\left[1-\frac{1}{2}\exp\left[\frac{E-\mu}{\lambda}\right]\right]^{n-1}\frac{1}{\lambda}\exp\left[\frac{E-\mu}{\lambda}\right] \\ +\exp\left[\frac{E-\mu}{\lambda}\right](n-1)\left[1-\frac{1}{2}\exp\left[\frac{E-\mu}{\lambda}\right]\right]^{n-2}\frac{d}{dE}\left[1-\frac{1}{2}\exp\left[\frac{E-\mu}{\lambda}\right]\right]\end{array}\right\}$$

$$\frac{dg_n}{dE} = n\frac{1}{2\lambda}\left\{\begin{array}{l}\left[1-\frac{1}{2}\exp\left[\frac{E-\mu}{\lambda}\right]\right]^{n-1}\frac{1}{\lambda}\exp\left[\frac{E-\mu}{\lambda}\right] \\ +\exp\left[\frac{E-\mu}{\lambda}\right](n-1)\left[1-\frac{1}{2}\exp\left[\frac{E-\mu}{\lambda}\right]\right]^{n-2}\left[-\frac{1}{2\lambda}\exp\left[\frac{E-\mu}{\lambda}\right]\right]\end{array}\right\} \quad \text{(C.7)}$$

Substitute Equation (C.7) into Equation (C.6):

$$0 = n\frac{1}{2\lambda}\left\{\begin{array}{l}\left[1-\frac{1}{2}\exp\left[\frac{E_n^*-\mu}{\lambda}\right]\right]^{n-1}\frac{1}{\lambda}\exp\left[\frac{E_n^*-\mu}{\lambda}\right] \\ +\exp\left[\frac{E_n^*-\mu}{\lambda}\right](n-1)\left[1-\frac{1}{2}\exp\left[\frac{E_n^*-\mu}{\lambda}\right]\right]^{n-1}\left[-\frac{1}{2\lambda}\exp\left[\frac{E_n^*-\mu}{\lambda}\right]\right]\end{array}\right\}$$

$$E_n^* = \lambda\left[\ln\left(\frac{2\exp\left(\frac{\mu}{\lambda}\right)}{n}\right)\right]$$

$$E_n^* = \mu + \lambda\ln(2) - \lambda\ln(n)$$

$$E_n^* = \mu - \lambda\ln\left(\frac{n}{2}\right) \quad \text{(C.8)}$$

Equation (C.8) defines the dependence of the most probable breakdown field on the sample size n drawn from a Laplace Distribution.

APPENDIX D

PARAMETRIC BOOTSTRAP TECHNIQUE

The parametric bootstrap technique was used to generate the 90% Laplace cumulative distribution confidence bands. An array of 10,000 evenly spaced values, between the upper and lower bounds, was generated for all three parameters (λ, μ, and ρ_V or ρ_A). 1,000 values from each parameter array were chosen at random. Values could be chosen more than once. The range of E^b_{max} values were chosen so that calculated values of $G(E^b_{max})$ would have lower and upper bounds of 0 and 1, respectively. The range of E^b_{max} values were split 0.25 kV/mm increments. For each value of E^b_{max}, $G(E^b_{max})$ was calculated for the 1000 parametric value combinations. The 1000 $G(E^b_{max})$ values were then sorted from smallest to larger. For each value of E, the 100^{th} and 900^{th} values were selected as the 90% confidence bounds. Once the confidence bounds for all values of E^b_{max} were determine the data sets were fit with the $G(E^b_{max})$ function using unconstrained parameters. These functions were used as the confidence bands in Figure 4.15 Additionally, the values of E that returned $G(E^b_{max}) = 0.5$ for each data set were used to 90% confidence bands for Figures 4.7 and 4.9. Tables D.1 and D.2 contains the best fit parameters and 90% confidence bounds for all weakest-link analysis parameters. Below is the MATLAB code used to generate the confidence bands for the Laplace cumulative distribution plots.

Table D.1 Parametric values and 90% confidence bounds derived from weakest-link failure best fits.

Analysis Type	Shape/Location Parameter (90% confidence bounds)	Scale Parameter (90% confidence bounds)
Weibull (Volume Defects)	m = 7.2 (6.035 – 8.4727)	E_0 = 102.6 (kV/mm) (87.21 – 117.99)
Weibull (Surface Defects)	m = 5.5 (4.539 – 6.393)	E_0 = 105.1 (kV/mm) (89.325 – 123.647)
Laplace (Volume Defects)	μ = 54.1 (kV/mm) (51.93 – 56.27)	λ = 2.1 (kV/mm) (1.848 – 2.423)
Laplace (Surface Defects)	μ = 44.8 (kV/mm) (41.981 – 47.197)	λ = 3.2 (kV/mm) (2.721 – 3.735)

Table D.2 Parametric values and 90% confidence bounds derived from weakest-link failure best fits.

Analysis Type	Concentration of Defects (90% confidence bounds)
Weibull (Volume Defects)	$\rho_V = 1.8*10^5$ (defects/mm^3) ($1.6*10^5 – 2.0*10^5$)
Weibull (Surface Defects)	ρ_A = 1718 (defects/mm^2) (1419 – 2022)
Laplace (Volume Defects)	$\rho_V = 1.3*10^8$ (defects/mm^3) ($1.2*10^8 – 1.4*10^8$)
Laplace (Surface Defects)	ρ_A = 1998 (defects/mm^2) (1717 – 2181)

```
clear;
clc;
Function [G_bounds,G,Ea,A,B] =
BootStrap(eff,E_lower,E_upper,lamda_lower,lamda_upper,mu_lower,mu_upper,roh_low
er,roh_upper)

% eff is the effective stressed region, E_lower and E_upper contains the range of E
values for which G(E) should be calculated, lambda_lower and lamda_upper are the 90%
confidence bounds for lamda, mu_lower and mu_upper are the 90% confidence bounds
for mu, roh_lower and roh_upper are the 90% confidence bounds for roh.

n=10000;
m=1000;

% generates an array of n values between and including lambda_upper and lamda_lower
lamda_n=lamda_lower:(lamda_upper-lamda_lower)/(n-1):lamda_upper;
% generates an array of n values between and including mu_upper and mu_lower
```

```
mu_n=mu_lower:(mu_upper-mu_lower)/(n-1):mu_upper;
% generates an array of n values between and including roh_upper and roh_lower
roh_n=roh_lower:(roh_upper-roh_lower)/(n-1):roh_upper;

% generates an array containing values with a spacing of 0.25 between and including
E_upper and E_lower
E=[E_lower:0.25:E_upper];
A=[]; B=[]; G=[];
Ea=E';
for i=1:size(E,2)
%     generates m integers between 1 and n;
   lamda_rand=randi(n,[1,m]);
   mu_rand=randi(n,[1,m]);
   roh_rand=randi(n,[1,m]);
%     stores above for each step in the for loop
   B_temp=[lamda_rand;mu_rand;roh_rand]';
   B=[B,zeros(m,1),B_temp];
%     generates m combinations of lamda, mu, and roh
   lamda_val=lamda_n(lamda_rand);
   mu_val=mu_n(mu_rand);
   roh_val=roh_n(roh_rand);

%     combines above into a m*3 matrix
   A_temp=[lamda_val;mu_val;roh_val]';
%     for each combination of lamda, mu, and roh calculates G(E)
   for j=1:m
      G_temp(j)=1-exp(-(eff*A_temp(j,3)/2)*exp(-(abs(A_temp(j,2)-E(i)))/A_temp(j,1)));
   end
   G=[G;G_temp];
   A=[A,zeros(m,1),A_temp];
end
% for each value of E sorts G(E) values from smallest to largest
G_sort=sort(G,2);
% Takes the 10% and 90% value of G(E)
G_bounds=[G_sort(:,100),G_sort(:,900)];
```

APPENDIX E

E: COMSOL® THERMAL HEATING MODEL

The finite element analysis program Comsol 4.2a was used to construct a thermal heating model. Dielectric heating and joule heating analyzed first independently and then in concert to determine if the heat generation rate was sufficient to raise the specimen temperature. The dielectric heating rate and joule heating rate were given in Equations (1.5) and (1.6), respectively. This study used stainless steel ball electrodes (R_1 = 12.7 mm, R_2 = 12.7 mm) in Diala® oil. The mesh and the oil layer thickness used in this model were identical to those discussed in Section 2.4. The material properties used are listed in Table E.1.

Table E.1 List of material properties for alumina, transformer oil, and steel at 20°C

Material Property	Alumina	Transformer Oil	Stainless Steel
Electrical conductivity, σ [S/m]	$1/(1* 10^{16})$	$1/(200 * 10^{14})$	$4.032 * 10^{6}$
Heat capacity at constant pressure, C_p [J/(kgK)]	900	2020	475
Density, ρ [kg/m^3]	3900	885	7859
Thermal conductivity, k [W/(m*K)]	27	0.124	44.5
Relative permittivity at 60 Hz, ε_r	9.3	2.3	1
Dielectric loss factor, tan δ	10^{-3}	10^{-1}	10^{-1}

Two COMSOL® physics modules, the electrostatics module and the heat transfer module, were used in this analysis. The electrostatics module was used to determine the electric field distribution within the model. The heat transfer module was used to determine the heat generation rate, the heat dissipation, and temperature increase at every node within the model. Within the electrostatics module, the three external faces of the oil were electrically insulated. The voltage ground was applied to the surface of the bottom electrode. The electrical potential was applied to the surface of the top electrode. The applied voltage, V, was determined by the following formula:

$$V = V\_ramp \sin(\omega t) \tag{E.1}$$

In Equation (E.1), V_ramp is a function which ramps voltage at a rate of 2 kV/sec starting from 0 kV at $t = 0$ sec, t is the time, and ω is the angular frequency. The electrostatics module solved the Poisson's Equation to calculate the electric field. In the heat transfer module, it was assumed that the dielectric oil had a flow velocity, u, of 0 m/s. Therefore, the heat transfer in both the solid and liquid phases was considered to be conductive heat transfer. Pure conductive Heat transfer is governed by the following equation:

$$\rho C_p \frac{\partial T}{\partial t} - \nabla(k \nabla T) = Q \tag{E.1}$$

In Equation (E.2), ρ is the density, C_p is the specific heat capacity at constant pressure, T is the temperature, and k is the thermal conductivity. Both joule heating and dielectric heating were considered as sources of the heat generation rate. The initial temperature as

well as the external temperature were set to 20°C. The temperature change across the phase boundaries was set to zero.

Resultant values were recorded every 0.1 seconds starting from 0 sec and continuing until breakdown voltage was reached. For a commercial grade specimen (R = 38.1 mm, t = 4 mm) with ball electrodes (R_1 = 12.7 mm and R_2 = 12.7 mm) in Diala® oil the breakdown voltage is 41.50 kV. Figure E.1 shows the electric fields, E, in the test system at the breakdown voltage. At the breakdown voltage the maximum electric fields were 60.22 kV/mm and 14.89 kV/mm in the Diala® oil and commercial-grade alumina specimen, respectively. Figure E.2 shows the heat generation rates, Q, in the test system at the breakdown voltage. The maximum heat generation rates at the breakdown voltage were 2783.2 W/m^3 and 688.1 W/m^3 in the Diala® oil and the commercial-grade alumina specimen, respectively. Figure E.3 shows the temperatures, T, in the test system at the breakdown voltage. The maximum temperatures at breakdown were 20.000167°C and 20.00009692°C in the Diala® oil and in the commercial grade alumina specimen, respectively. The power generated due to dielectric heating is significantly great than that due to joule heating. However, the total power generation rate was insufficient to generate a significant temperature increase. The observed temperature change was insignificant to be the cause of the breakdown. The temperature increased by less than one degree. The variation of material properties with temperature did not play a role in the analysis. This is due to the fact that the total change in temperature was less than 0.001°K in both the Diala® oil and the commercial-grade alumina specimen.

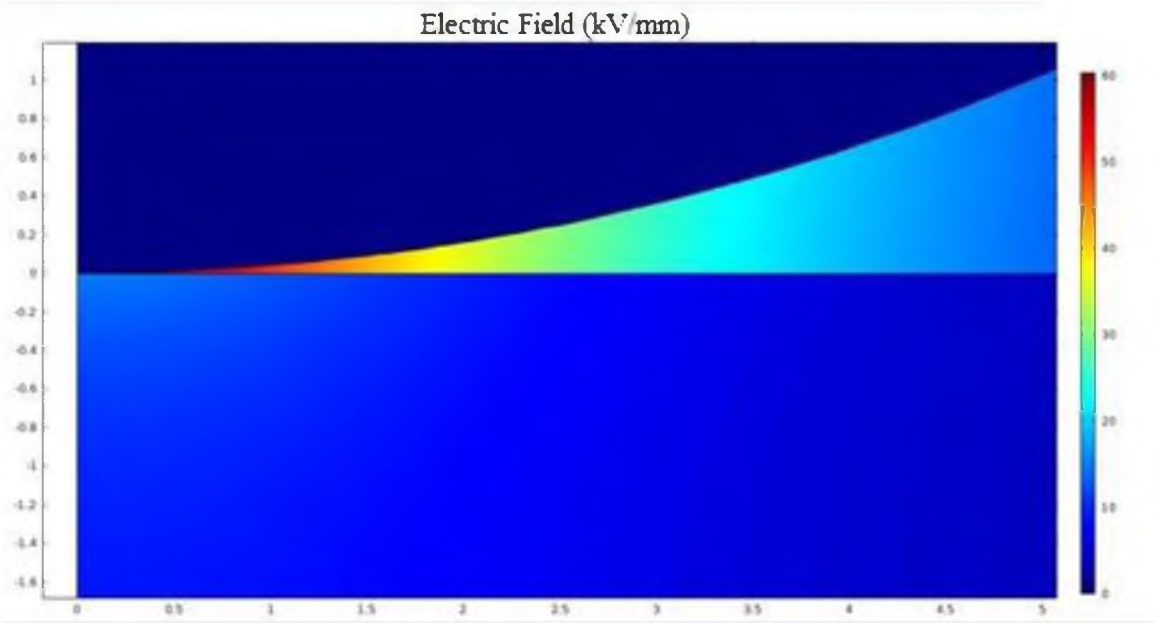

Figure E.1 Electric fields in the test system at the breakdown voltage.

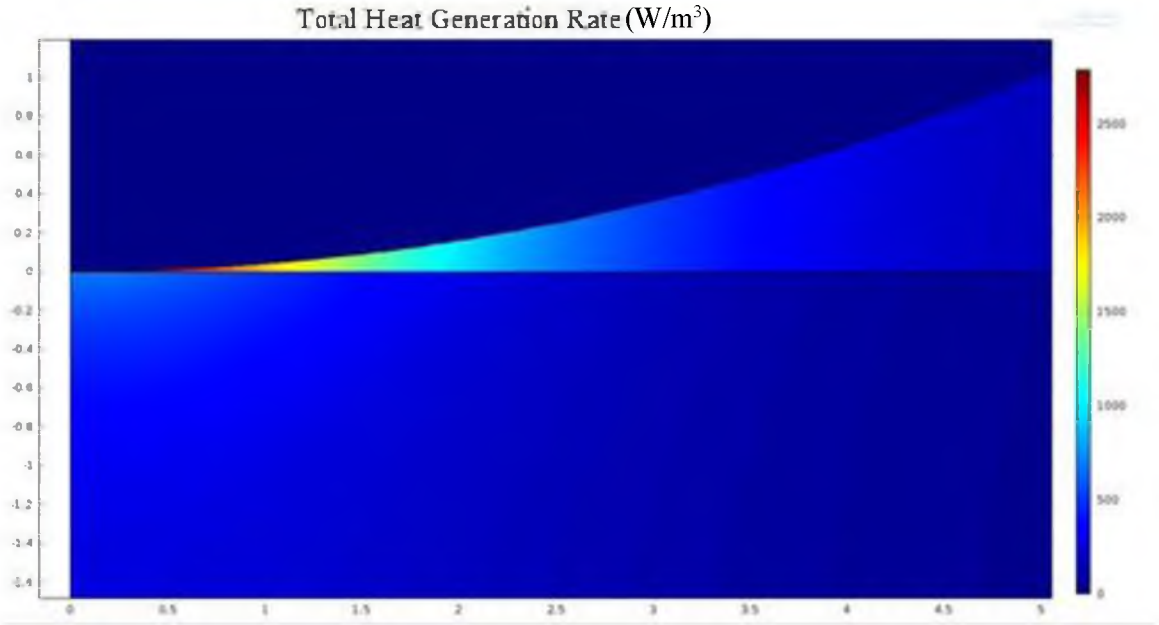

Figure E.3 Heat generation rates in the test system at the breakdown voltage.

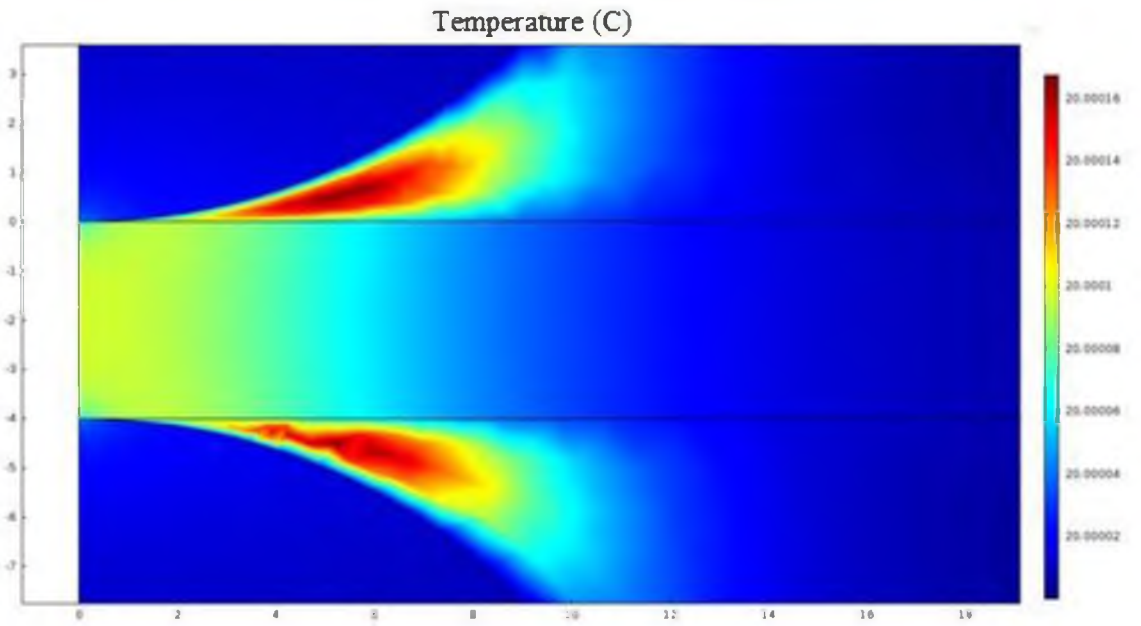

Figure E.3 Temperatures in the test system at the breakdown voltage.

REFERENCES

1. M. Touzin, D. Goeuriot, C. Guerret-Piecourt, D. Juve and H. J. Fitting, "Alumina Based Ceramics for High-Voltage Insulation," *J. Eur. Ceram. Soc.*, vol. 30, pp. 805-817, 2010.

2. C. T. Morse and G. J. Hill, "The Electric Strength of Alumina: The Effect of Porosity," *Proc. Brit. Ceram. Soc.*, vol. 18, pp. 23-35, 1970.

3. W. H. Gitzen, "Electrical Properties of Alumina," in *Alumina As A Ceramic Material*, Columbus, The American Ceramic Society, Inc., 1970, pp. 79.

4. M. Yoshimura and H. K. Bowen, "Electrical Breakdown Strength of Alumina at High Temperatures," *J. Am. Ceram. Soc.*, vol. 64, pp. 404-410, 1981.

5. I. O. Owate and R. Freer, "The Dielectric Breakdown of Alpha Alumina Ceramic At Room Temperature," *Sci. Ceram.*, vol. 18, pp. 1013-1018, 1988.

6. P. D. Lomer, "The Dielectric Strength of Aluminum Oxide Films," *Proc. Phys. Soc. London Section B*, vol. 63, pp. 818-820, 1950.

7. W. S. Nicol, "Thickness Variation of Breakdown Field Strength in Plasma Oxidized Aluminum Films," *Proc. IEEE*, vol. 56, pp. 109-110, 1968.

8. Y. Kim, "Effects of Electrode Geometry and Dielectric Media on Dielectric Breakdown Strength of Polycrystalline Alumina," M.S. thesis, Dept. of MSE, Univ. of Utah, UT, 2010.

9. H. Frohlich, "Theory of Electrical Breakdown in Ionic Crystals," *Proc. Roy. Soc. In London*, vol. A 160, pp 230-241, 1937.

10. F. Seitz, "On the Theory of Electron Multiplication in Crystals," *Phys. Rev.*, vol 76, no. 9, pp. 1375, 1949.

11. J. J. O'Dwyer. "Theory of High Field Conduction in a Dielectric," *J. Appl. Phys.*, vol. 40, no. 10, pp. 3887-3890, 1969.

12. J. J. O'Dwyer, "Breakdown in Solid Dielectrics," *IEEE Trans. Elec. Insul. EI-17*, vol. 6, pp. 484-487, 1982.

13. V. Fock, "To the Heat Theory of Electric Breakdown," *Arch. Elektrontech*, vol. 19, pp. 71-81, 1927.

14. P.H. Moon, "The Theory of Thermal Breakdown of Solid Dielectrics," *Trans Am. Inst. Eleck. Engrs.*, vol. 50, no. 3, pp. 1008-1021, 1931.

15. Kwan Chi Kao, Dielectric Phenomena in Solids: With Emphasis on Physical Concepts of Electronic Processes, San Diego, Elsevier Academic Press, 2004.

16. J. H. Lienhard IV, J. H. Lienhard V, A Heat Transfer Text Book, 4th Ed., Cambridge, Phlogiston Press, 2012.

17. X.D. Yu, V.V. Varadan, V.K. Varadan "Modeling Microwave Heating of Ceramics" in Ceramic Transactions. V. 21 Proceedings of the Symposium on Microwave Theory and Application in Materials Processing Annual Meeting of American Ceramic Society 23rd, 1991.

18. M. Yoshiruma and H.K. Bowen, "Electrical Breakdown Strength of Alumina at High Temperatures". *Journal of the American Ceramic Society*, vol. 64, pp. 404–410, 1981.

19. J. W. Cable, Induction and Dielectric Heating, New York, Reinhold Publishing, 1964.

20. B. Epstine, "Statistical Aspects of Fracture Problems," *J. App. Phys.*, vol. 18, pp. 140 – 147, 1948.

21. J. K. Nelson, "Breakdown Strength of Solids." in Engineering Dielectrics, Vol. 2A, Electrical Properties of Solid Insulating Materials; Molecular Structure and Electrical Behavoir, Edited by R. Bartnikas and R. M. Eichhorn. ASTM STP 783, American Society for Testing and Materials, Philadelphia, pp. 445-520, 1983.

22. W. Weibull, "A Statistical Theory of the Strength of Materials," Ingeniörsvetenskapsakademiens Handlingar Nr 151, Stockholm, Sweden Generalstabens Litografiska Anstalts Förlag, 1939.

23. B. Epstein, "Application of the Theory of Extreme Values in Fracture Problems," *J. Am. Stat. Assoc.*, vol. 43, no. 243, pp. 403-412, 1948.

24. Yoshinobu Nakamura, Mikito Suzuki, Naobumi Motohira, Akira Kishimoto, and Hiroaki Yanagida, "Comparison between the Mechanical and Dielectric Strength Distributions for Hardened Gypsum," *J. Mat. Sci.*, vol. 32, pp. 115-118, 1997.

25. F.T. Pierce, "Tensile tests for cotton yarns v. 'The weakest link' – theorems on the strength of long and composite specimens," *J. Tex. Inst.*, vol. 17, pp. 355 (1926).

26. L.H.C. Tippett, "On the extreme individuals and the range of samples taken from a normal population," *Biometrika*, vol. 17, pp. 364 (1925).

27. R. Gerson and T. C. Marshall, "Dielectric Breakdown of Porous Ceramics," *J. Applied Physics*, vol. 30, no. 11, pp. 1650 – 1653, 1959.

28. P. M. Duxbury, P. D. Beale, and P. L. Leath "Size Effects of Electrical Breakdown in Quenched Random Media," *Physical Review Letters*, vol. 57, no. 8, pp. 1052 – 1055, 1982.

29. S. Beaudet, J. C. Bernier and D. Autissier, "Doping Elements Influence on Microstructural and Dielectric Properties of Alpha Alumina," *Key Engineering Materials*, vol. 132, pp. 1179-82, 1997.

30. J. Leibault, J. Bigarre, D. Treheux, D. Goeuriot, and F. Thevenot, "Influence of Microstructural Parameters on Dielectric Properties of Polycrystalline Alumina," in CSC'3 Proceedings, vol. 53, 391 – 400, 1998.

31. J. Liebault, J. Vallayer, D. Goeuriot, D. Treheux and F. Thevenot, "How the Trapping of Charges Can Explain the Dielectric Breakdown Performance of Alumina Ceramics," *J. Eur. Cera. Soc.*, vol. 21, pp. 389 – 397, 2001.

32. S. R. Sangawar and H. H. Kumar, "Alumina-based Ceramic Material for High-voltage Ceramic Substrate," *Defence Science Journal*, vol. 56, pp. 269 – 278, 2006.

33. M. Touzin, D. Goeuriot, H.-J. Fitting, C. Guerret-Piecout, D. Juve, D. Treheux, "Relationship between dielectric breakdown resistance and charge transport in alumina materials- Effects of the microstructure," *J. Euro. Ceramic S.*, vol. 27, pp. 1193 – 1197, 2007.

34. I. O. Owate and R. Freer. "Dielectric Breakdown of Ceramics and Glass Ceramics," in Proceedings of the 6th International Conference on Dielectric Materials, Measurements and Applications, pp. 443 – 446, 1992.

35. F. Talbi and F. Lalam, "Dielectric Breakdown Characteristics of Alumina," in International Conference on Solid Dielectrics, Potsdam, Germany, 2010.

36. I. O. Owate and R. Freer, "AC Breakdown Characteristics of Ceramic Materials," *J. Appl. Phys.*, vol. 72, pp. 2418 – 2422, 1992.

37. T. Shioiri, T. Shindo, T. Kamikawaji, E. Kaneko, and I. Ohshima. "Effect of Annealing and Polishing on Flashover Characteristics of Ceramic in Vacuum," *IEE Trans.*, vol. 9, no. 3, pp. 416 – 420, 2002.

38. Hisao Miyazawa and Jun-ichi Okada, "On the Breakdown of Alumina at Higher Temperature," *J. Phys. Soc. Jpn.*, vol. 6, pp. 55 – 59, 1950.

39. H. Goshima, N. Hayakawa, M. Hikita, H. Okubo, and K. Uchida, "Area and Volume Effects on Breakdown Strength in Liquid Nitrogen," *IEEE Trans.*, vol. 2, no. 3, pp. 376-384, 1995.

40. H. Goshima, N. Hayakawa, M. Hikita, H. Okubo, and K. Uchida, "Weibull Statistical Analysis of Area and Volume Effects on the Breakdown Strength in Liquid Nitrogen," *IEEE Trans.*, vol. 2 no. 3, pp. 385-393, 1995.

41. N. Hayakawa, H. Sakakibara, H. Soshima, M. Hikita, and H. Okubo, "Breakdown Mechnism of Liquid Nitrogen Viewed from Area and Volume Effects," *IEEE*, vol. 4 no. 1, pp. 127-134, 1997.

42. D. Tibbitts, "Dielectric Breakdown of Alumina: A Weakest-Lin Failure Analysis," M.S. thesis, Dept. of MSE, Univ. of Utah, UT, 2006.

43. Tzu-Chien Wen and Dinesh K. Shetty "Colloidal Processing and Optical Transmittance of Submicron Polycrystalline Alumina" *Proc. SPIE* 8016, Window and Dome Technologies and Materials XII, 80160C, 2011.

44. CoorsTek AD-94 Alumina Material Properties Sheet. Available: http://www.coorstek.com/materials/ceramics/alumina_ad-94.php

45. "Standard Test Method for Dielectric Breakdown Voltage and Dielectric Strength of Solid Electrical Insulating Materials at Commercial Power Frequencies," ASTM Standard D 149-97a, American Society for Testing and Materials, Philadelphia, PA, 1997.

46. H. Li, G. Liu, B. Liu, W. Chen, S Chen, "Dielectric properties of polyimide/Al2O3 hybrids synthesized in-situ polymerization", *Materials Letter*, vol. 61, no. 7, pp. 1507-1511, 2007.

47. D. F. Binns and T. J. Randall, "Calculation of Potential Gradients for a Dielectric Slab Placed between a Sphere and a Plane," *Proc. IEE*, vol. 114, pp. 1521 – 1528, 1967.

48. T. Takuma and T. Kawamoto, "Field Intensification Near Various Points of Contact with a Zero Contact Angle between a Solid Dielectric and an Electrode," *IEEE Trans.* vol. 103, pp. 2486 – 2494, 1984.

49. E. Poli, "The Use of Image Charges in the Charge-Simulation Method: A Parallel-Plane Dielectric Plane Covering a Conductor," *IEEE Trans. on Magnetics*, vol. 28, no. 2, pp. 1076-1079, 1992.

50. H. Singer, H. Steinbigler, and P. Weiss, "A Charge Simulation Method of the Calculation of High Voltage Fields," *IEEE Trans.*, vol. 93, pp. 1660 – 1667, 1974.

51. B. Epstein and H. Brooks, "The Theory of Extreme Values and Its Implications in the Study of the Dielectric Strength of Paper Capacitors," *J. Appl. Phys.*, vol. 19, pp. 544 – 550, 1948.

52. D. Milton and J. L. Wentz, "The Impulse Strength of Certain Casting Resins is Area Dependent," *Insulation*, pp. 71 – 76, May, 1966.

53. R. Lovell, "The Effect of Specimen Size on the Electric Breakdown of Unfilled and Filled Epoxy Polymers," *IEEE Trans. On Electrical Insulation,* vol. EI-11, no.4, pp. 110 – 114, 1976.

54. K. Kristiansen, "A Statistical Approach to the Analysis of Dielectric Breakdown Strength of Thin Insulating Films," *Vacuum*, vol. 27, no. 4, pp. 227 – 233, 1977.

55. K. H. Weber and H. S. Endicott, "Area Effect and Its Extreme Basis for the Electric Breakdown of Transformer Oil," *IEE Trans. On Power Apparatus and Systems*, vol. 75, pp. 371 – 381, 1956.

56. L. Y. Chao and D. K. Shetty, "Extreme-Value Statistics Analysis of Fracture Strength of a Sintered Silicon Nitride Failing from Pores," *J. Am. Ceram. Soc.*, vol. 75, no. 8, pp. 2116 – 2124, 1992.

57. B. Carnahan, H. A. Luther and J. O. Wilkes, "Numerical Integration," *Applied Numerical Methods*, New York, John Wiley and Sons, Inc., 1969, pp. 69.

58. C.A. Johnson and W.T. Tucker, "Advance Statistical Concepts of Fracture in Brittle Materials," in *Engineered Material Handbook*, Vol. 4 Ceramics and Glass, Metals Park, ASM International 1994, pp. 709-715.

59. R.T. DeHof and F.N. Rhines, "Particle Size Distribution," in Quantitative Microscopy, Columbus, McGraw-Hill, Columbus, 1968, pp. 152.

60. H.R. Zeller "Breakdown and prebreakdown phenomena in solid dielectrics" *IEEE Transactions on Electrical insulation*, vol. EI-22, no. 2, pp. 115-122, 1987.

61. W.V. Houston "Acceleration of Electrons in a Crystal Lattice" *Physical Review*, vol. 57, pp. 184-186, 1940.

62. M. Sparks "Theory of Electron Avalanche Breakdown in Solids" *Phys. Rev. B*, vol. 24, no. 6, pp. 3519 – 3536, 1981.

63. A. von Hippel, "Ergebnisse der Exakten Naturwissenschaften" vol. 14, pp. 79, 1935.

64. B.S. Rawal and N.H. Chan "Conduction and failure of mechanisms in barium titanate based ceramics under highly accelerated conditions" AVX corporation product report, Myrtle Beach, SC 1984.

65. Y.H. Chen, W.H. Tuan, J. Shieh "Effect of microstructure on lifetime performance of barium titanate ceramics under DC electric field loading" *J. European Ceramic Society*, vol. 30, pp. 2577-2583, 2010.